

Department of Physics and Astronomy

Heidelberg University

Master thesis

in Physics

submitted by

Lucas Dittmann

born in Würzburg

2022

Tests of an HV-CMOS Prototype for the LHCb MightyTracker

This Master thesis has been carried out by Lucas Dittmann

at the

Physikalisches Institut

under the supervision of

Prof. Dr. Ulrich Uwer

Zusammenfassung:

Der Detektor des LHCb-Experiments am CERN soll während der vierten Wartungspause des LHC 2033 ein zweites Mal aufgerüstet werden, da der Luminositätsanstieg an dem Kollisionspunkt des LHCb-Experiments zu hoch für den aktuellen Detektor ist. Während diesem Upgrade soll der zurzeit betriebene Szintillationsfaserdetektor durch den MightyTracker ersetzt werden. Dieser Subdetektor besteht aus zwei unterschiedlichen Detektortechnologien. Der innere Teil des Detektors besteht aus HV-MAPS Pixelsensoren, die MightyPix Sensoren. Der äußere Teil des MightyTrackers besteht aus szintillierenden Fasern. Ein Vorgänger des MightyPix Sensors, der ATLASPix3.1 Sensor, und eines seiner Auslesesysteme, das GECCO-System, werden zur Entwicklung von Messaufbauten für MightyPix-Prototypen verwendet. Der ATLASPix3.1 Sensor wird mit elektronischen Pulsen und radioaktiven Quellen getestet, um die Schwellenwerte des Sensors zu optimieren. Die theoretische Begrenzung der Trefferraten des ATLASPix3.1 Sensors wird berechnet und mit der experimentell bestimmten maximalen Trefferrate verglichen. Für die Ratenmessung wird ein Photonenstrahl aus einer Röntgenröhre verwendet. Die maximale Ausleserate des ATLASPix3.1 beträgt 9,7 MHz, was mit der berechneten theoretischen Grenze kompatibel ist. Außerdem wird das Verhalten dieses Sensors in Ionenstrahlen mit experimentellen Messungen und Simulationen untersucht. Es wird festgestellt, dass die Größe der Hit-Cluster und das ToT des Clusters mit der Energiedeposition zunehmen und dass Kernwechselwirkungen zwischen den Ionen des Strahls und dem Sensormaterial zu sehr großen Hit-Clustern führen.

Abstract:

The detector of the LHCb experiment at CERN will be upgraded a second time during the long shutdown 4 of the LHC, starting in 2033, to cope with the further luminosity increase at LHCb's interaction point. In this upgrade, the scintillating fiber tracker installed in Upgrade I is planned to be replaced by the MightyTracker. This subdetector consists of an inner part made from HV-MAPS pixel sensors called MightyPix and an outer part made from scintillating fibers. A predecessor of the MightyPix, the ATLASPix3.1, and one of its readout systems, the GECCO system, are used to develop measurement setups for MightyPix prototypes. The ATLASPix3.1 is successfully tuned by using injection pulses and radioactive sources.

The theoretical rate limit of the ATLASPix3.1 is calculated and compared to an experimentally determined maximum rate. A photon beam from an X-ray tube is used for the high rate measurement. The operational maximum readout rate of the ATLASPix3.1 is 9.7 MHz, which is compatible with the calculated theoretical limit. Furthermore, the behavior of the sensor in ion beams is studied with experimental data and simulations. It is found that the size of the clusters hit as well as the ToT of the cluster increase with energy deposition. Nuclear interaction between ions and sensor material can lead to the formation of large hit clusters.

Contents

1	Introduction	6
2	Standard Model of Particle Physics	8
2.1	The Weak Interaction and CP - Violation	8
3	The LHCb Experiment	11
3.1	The Upgrade I LHCb Detector	11
3.1.1	Tracking system	12
3.1.2	Particle Identification	15
3.2	LHCb Upgrade II Plans	17
3.2.1	Detector Layout	17
3.2.2	MightyTracker	18
4	Particle Detection	20
4.1	Charged Particle Interaction in Matter	20
4.1.1	Ionization	20
4.1.2	Bremsstrahlung	22
4.2	Interaction of Photons with Matter	23
4.3	Semiconductor Sensors	23
4.3.1	Working Principle	23
4.3.2	Silicon Pixel Detectors	25
4.3.3	HV-CMOS High-Voltage Monolithic Active Pixel Sensors . . .	25
5	HV-CMOS Sensor ATLASPix3.1	28
5.1	Pixel Matrix	30
5.2	Readout	33
5.2.1	Untriggered Readout	33
5.2.2	Triggered Readout	33
5.3	Clock Distribution	34
5.4	MightyPix v1	35
6	Measurement Setup	36
6.1	GECCO Readout System	36
6.1.1	Hardware	36
6.1.2	Firmware	37
6.1.3	Control Software	38
6.2	Signal & Particle Sources	39
6.2.1	Injection Pulses	39

6.2.2	Radioactive Particle Sources	39
6.2.3	X-Ray Tube	40
6.2.4	Heidelberg Ion Therapy Center	41
6.3	Sensor Configuration	41
7	Calibration Measurements	43
7.1	Global Sensor Calibrations	43
7.2	Injection Pulses: Local Threshold Calibrations	47
7.2.1	S-Curves	48
7.2.2	Threshold Trimming	50
7.3	Radioactive Particle Source: Energy Response	53
7.3.1	Strontium-90	53
7.3.2	Iron-55	55
7.3.3	Crosstalk Hits	56
8	High Rate Measurements	58
8.1	Readout Delay	60
8.2	Rate Limitations	64
8.2.1	Theoretical Limitations of the Setup	64
8.2.2	Experimental Limitation	66
8.2.3	Summary	73
9	Ion Beam Measurements	75
9.1	Spill Structure	77
9.2	Energy Spectra & Clustering	78
9.2.1	Cluster Analysis of the Carbon Ion Measurements	83
9.2.2	Bumps	85
9.2.3	Sensor Response	87
9.3	Simulation	88
9.3.1	GEANT4 Simulation	88
9.3.2	Allpix ² Simulation	94
9.3.3	Summary	97
10	Conclusion	98
A	Sensor Configuration	100
B	Hitmap Pattern	102
B.1	State Machine Error	102
B.2	Oscillation	103
C	Bibliography	104

1 Introduction

The interaction of fundamental particles is described by a quantum field theory, the standard model of particle physics (SM). Since its development in the 1960 and 1970s, this theory has been tested and measured precisely by several experiments. The most recent success of the standard model is the prediction [1] and the discovery of the Higgs boson by the experiments ATLAS and CMS in 2012 [2][3].

Although the standard model is a well-established theory, it fails to explain observations and facts like the asymmetry of matter and antimatter in the universe [4], the mass of neutrinos [5] or the existence of dark matter [6]. In order to explain these observations, new theoretical models predicting new physics phenomena and particles are necessary. To date, no new physics phenomena beyond the description of the standard model have been observed. The quest for new physics is one of the driving motivations for research at the large hadron collider (LHC). New physics phenomena could manifest either directly, as new particles, or indirectly through new quantum loops influencing the decay of very rare B- and D-mesons for example.

LHCb is a dedicated experiment to search for new phenomena in the decay of heavy mesons. The LHCb experiment has been upgraded recently and has started a new data taking run. Until 2033, the current data sample of LHCb will have been increased at least by a factor 6. Afterwards, the LHCb collaboration plans to upgrade the detector a second time for it to run at an even higher luminosity to increase the data sample even further. In this upgrade, many changes to the detector layout and subdetectors are planned. One of them being the replacement of the scintillating fiber (SciFi) tracker by the MightyTracker. The MightyTracker is planned to consist of two detector technologies. In the inner region of the MightyTracker, particles are detected by silicon pixels sensors, the so-called MightyPix, while the outer region of the detector consists of scintillating fibers. The sensors chosen for the silicon part of the detector are High-Voltage Monolithic Active Pixel Sensors (HV-MAPS) [7] produced in HV-CMOS technology. These sensors consist of a pixel structure, where every pixel includes a charge-detecting diode as well as the front-end electronics to digitize the charge pulse created by the pixel diode. Since the entire readout is already placed in the pixel, this technology has a smaller material budget than hybrid silicon pixel detectors.

This thesis develops and validates measurement setups, which can be used for MightyPix prototypes. For this a full-scale HV-MAPS prototype ATLASPix3.1, a predecessor of the LHCb prototype MightyPix, is used.

This thesis is sketched as follows: The next chapter gives a short introduction into

the underlying theory of particle physics. The third chapter describes the current layout of the LHCb detector and the planned upgrade II. Chapter 4 introduces the principles of particle detection and silicon pixel detectors, while Chapter 5 describes the HV-CMOS sensor ATLASPix3.1 tested in this thesis. Subsequently, the data acquisition system (DAQ) and the measurement setups used to test the pixel sensor are explained in Chapter 6. The following Chapter 7 depicts the initial measurements performed to confirm the proper functioning of the sensor under test and the DAQ system. In Chapter 8, the delay of the sensor readout and the hit rate capabilities of the sensors are determined by using X-ray. Lastly, the sensor under test is operated in an ion beam. The observations in these measurements and simulations performed to understand these observations are shown in Chapter 9. Finally, a summary of the measurements performed in this thesis is given in Chapter 10.

2 Standard Model of Particle Physics

The standard model of particle physics (SM) [9][10][11] describes the current knowledge of the interaction of fundamental particles. The particles of the SM and their masses are shown in Figure 2.1. The theory can be divided into two parts: the electro-weak (EW) theory and quantum chromodynamics (QCD). The theory of quantum chromodynamics describes the strong interaction between quarks. On the other hand, the electro-weak theory describes the weak and the electromagnetic force.

Since the SM is a quantum field theory, each force is mediated by gauge bosons with spin 1 [12]. The weak force is mediated by the massive W^\pm bosons and Z-boson, the electromagnetic force by the massless photon γ and the strong force by eight massless gluons g . Additionally, there is the Higgs boson with spin 0, which generates the mass for the massive bosons and fermions by electroweak symmetry breaking. [1]

In the standard model there are 12 fermions with spin $\frac{1}{2}$. The fermions are divided into six quarks and six leptons. The six quarks are all massive and are divided into two types. The up-, charm- and top-quarks, the so-called up-type quarks, have an electric charge of $+\frac{2}{3}$. On the other hand, the down-, strange- and bottom-quarks are called down-type quarks and have a charge of $-\frac{1}{3}$. The leptons consist of three massive leptons, which are negatively charged (-1), the electron, muon and tauon as well as three massless and neutral electron-, muon- and tauon-neutrino. Further, these fermions can be grouped into three generations. Each generation consists of an up-type quark, a down-type quark, a charged lepton and a neutral lepton, such that these generations only differ by the mass of the particles. The generation and mass structure of the standard model is currently not understood.

Quarks and gluons are the only particles carrying one of the three different color charges of the strong interaction. Due to the asymptotic freedom of the QCD, quarks and gluons can not be free. Instead, quarks form a bound and color neutral state, the so-called hadrons, while gluons decay into hadrons. These hadrons are divided into mesons, which are made of a quark and an anti-quark, and baryons, which consist of three quarks or three anti-quarks.

2.1 The Weak Interaction and CP - Violation

In the electro-weak theory, the flavor of quarks is changed via the charged current interaction by W^\pm -bosons. In contrast, flavor changing processes involving neutral bosons (Z, γ) are forbidden at the first order (tree level) of the standard model. However, at higher order quantum corrections (box and penguin diagrams) flavor

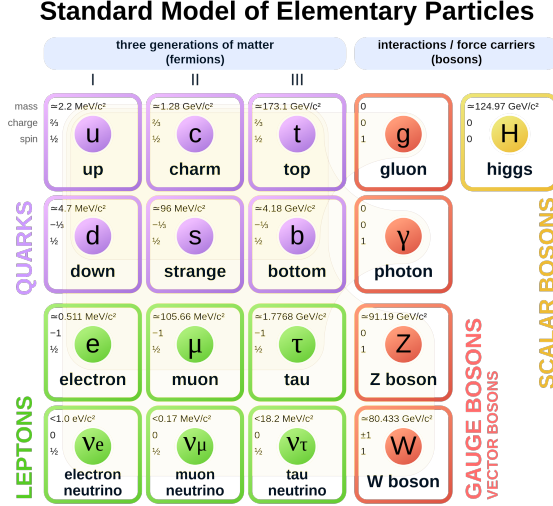


Figure 2.1: The fundamental particles of the standard model.[8]

changing neutral currents are possible but heavily suppressed by the GIM mechanism.

The flavor change of the weak charged current interaction is described by the Cabibbo-Kobayashi-Maskawa (CKM) matrix with the mixing parameter V_{ij} , which mix the flavor (weak) eigenstates (d') and the mass eigenstates (d):

$$\begin{pmatrix} d' \\ s' \\ b' \end{pmatrix} = \begin{pmatrix} V_{ud} & V_{us} & V_{ub} \\ V_{cd} & V_{cs} & V_{cb} \\ V_{td} & V_{ts} & V_{tb} \end{pmatrix} \begin{pmatrix} d \\ s \\ b \end{pmatrix} \quad (2.1)$$

Because of the unitarity, the CKM matrix can be described with three rotation angles and a complex phase. The appearance of this complex phase is responsible for CP-violation in the quark sector of the standard model, where the abbreviation CP stands for charge-parity conjugation. A charge conjugation transforms a particle into its antiparticle ($X \rightarrow \bar{X}$), while a parity transformation inverts the spatial coordinates ($\vec{x} \rightarrow -\vec{x}$). CP-violation can occur in a direct ($\Gamma(X \rightarrow f) \neq \Gamma(\bar{X} \rightarrow \bar{f})$) or an indirect process, which can be a mixing process ($P(X \rightarrow \bar{X}) \neq P(\bar{X} \rightarrow X)$) or the interference between mixed and unmixed states. While by rephasing the CKM matrix all CKM elements can in principle be complex, it is very common to use a parameterization, where at the lowest order only the two elements V_{td} and V_{ub} are complex. The phase of the two complex parameter V_{td} and V_{ub} are generally called β and γ , respectively:

$$V_{\text{CKM}} = \begin{pmatrix} |V_{ud}| & |V_{us}| & |V_{ub}|e^{-i\gamma} \\ |V_{cd}| & |V_{cs}| & |V_{cb}| \\ |V_{td}|e^{-i\beta} & |V_{ts}| & |V_{tb}| \end{pmatrix} \quad (2.2)$$

This parameterization of the CKM matrix allows to make predictions for CP-violating effects in B-mesons: Decays of B-mesons involving a $b \rightarrow u$ transition could exhibit direct CP violation allowing a measurement of the phase γ . On the other hand, decays involving an oscillation between B^0 and \bar{B}^0 states with a box diagram including top quarks could lead to time dependent CP-violation and thus allow the measurement of β . An experiment dedicated to measuring CP-violation in B- and D-mesons is the LHCb experiment at CERN. Moreover, the experiment studies very rare B- and D-meson decays which may provide a hint on possible new phenomena in quantum loops.

3 The LHCb Experiment

The LHCb experiment is located at the circular proton-proton collider LHC (Large Hadron Collider), which lies on the french-swiss border at Geneva and is operated by CERN. The LHC has a circumference of almost 27 km and provides proton-proton collisions with center of mass energy up to $\sqrt{s} = 14$ TeV. The LHCb experiment operates since 2009 and has collected data corresponding to an integrated luminosity of 9 fb^{-1} until the second long shutdown of the LHC (LS2) in 2018. During this shutdown the entire LHCb detector has been upgraded to cope with the 5 times higher instantaneous luminosity at LHCb's interaction point. In the following runs starting in 2022 LHCb is expected to measure data corresponding to an integrated luminosity up to 50 fb^{-1} until its next major upgrade planned for the long shutdown LS4 in 2033.

LHCb uses mesons containing bottom and charm quarks to measure CP-violation and to search for rare decays. In the standard model these decays are possible only through higher order quantum loops, which are highly suppressed. The decays are therefore sensitive to new phenomena appearing as additional quantum corrections. Because bottom quarks are created in pairs ($b\bar{b}$) in either forward or backward directions at LHC's energies, the LHCb detector is built as a single-arm forward spectrometer covering an angle of 300 mrad in the horizontal plane, the bending plane of the experiment's magnet, and an angle of 250 mrad in the vertical plane.

3.1 The Upgrade I LHCb Detector

The LHCb detector consists of many subdetectors, which can be grouped into two categories. One category comprises tracking detectors measuring the track and momentum of the particle traversing the detector. The second detector group is dedicated towards the identification of the particle species. The detector layout of Run 3 (after Upgrade I) is described in the following and shown in Figure 3.1.

In contrast to Run 1 and Run 2, where LHCb used a hardware trigger, after Upgrade I the LHCb detector is now taking data with a software trigger, which increases the data taking rate. To allow an online event building in the software trigger structure, it is necessary that all subdetectors are read out with the LHC bunch crossing frequency of 40 MHz.

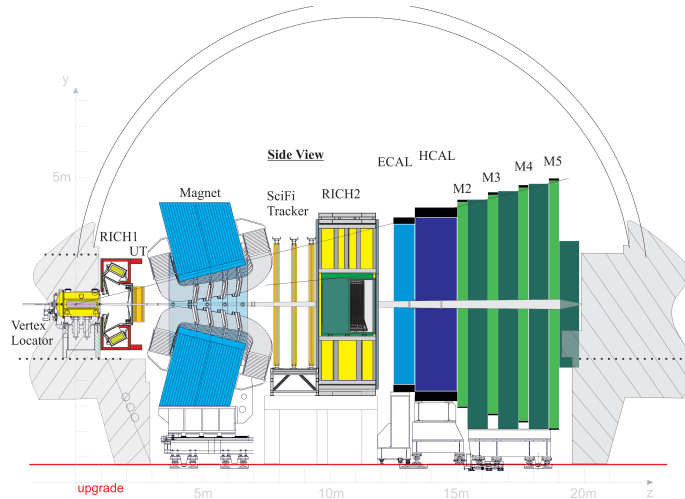


Figure 3.1: The LHCb upgrade I detector of Run 3.[13]

3.1.1 Tracking system

The tracking system consists of three subdetectors, two in front of the dipole magnet and one downstream of the magnet. The dipole magnet is used to bend the track of charged particles in the horizontal plane. Using the Lorentz force, the particle's momentum is determined from the curvature of the bent track. To do so, the deflection angle needs to be measured precisely and thus at least two measurement points of the particle track in front and behind the magnet are needed. LHCb's dipole magnet creates a homogeneous magnetic field with an integrated field strength of 4 Tm. In order to cope with the 5 times higher luminosity in Run 3 of the LHC, the complete LHCb tracking system was upgraded during LS2. [13][14]

Vertex Locator

The Vertex Locator (VELO) is placed around the collision point of the two proton beams to measure the track of b- and c-hadrons created in the collision. These particles fly through the detector for about 1 cm before they decay. The determination of their decay vertex is important in order to be able to distinguish their decay products from particles created in the primary proton-proton collision. Therefore, the VELO layers need to be very close to the interaction point. The VELO is split into two halves on either sides of the beam pipe, such that the VELO can be moved in and out of the interaction point to reduce radiation damage by unstable beams when the detector is not collecting data. Each half side consists of 26 modules on which 4 hybrid pixel sensors with 3 ASICs (Application Specific Integrated Circuit) each, the so-called VELOpix, are placed. The sensors are orientated in an L-like shape such that both detector halves can enclose the beam pipe completely as shown in Figure 3.2. The VELO sensors consists of 256×256 pixel with a pitch of $55 \times 55 \mu\text{m}^2$ allowing a precise spatial measurement. Moreover, this pixel pitch

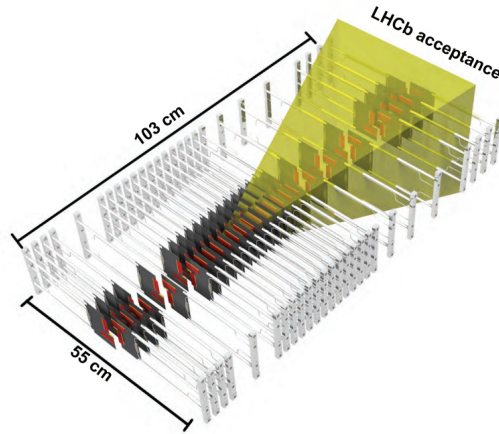


Figure 3.2: Structure of the VELO modules. The sensors and ASICs are shown in red. The acceptance of the other is subdetectors is indicated in yellow.[14]

allows the VELOpix sensors to detect particles at a mean hit rate of 600 MHz in the hottest regions. [14]

Upstream Tracker

The Upstream Tracker (UT) is, as its name suggests, placed upstream of the dipole magnet. The subdetector consists of 4 layers of silicon strip sensors. Each layer covers an active area of 2 m^2 . Due to different occupancy and radiation damage during operation, four sensor types with different strip pitches are used. The sensors closest to the beam pipe are exposed to higher occupancy and higher radiation damage. Therefore their strip pitch is $93.5 \text{ }\mu\text{m}$ while the outer sensors have a larger pitch of $187.5 \text{ }\mu\text{m}$. Granularity in the horizontal and vertical plane is achieved by orientating the first and last layer vertically and the second and third layer in $\pm 5^\circ$ with respect to the first and last layer. Figure 3.3 shows the stereo layers of the UT. [13]

Scintillating Fibre Tracker

The Scintillating Fiber Tracker (SciFi) is located downstream of the dipole magnet. The scintillating fibers have a diameter of $250 \text{ }\mu\text{m}$ and produce scintillating light when a charged particle traverses the detector. The scintillating light is transported to the top or the bottom of the fiber, where the light is collected by silicon photomultipliers (SiPM). The SciFi consists of three tracking stations, where each station is built similarly to the UT from 4 stereo layers. The first and last layer are orientated vertically and the second and third layer are orientated $\pm 5^\circ$ with respect to the vertical layers. The geometry of such a tracking station is shown in Figure 3.4. Each layer covers an active area of 30 m^2 . [13]

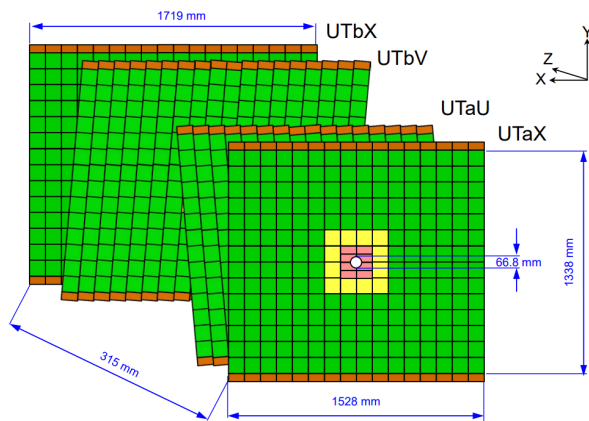


Figure 3.3: Scheme of the four UT layers. The different types of silicon strip sensors are color coded.

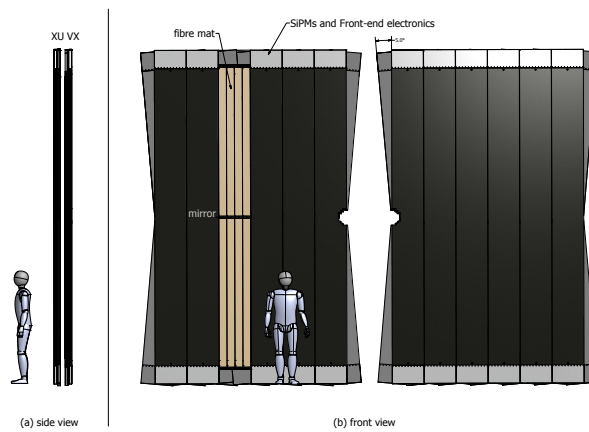


Figure 3.4: Schematic depiction of one SciFi tracking station.

3.1.2 Particle Identification

For B-physics it is important to reconstruct the B-meson from its decay products. For that, the types of the final state particles have to be determined. Particles can be identified via their mass or by a characteristic interaction which distinguishes them from other particle types. The mass m of a particle can be determined by its momentum p and relative velocity β :

$$m = \frac{p}{\beta\gamma c} \quad (3.1)$$

where c is the speed of light and γ the Lorentz factor.

The LHCb spectrometer uses two Ring Imaging Cherenkov detectors to identify charged hadrons by their mass. An electromagnetic shower in the electromagnetic calorimeter (ECAL) identifies electrons and photons, while hadrons leave a characterizing particle shower in the hadronic calorimeter (HCAL). Muons are minimum ionizing particles (MIPs) at LHC's energies which distinguishes them from other particles. They are identified by leaving tracks behind absorbers in the muon stations.

Ring Imaging Cherenkov Detectors

The Ring Imaging Cherenkov (RICH) detectors are used to distinguish charged hadrons by measuring the emission angle of the Cherenkov light. Cherenkov radiation is produced by a particle traversing a medium faster than the speed of light in this material. The emission angle of the Cherenkov light is dependent on the relative velocity β of the particle. Thus, by measuring the emission angle the particle's velocity can be determined. Together with the momentum measured by the tracking system, the velocity measurement is used to determine the mass of the particle following Equation 3.1. The Cherenkov light is detected using multi-anode photomultiplier tubes. LHCb uses two RICH detectors: RICH1 between VELO and UT and RICH2 downstream of the SciFi. To provide particle identification over a large momentum range, different radiator materials are used: RICH1 uses C_4F_{10} , which allows to distinguish charged hadrons with a momentum between 10 – 50 GeV/c while RICH2 uses CF_4 to cover a range of 15 – 100 GeV/c. [15]

Calorimeters

Downstream of RICH2, the electromagnetic (ECAL) and the hadronic calorimeter (HCAL) are located. The calorimeters are used to identify electrons, photons and hadrons and to measure their energy by using electromagnetic and hadronic particle showers. Therefore, both calorimeters are composed of alternating layers of scintillators and absorbers. The ECAL consists of 66 layers of 2 mm thick lead absorbers and 4 mm thick scintillating tiles. In contrast, the HCAL uses 16 mm thick iron absorbers and 4 mm thick scintillating tiles. The scintillation light is transported to light-detecting photomultiplier tubes via wavelength-shifting fibers. The amount of

scintillation light produced is proportional to the energy of the particle, such that the energy and the structure of the shower can be measured. [15]

Muon System

Muon candidates are detected by the four muon stations M2 – M5¹. Between each station 80 cm thick iron absorbers are placed, such that hadrons are filtered out. Only muons with momenta larger than 6 GeV/c can traverse all 4 muon stations. Since the particle density varies between the regions of the muon stations, 16 different types of multi-wire proportional chambers (MWPC) are used to measure the track and the penetration depth of muon candidates. [15]

¹Named M2 – M5 for historic reasons. Before upgrade I an additional muon station M1 was located upstream of the ECAL which was needed for the hardware trigger.

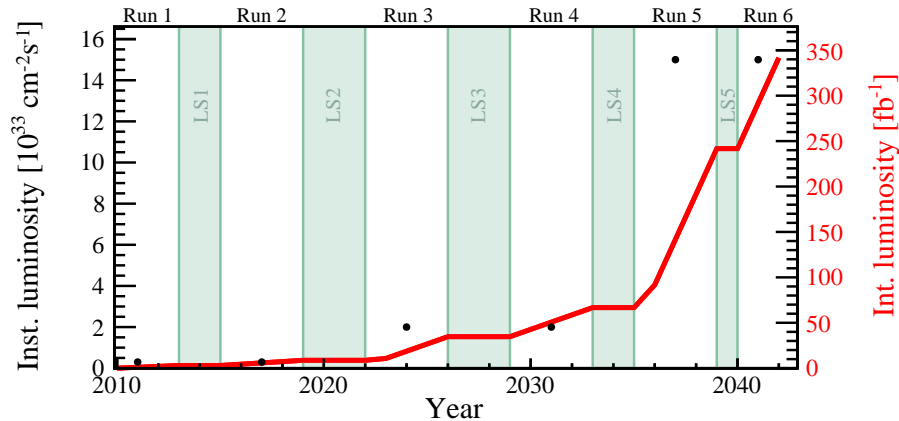


Figure 3.5: Luminosity and integrated luminosity at the LHCb detector against the LHC schedule. [16]

3.2 LHCb Upgrade II Plans

Upgrade II of the LHCb detector is planned for the long shutdown LS4 (2033–2035) and will allow LHCb to collect data at 5 times higher luminosities of $1.5 \times 10^{34} \text{ cm}^{-2} \text{ s}^{-1}$ (Figure 3.5). [17] With the increase of the instantaneous luminosity the occupancy in the different subdetectors will increase significantly. The total integrated luminosity of 180 fb^{-1} at the end of Run 5 will also increase the radiation damage for the different subdetectors. During the upgrade process all existing detectors will be replaced or modified to increase the rate capabilities and the radiation hardness. Similarly to Upgrade I, the planned Upgrade II detector will run with a software trigger. In addition, to the abilities for flavor physics, the installation of new detectors will make LHCb a multipurpose detector in the forward region. In the following, the proposed design of the detector which is shown in Figure 3.6 is described.

3.2.1 Detector Layout

The layout of the Upgrade II tracking system will be similar to the tracking setup of the current detector. Again, three subdetectors, VELO, UT and MightyTracker, the upgraded version of the SciFi detector, will be used. Additionally, the tracking system will be extended by so-called magnet stations. These magnet stations will cover tracks of low momentum particles leaving the acceptance of the spectrometer at the sides of the magnet. The particle identification system will consist of the two RICH detectors RICH1 and RICH2, the four muon stations M2-M5, the ECAL and a newly installed time-of-flight detector (ToF) using a TORCH (Timing Of internally Reflected Cherenkov photons) detector. The HCAL will be removed completely in favor of additional absorber material in front of the muon stations in order to reduce the hadronic background in the muon station, since the HCAL information was only needed for the hardware trigger used in the initial detector layout of Run 1 and 2.

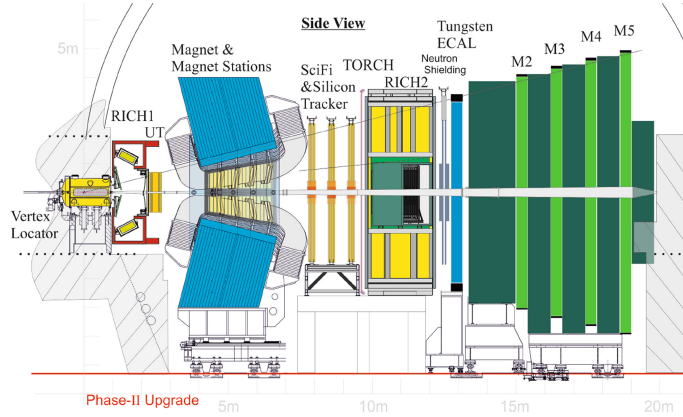


Figure 3.6: The foreseen baseline for the planned upgrade II (Run 5) detector layout of the LHCb experiment.[17]

3.2.2 MightyTracker

The MightyTracker (MT) will be the upgraded version of the SciFi detector. The 5 times higher luminosity would increase the occupancy in the inner part of the currently installed SciFi to a level where tracking is not possible anymore. Moreover, the strong irradiation in Run 5 would quickly damage the inner part of the detector significantly [18]. By constructing only the inner and middle part (cyan and magenta in Figure 3.7) of the tracking station with silicon pixel detectors this effect can be reduced, since for the outer parts of the tracking station the SciFi technology is still a viable option. Even so, the radiation damage is too large for the currently installed SiPMs. Different options to replace the SiPMs are discussed. As one mitigation measure to reduce the thermal noise created by the radiation damage the operation of the SiPMs at cryogenic temperatures of about $-150\text{ }^{\circ}\text{C}$ is proposed.

For the silicon sensor part of the MightyTracker High-Voltage Monolithic Active Pixel Sensors (HV-MAPS) are proposed. Because of their monolithic structure HV-MAPS have a lower material budget than other types of silicon sensors, reducing scattering and absorption effects. HV-MAPS are produced in a commercial HV-CMOS process, making them less expensive than other types of pixel sensors and intrinsically radiation-hard. An introduction into this technology is given in Chapter 4. Currently it is planned to equip each tracking station with two staggered layers of MightyPix sensors, resulting in a total of 6 layers of silicon sensors. Each layer will cover an area of 3 m^2 , resulting in 18 m^2 of silicon pixel detectors in the MightyTracker.

Since the MightyPix sensors have to cope with the 25 ns bunch structure of the LHC, they have to fulfill several performance requirements. The time resolution of the MightyPix sensors is required to be below $\sigma_t \lesssim 3\text{ ns}$ to match hits to the correct 25 ns bunch crossing window of the LHC at a confidence of 99%. A pixel pitch of

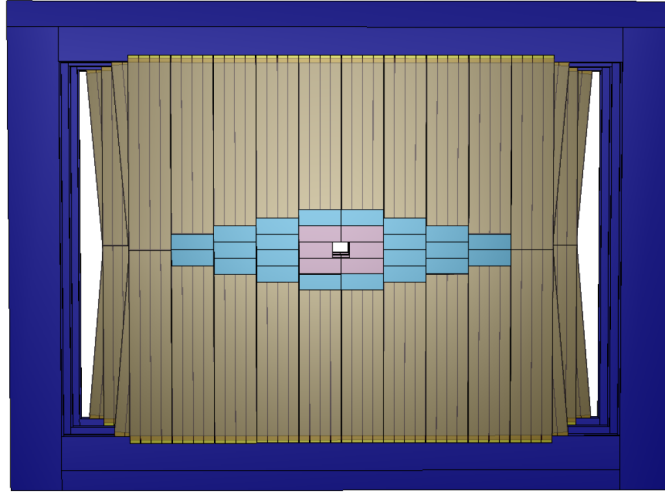


Figure 3.7: The three tracking stations of the Mighty Tracker. The SciFi modules are shown in brown and the MightyPix modules of the inner and middle tracker are shown in magenta and cyan.[17]

$50 \times 150 \mu\text{m}$, which is used by previous prototypes, provides a sufficient spatial resolution for a high tracking performance. The MightyPix sensors closest to the beam pipe (magenta in Figure 3.7) will detect a mean of 1.7 particle per non-empty bunch crossing, resulting in a mean particle rate of 50 MHz on the sensor. Furthermore, the sensors in the inner part of the MightyTracker need to withstand a radiation damage of 1 MeV neutron equivalent fluence of $6 \times 10^{14} \text{ n}_{\text{eq}}/\text{cm}^2$. Lastly, the material budget of the silicon sensors and their support structure should be equal or less than 1% of a radiation length. Currently it is planned to use 100 μm thick sensors in the MightyTracker. Therefore, the sensors contribute to the material budget with 0.11 % of a radiation length, which is 4 times lower than the material budget of the hybrid pixel sensor VELOPix with 0.44 % of a radiation length. [17][19]

4 Particle Detection

Particles are detected by energy loss in the detection material. The most common processes of particle detection in silicon-based tracking detectors are listed in the following sections. The third section of this chapter gives a short introduction into the working principle and types of semiconducting sensors.

4.1 Charged Particle Interaction in Matter

A particle traversing a detector can interact with its material. The most common type of interaction of charged particles with matter is electromagnetic interaction.

4.1.1 Ionization

Charged particles traversing a material ionize atoms of the material along their track and transfer some of their energy to the material. For charged particles, this energy loss due to ionization is described by the Bethe-formula [21]. The mean energy loss per distance $\langle \frac{dE}{dx} \rangle$ is given as

$$-\left\langle \frac{dE}{dx} \right\rangle = Kz^2 \frac{Z}{A} \frac{1}{\beta^2} \left[\frac{1}{2} \ln \left(\frac{2m_e c^2 \beta^2 \gamma^2 E_{\max}}{I^2} \right) - \beta^2 - \frac{\delta(\beta\gamma)}{2} \right] \quad (4.1)$$

where K is a constant ($K = 0.307 \text{ MeVcm}^2/\text{mol}$), z the charge of the particle in electron charges e , Z the atomic number and A the relative atomic mass of the material, I the mean ionization energy of the material, E_{\max} the maximal energy transfer to the material and δ is the so called density-correction. The Bethe-formula shows a dependence on the relative velocity β of the traversing particle and the Lorentz factor γ . The formula is valid between $0.1 < \beta\gamma < 1000$ [20]. Typically, the energy loss due to ionization is expressed normalized to the density of the material ρ and in dependency of either $\beta\gamma$ or the particle momentum following Equation 3.1. The energy loss due to ionization is shown in Figure 4.1 for different materials.

Particles with a $\beta\gamma = 3$ lose the least amount of energy by ionization, typically $1 - 2 \text{ MeV cm}^2/\text{g}$, hence they are called minimum-ionizing particles (MIP). Since they lose the least amount of energy in the detector material, a tracking detector has to be designed in such a way that it is able to detect MIPs. A MIP loses a mean energy of about $390 \text{ eV}/\mu\text{m}$ by ionization in a silicon detector [22]. For particles with a $\beta\gamma$ lower than a MIP, the Bethe formula is dominated by the $\frac{1}{\beta^2}$ -part leading to an increased energy deposit for lower momenta. In contrast, the energy deposition of

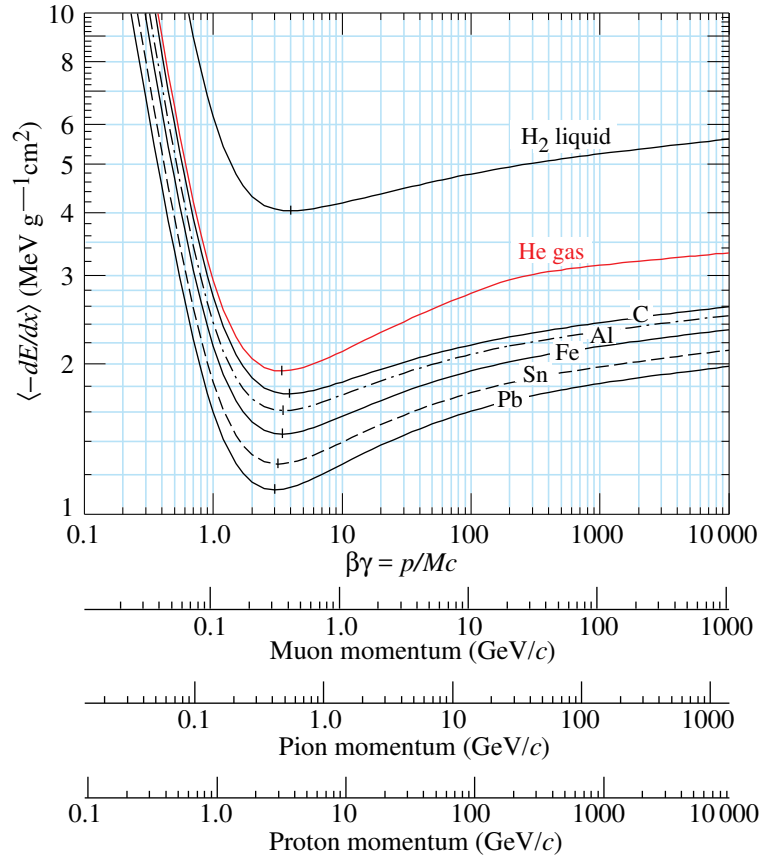


Figure 4.1: Energy loss by ionization dependent on $\beta\gamma$ and on the momentum for muon, pion and proton in different materials. [20]

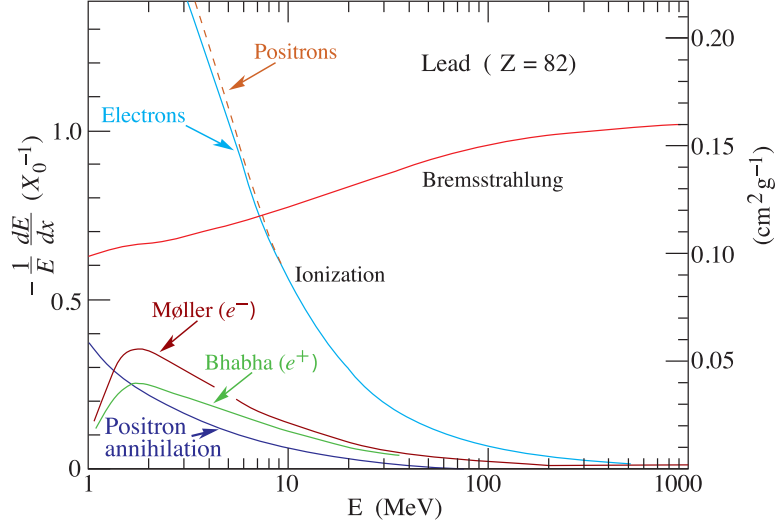


Figure 4.2: Total energy loss and energy loss per interaction type of electrons and positrons in lead depending on the particle energy. [20]

particles with higher momenta than a MIP increases logarithmically with momenta, since the term $\ln(\beta^2\gamma^2)$ is dominant. The statistical distribution of the energy loss by ionization in a thin detector is described by the Landau function [23], which is an asymmetric function with a tail structure to higher values. Therefore, the mean energy loss by ionization is larger than the most probable energy loss.

δ -Electrons

The tail structure of the ionization distribution is caused by the creation of so-called δ -electrons. These electrons are bound in the atomic shell of the material and are lifted into an unbound state by an interaction with a particle traversing the material. After their creation δ -electrons lose energy by ionization in the detector material and are absorbed in the detector material in most cases.

Ionization by Electrons and Positrons

As a result of their much lower mass the energy loss of electrons and positrons can not be completely described by the Bethe equation, since the energy loss by bremsstrahlung is predominant for large momenta. This effect is visualized in Figure 4.2. The critical energy, where bremsstrahlung predominates the energy loss by ionization, is 40.2 MeV for electrons in silicon and 582 GeV for muons. [22]

4.1.2 Bremsstrahlung

Bremsstrahlung occurs when a highly relativistic charged particle ($\beta \approx 1$) passes the Coulomb field of a nucleus. The electromagnetic interaction between a particle

and a nucleus of the material leads to the emission of a photon, the so-called bremsstrahlung photon. Thus, the incident particle loses energy to the photon. The energy loss dE/dx of a particle with energy E can be approximately described by a radiation length X_0 :

$$\frac{dE}{dx} = -\frac{E}{X_0} \quad (4.2)$$

The radiation length X_0 is a material property. For example, a silicon detector has a radiation length of about 9.36 cm. [22]

4.2 Interaction of Photons with Matter

Photons can interact with matter in three ways: Photo absorption, inelastic scattering (Compton scattering) or pair production. Photo absorption is the predominant process for photons in silicon with an energy below $E_\gamma \approx 100$ keV. Since within the scope of this thesis only photons with a maximum energy of 35 keV are used, Compton scattering and pair production are not discussed here.

A photon is absorbed in matter if its energy is high enough to lift an electron bound in an atom of the material into an unbound state. This unbound electron loses energy in the material due to ionization. The absorption cross section σ is dependent on the photon energy E_γ and the atomic number of the material Z [22]:

$$\sigma \sim E_\gamma^{-7/2} Z^5 \quad (4.3)$$

4.3 Semiconductor Sensors

4.3.1 Working Principle

A semiconductor is a solid material whose valence band states are fully occupied, such that the conduction band is empty at temperature $T = 0$ K. Because of the small band gap between valence and conduction band in semiconductors, electrons can move from the valence band into the conduction band leaving a positive ion (hole) in the valence band at temperatures above 0 K. Thus, semiconductors become conductive with an intrinsic resistivity typically between $10^{-3} - 10^8 \Omega \text{ cm}$ at room temperature. Silicon is the most common used semiconducting material for particle detection. [22]

Doping

At room temperature the intrinsic charge carrier density of silicon is too low to act as a conductor. The charge carrier density can be increased by adding so-called dopants to the semiconductor causing a defect in its crystal structure. Dopants are different elements with more or less valence electrons than silicon. Elements adding

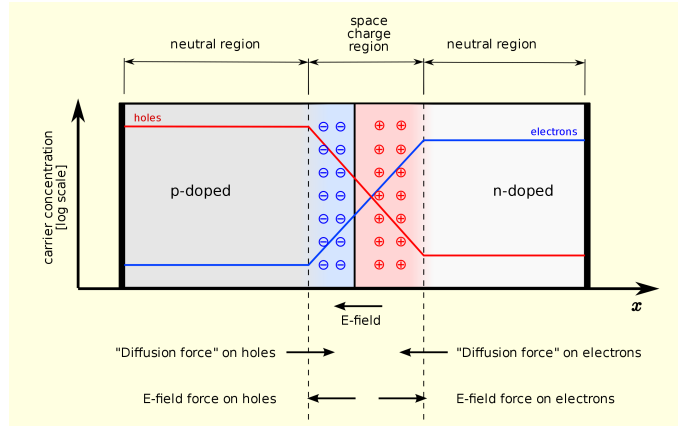


Figure 4.3: Schematic of a pn-junction in thermal equilibrium. [24]

additional electrons to the conduction band of the semiconductor are called donors. In contrast, acceptors are elements which add an additional hole to the material by capturing a valence electron of a neighboring silicon atom. A semiconductor doped with donors is called n-doped while a material doped with acceptors is called p-doped.

pn - Junction

The contact zone between a p-doped and an n-doped substrate is called pn-junction, which is also known as diode. Positive holes diffuse from the p-doped part to the n-doped part while electrons diffuse from the n-doped to p-doped substrate. At the pn-junction electrons and holes can recombine with each other, such that a charge-free region between the doped substrates is created, the so-called depletion zone. Due to the recombination of electron-hole pairs, the charge of the p- and n-dopants in the depletion zone is not compensated by the free charge carriers in the conduction band. Hence, a negative and positive space charge is created respectively. Between the negative space charge in the p-doped part and positive space charge in the n-doped part of the depletion zone a potential, the so-called built-in voltage, is created resulting in an electric field. The electric field creates a drift current of electrons and holes which cancels the diffusion current. A pn-junction in this equilibrium is shown in Figure 4.3. If an additional external bias voltage V_{bias} is applied to the pn-junction in direction of the built-in voltage V_0 , the size of the depletion zone and the electric field strength are increased. The width of the depletion zone w is approximated by:

$$w = \sqrt{\frac{2\epsilon_0\epsilon(V_{\text{bias}} - V_0)}{e} \frac{N_A + N_D}{N_D N_A}} \quad (4.4)$$

where ϵ_0 is the vacuum dielectric constant and ϵ is dielectric constant of silicon, e is the electron charge, N_D is the donor density and N_A is the acceptor density. [25]

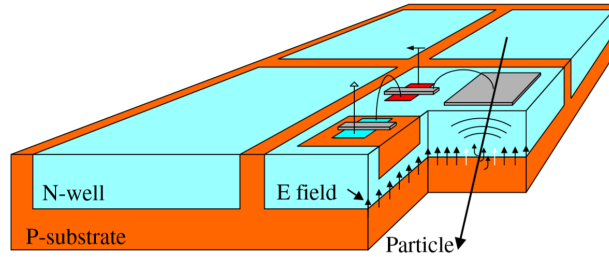


Figure 4.4: Conceptual scheme of an HV-MAPS detector.[7]

In a silicon detector the depletion zone acts as the particle detecting volume. The energy loss of a particle traversing the depletion zone creates free electron-hole pairs. In silicon with a small band gap of 1.12 eV, a mean energy transfer of only 3.65 eV to the material is required to create 1 electron-hole pair at $T = 300$ K. [22]

4.3.2 Silicon Pixel Detectors

Silicon pixel detectors are widely used in particle physics. All of the four large LHC experiments use pixel sensors in their detectors. Pixel sensors can be divided into two categories: Hybrid and monolithic pixel sensors.

Hybrid pixel detectors like the VELOPix [26] consist of a sensor chip and a readout chip, which are bump-bonded together. The sensor chip contains the charge-detecting diodes in a pixel structure, while the readout chip contains the front-end electronics to read the pixels. This type of sensor shows an excellent performance for particle tracking. The diodes of hybrid pixel sensors can be depleted with a high bias voltage resulting in a high signal to noise ratio. However, the production of these types of sensors is costly and difficult. Moreover, the two-chip approach leads to an increased material budget and thus increased multiple scattering deteriorates the spatial resolution.

In contrast, monolithic sensors consist of only one chip, which contains the charge-detecting diode and the readout electronics in the same pixel, reducing the material budget and the production cost of the sensor. Since the depletion zone and the amplifying-transistors needed for the readout share the same substrate, the monolithic sensors are not as radiation-hard as hybrid sensors.

4.3.3 HV-CMOS High-Voltage Monolithic Active Pixel Sensors

High-Voltage Monolithic Active Pixel Sensors (HV-MAPS) [7] are monolithic sensors produced in a commercial HV-CMOS process.

Signal Generation

Every pixel of an HV-MAPS contains a diode detecting the energy loss of a particle. The diode of HV-MAPS can be biased with a high voltage, which distinguishes them from MAPS like the ALPIDE [27] sensor used in the ALICE experiment. This difference between HV-MAPS and MAPS is caused by the production process of these sensors. MAPS are produced in a CMOS process with a small epitaxial layer. On the other hand, HV-MAPS are produced in a commercial 180 nm HV-CMOS process developed for automotive industries allowing to deplete the pn-junction with much higher voltages than the standard CMOS process. A scheme of an HV-MAPS sensor is shown in Figure 4.4. The detection volume of an HV-MAPS, the pn-junction, is created at the junction of the p-substrate (orange in Figure 4.4) and the deep n-wells which form the pixels of the sensor (blue in Figure 4.4). The pixel diode is typically depleted by a bias voltage of up to 100 V. When a particle traverses the depletion zone of an HV-MAPS electron-hole pairs are created by ionization. Because of the applied bias voltage in the depletion zone, the electrons and holes drift to the positive and negative electrodes creating the field respectively. Following the Shockley-Ramo theorem [28], these drift currents induce a signal on the electrodes, which can be read out by signal processing electronics in the pixels.

Every pixel includes an in-pixel amplifier circuit creating an electronic pulse from the charges collected in the pixel diode. Typically, a comparator applies a threshold to the amplified pulse to suppress noise hits. Depending on the specific sensor design this comparator circuit is also included in the pixel structure or is located in the peripheral structure of the sensor. The signals from the pixels are sent to a peripheral readout structure via metal layers, where the hits are digitized. The transistors used for the in-pixel circuits are placed in shallow wells in the deep n-wells. NMOS transistors are placed in a shallow p-well, while PMOS transistors are placed in a shallow n-well. Depending on the specific sensor design, the shallow n-wells are placed directly in the deep n-well, which leads to a capacitive coupling between the PMOS transistor and the diode, or a deep p-well is placed between the two n-wells reducing the capacitive coupling between the shallow and deep n-wells.

Time-over-Threshold & Timewalk

The charge pulse generated in the depletion zone is typically amplified and a comparator is used to apply a threshold to the amplified pulse to suppress noise hits. A comparator has a high output as long as the amplified pulse is above the threshold. When a comparator signal is further processed, the rising edge of the comparator pulse contains the time information of a particle hit and is typically named time-of-arrival (ToA or TS1). Since the rise time of the amplifier signal depends on the pulse height, large signals pass the threshold earlier than small signals. Hence, large signals are detected earlier than small signals. This effect known as timewalk leads to a decreased time resolution of the sensor. A scheme of the timewalk effect is shown in Figure 4.5. However, the timewalk effect can be corrected, when the pulse height

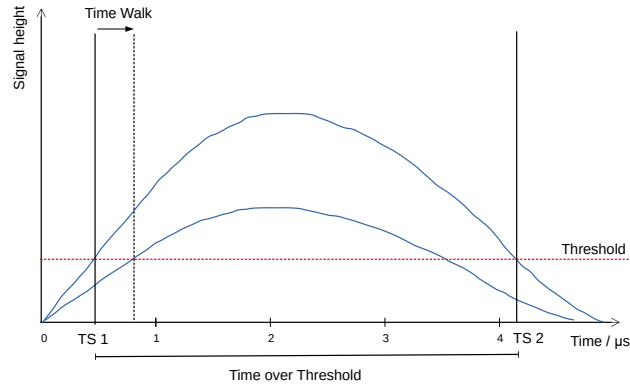


Figure 4.5: Scheme of two arbitrary amplifier pulses depicting time-over-threshold and timewalk.

of the signal is known. The pulse height of the signal is linearly dependent on the time the signal is above the threshold, the so-called time-over-threshold (ToT). This time information can be obtained by recording the trailing edge of the comparator pulse, the time-over-threshold timestamp (ToT or TS2)¹. The time-over-threshold can be determined from the difference of both timestamps:

$$\text{ToT} = \text{TS2} - \text{TS1} \quad (4.5)$$

Due to saturation effect in the amplifier circuit, both the pulse height and the ToT may not be linearly dependent on the energy deposition in the pixel diode.

¹To avoid ambiguities ToT is used as an abbreviation of the time-over-threshold and TS2 of the trailing edge timestamp in the following.

5 HV-CMOS Sensor ATLASPix3.1

ATLASPix3 (AP3) and ATLASPix3.1 (AP3.1) are full-scale prototypes of a triggered HV-MAPS sensor for the inner tracker of the ATLAS experiment at CERN [30]. AP3 and AP3.1 differ only in minor changes in the structure of the sensor and do not lead to major performance differences between AP3 and AP3.1. Therefore, the abbreviation AP3 includes both versions of the sensor in the following description of them. Although the AP3 is designed for triggered readout, it contains an additional untriggered readout structure, which is similar to the Mu3e¹ prototype MuPix8 [31]. The ATLASPix3 consists of 49104 pixels with a pixel pitch of $150 \times 50 \mu\text{m}^2$ in 132 columns and 372 rows, resulting in an active area of $19.8 \times 18.6 \text{ mm}^2$ as shown in Figure 5.1. At the bottom of the active area, a 2 mm high peripheral structure contains the triggered and untriggered pixel readout, the DAC (digital to analog converter) registers and the configuration unit. The hits are read from the pixels column-wise and are sent to a data acquisition system (DAQ) by low-voltage differential signaling (LVDS) at a nominal link speed of 1.28 Gbit/s. [29][32]

¹Mu3e is an experiment at the Paul Scherrer Institute (PSI) studying the rare decay $\mu^+ \rightarrow e^+e^-e^+$.

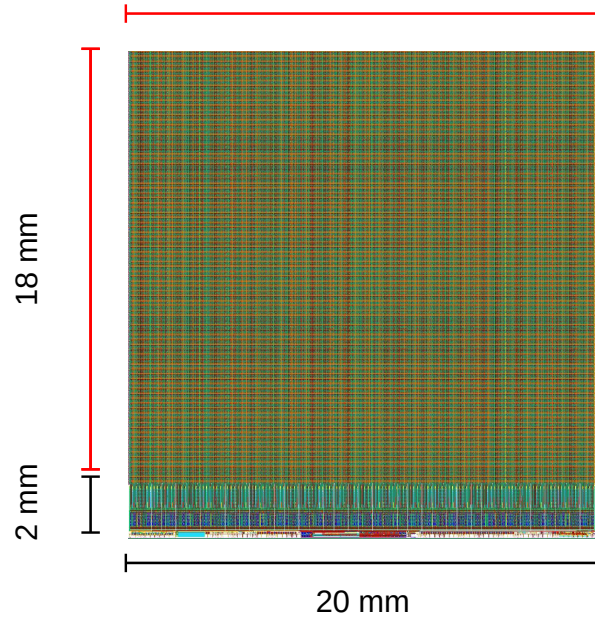


Figure 5.1: Layout of the HV-MAPS prototype ATLASPix3(.1). The active area is indicated in red, while the periphery is indicated in black. Adapted from [29]

Parameter	Function
Th	External applied reference voltage to comparator
Bl	Baseline voltage of the comparator
Blres	Baseline Restoration
Inj	Injection pulse amplitude
VPLoad	Load of the amplifier
VNFb	Fall time of the amplifier
VNFoll	Feedback stabilization
TDAC	Threshold tuning
VNDAC	Tuning range of TDAC's
VNbiasRec	Input level signal receiver
VPbiasRec	Input level signal receiver

Table 5.1: Selection of parameters of AP3.1.

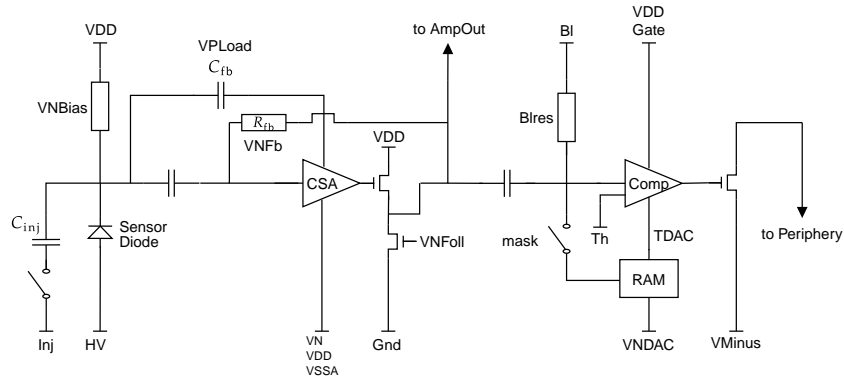


Figure 5.2: In-pixel circuit of the AP3(.1).

Voltage	Function
HV	Bias voltage
VDD	Pixel power domain
VSSA	Amplifier supply voltage
VMinus	Ground level of the signal line
Gate	Load of the NMOS comparator

Table 5.2: Voltages applied to the ATLASPix3.1 sensor.

5.1 Pixel Matrix

Every pixel of the ATLASPix3 contains a charge-collecting diode, the pn-junction where the energy loss of a particle is detected. The particle detecting diode of the AP3 is depleted by a reverse-biased high voltage of $HV \approx -60$ V. As discussed in Section 4.3.3 all the in-pixel electronics is located within this diode. The pixel electronics consist of a PMOS charge sensitive amplifier (CSA), an NMOS comparator and a RAM (Random-Access Memory) for the tunable pixel threshold. Figure 5.2 shows the circuit of an AP3 pixel. The tuneable voltage parameters described in this chapter are shown in Table 5.1 while the voltages supplied to the sensor are shown in Table 5.2.

Analog Circuit

The charge pulse created by the pixel diode is amplified by the CSA. The rise time of this pulse is determined by the feedback capacitor C_{fb} , which leads to an exponential rise of the signal. The fall of the signal is determined by a linear feedback created by the resistor R_{fb} , which is tunable with parameter $VNFB$. Typically, the rise time is



Figure 5.3: Test outputs of AP3.1 measured with an oscilloscope. Blue shows the injection pulse created by discharging the injection capacitor. Yellow: Amplified injection pulse. Magenta: Digital signal of the comparator caused by the injection pulse. The comparator pulse is shaped by the receiver unit in the periphery.

of the order of $\mathcal{O}(10 \text{ ns})$ while the falling time is of the order of $\mathcal{O}(1 \mu\text{s})$. The pulse shape of the amplifier output with its exponential rise and linear fall can be seen in yellow in Figure 5.3. To stabilize the feedback, a tunable source follower *VNFoll* is implemented.

Digital Circuit

The amplified pulse is capacitively coupled to the baseline of the comparator circuit. The baseline is supplied via the tunable voltage *Bl*. This voltage is generated on-chip using the power domain *VDD*. The restoration of the baseline can be tuned using the parameter *BLres*. The comparator applies a threshold to the signal and creates a digital signal. The threshold of the comparator is externally applied to the pixel via a tuneable voltage DAC (VDAC) *Th*. Since the amplifier amplitude and threshold may vary between pixels, an in-pixel threshold tuning is implemented. The so-called 3-bit tune DAC (TDAC) values can shift the height of the threshold for each pixel separately. The tuning range of the TDAC can be set with the parameter *VNDAC*. The TDAC value of a pixel is stored in its pixel RAM. An additional bit of the pixel RAM, the *mask bit*, is used to disable the pixel's comparator, which is for example needed if the pixel measures very high electronic noise. Because of the NMOS-type structure of the comparator, the current flow through the comparator has to be regulated via an external load. In the AP3 sensor, an externally provided voltage

Gate realizes the load. A comparator pulse of the AP3.1 can be seen in magenta in Figure 5.3.

The digital comparator signal is sent to the peripheral readout structure along the column as shown in Figure 5.4. The high level of this signal is given by the voltage VDD and the low level is given by the voltage $VMinus$:

$$\text{LowLvl} = V\text{Minus} \quad (5.1)$$

$$\text{HighLvl} = VDD \quad (5.2)$$

The line driver voltage $VMinus$ can be created on-sensor using the VDAC *minus* or can be applied externally. The signal lines connecting the pixels with the peripheral readout structure are all of the same length to reduce a row-dependent delay structure in the timing of the signal.

Test Outputs

For testing purposes, the amplified pulses behind the CSA can be accessed using the *AmpOut* test line for pixels in row 0. The digital signals of the comparators in one column can be accessed using the *HitBus* test output for all columns. Since *HitBus* test output is located behind the receiver unit in the periphery, the signal seen at the test output is shaped by the receiver circuit. So-called injection pulses can be injected into the pixel readout structure by discharging a capacitor C_{inj} to test the analog and digital in-pixel circuits of every pixel. The negative amplitude of the discharge of the capacitor can be seen in cyan in Figure 5.3. The strength of such a test pulse can be controlled using the VDAC parameter *Inj* or using an external pulse generator.

5.2 Readout

The structure of the pixel readout of the ATLASPix3 sensor is shown in Figure 5.4. The digital signal sent from the pixels along the columns to the periphery is digitized by a receiver circuit. The input level of the receiver can be tuned using the parameters *VNBiasRec* and *VPBiasRec*. The receiver digitizes the leading- and trailing-edge timestamp of the comparator signal and stores the time information in a hit buffer. Since each pixel has one corresponding hit buffer in the periphery, only the timestamp information is saved in the buffer. The hit information is further processed column-wise by the readout system. Since the ATLASPix3 contains a triggered and an untriggered readout mode, two different structures can be used to read the hit information from the hit buffers.

5.2.1 Untriggered Readout

In case of the untriggered readout structure the information in the hit buffers is processed further by an end-of-column structure (EoC). All 372 pixels in one column share a fixed EoC. In one readout cycle of the finite state machine (FSM) one hit data per column can be shifted from the hit buffers into the EoC. This process is done simultaneously for every column with hits in their hit buffers. Which non-empty hit buffer is read in a column is determined by the spatial position of the hit buffers. The priority order of this process can be expressed in terms of the row address of the pixel corresponding to the hit buffer: The priority order starts at row 185 and goes from there to row 0. After row 0 the priority order continues at row 186 and goes to row 371. After the hit information is shifted to the EoC, the finite state machine reads the hit information from the EoC starting in column 131 and ending in column 0. The hit information is encoded via 8b/10b aurora encoding and is sent to the DAQ system by the FSM. The data is sent to the DAQ system at both edges of the readout clock (640 MHz)² resulting in a nominal data rate of 1.28 Gbit/s. After that, the FSM restarts its readout cycle with loading the hit information from the hit buffers in the EoC.

5.2.2 Triggered Readout

The triggered readout is structured differently. The hit information in the hit buffers is processed by content-addressable memory (CAM) buffers, the so-called trigger buffers. These buffers are used to store up to 80 hits per column until a trigger with matching timestamp arrives. The priority order, in which hit information is transferred from the hit buffers to the CAM, is similar to the priority order in the untriggered readout. Moreover, the trigger buffers are used to group hits into events, which will be sent to the DAQ system together. The trigger decision sent to the sensor is stored in a trigger table for a given trigger delay time, since the hit

²see Section 5.3.

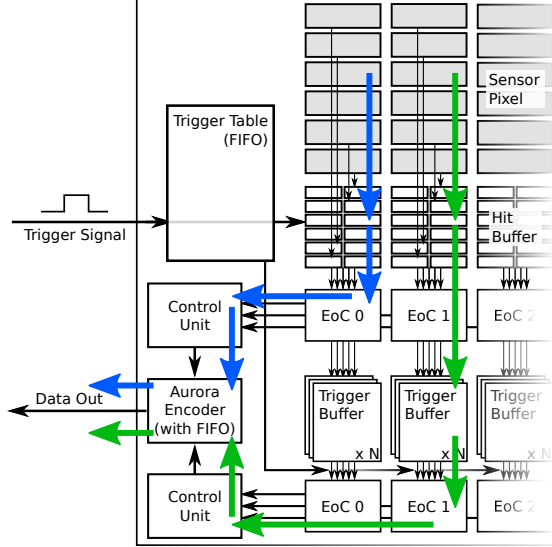


Figure 5.4: Scheme of the readout periphery of AP3(.1). Data flow of the untriggered readout shown in blue and triggered in green. [32]

data from the pixels typically arrive later than the trigger. After the delay time, events with matching timestamp to the trigger, are shifted in the EoC. Similarly to the untriggered readout structure the hit data is read from the EoC sent to DAQ system. However, the hit information is encoded to 64b/66b aurora encoding instead of 8b/10b, because a different data format is necessary for the event building.

5.3 Clock Distribution

The readout clock of ATLASPix3 sensor can be provided in three ways: As reference clock for the PLL (Phase-locked loop), as CMD interface and as external signal. Nominally, this clock should run at 640 MHz. From the readout clock, the clocks of the readout control units (CU) of the triggered and untriggered readout are derived. The triggered control unit is 4 times slower than the readout clock (160 MHz) and the untriggered 5 times slower (128 MHz). The control unit clock provides the clock for the state machine for both readout modes. The FSM clock speed f_{SM} can be tuned by the *timerend* setting:

$$f_{SM} = \frac{f_{cu}}{2(1 + timerend)} \quad (5.3)$$

Due to timing constrains in the routing of the FSM of the untriggered readout, the FSM is not able to run at its frequency of 64 MHz and has to be slowed down by a factor of 2 using the *timerend* = 1 setting. It is observed that the FSM is working correctly up to a frequency of 40 MHz.

Additionally, the timestamp clocks are derived from the control unit. In untriggered readout the timestamp clock f_{TS} has the same clock speed as the control unit (128 MHz). In contrast, the timestamp clock of the triggered readout is 4 times slower than its control unit (40 MHz). The clock speed of TS1 f_{TS1} and TS2 f_{TS2} can be tuned by the parameters $ckdivend$ and $ckdivend2$, respectively:

$$f_{TS1} = \frac{f_{TS}}{1 + ckdivend} \quad (5.4)$$

$$f_{TS2} = \frac{f_{TS}}{1 + ckdivend2} \quad (5.5)$$

To calculate the ToT correctly TS2 has to be slowed down, such that the maximum time-over-threshold is smaller than the interval of the 128 TS2 steps. The slow-down parameter $ckdivend2$ has to be chosen, such that there are no ambiguities when calculating the time-over-threshold. The possible values can be derived in the following way:

$$\log_2 \left(\frac{ckdivend2 + 1}{ckdivend + 1} \right) \in \mathbb{N}_0 \quad (5.6)$$

5.4 MightyPix v1

The MightyPix v1 is the first prototype dedicated to the MightyTracker project. The prototype was submitted to production in May 2022 and is expected to arrive in December 2022. The pixel structure will be similar to the AP3. However, both the amplifier and the comparator, are CMOS-based. The CMOS-based pixel electronics will increase the radiation hardness, reduce the timewalk and the delay of the signals. Moreover, the pixel matrix is reduced to 29×320 . This should increase the hit rate capability of the MightyPix in respect to the AP3 by a factor 4, since the active area read by the readout structure is reduced by the same factor. In later iterations of the MightyPix sensors four of this pixel matrices will be combined to one sensor with four readout structures with one data link each. The pixel pitch of the MightyPix v1 is $165 \times 55 \mu\text{m}^2$ resulting in an active area of $4.8 \times 17.6 \text{ mm}^2$. It is foreseen that the pixel diode can be biased with a high voltage above -120 V , which reduces the sensor capacitance and increases the signal to noise ratio. In contrast to the ATLASPix3, the MightyPix contains only an untriggered readout structure, which can be accessed using a LHCb-like readout like a LpGBT-board (Low Power GigaBit Transceiver). [33]

6 Measurement Setup

The goal of this thesis is to develop different measurement setups for studying HV-MAPS prototypes for the LHCb MightyTracker. The ATLASPix3.1 sensor, a predecessor of the MightyPix, is tested in this thesis. The sensor is read out by the GECCO readout system, which is described in the next section. The second section of this chapter describes the different electronic signal and particle sources used to test the AP3.1, while the third section depicts the configuration of the sensor used for the measurements.

6.1 GECCO Readout System

The GECCO (GEneric Configuration and COntrol) system [34] is a data acquisition (DAQ) system for HV-MAPS. It was developed by Felix Ehrler and Rudolf Schimassek at KIT (Karlsruhe Institute of Technology). The GECCO system is designed to read out the ATLASPix1 and ATLASPix3 prototypes, but has been adapted to other HV-MAPS developed at KIT like the HITPix and the ASTROPix. [32][35] The system contains a single-sensor setup and a telescope setup with 4 sensor layers. The single-sensor setup can be used to determine the characteristics of one sensor, like the signal response or the hit rate capabilities. In contrast, the telescope setup can be used to study the time resolution and hit efficiency of a sensor under test using particle beams. Three of the four layers of the telescope can be used as tracking and time reference, while the time resolution and hit efficiency of one sensor layer is studied. Since only the single-sensor setup is used within the scope of this thesis, the telescope setup is not explained.

6.1.1 Hardware

The hardware of the GECCO system consists of three parts, which are shown in Figure 6.1. The first part is the carrier board. The sensor under test, here the AP3.1, is attached and bonded to this carrier board. On the board are probe pins for the different externally applied voltages, which can be used for testing purposes. In addition, the shift registers used for writing the configuration to the sensor are placed on the carrier board. The carrier board is connected to the GECCO board via a PCIe \times 16 connector, which routes the voltages and the differential lines used for configuration and data output. The GECCO board is used to apply the external voltages and contains the more expensive components, for example LVDS receivers, needed for the connection between sensor and FPGA (field-programmable gate array), which is used to control the sensor. The GECCO board is connected to

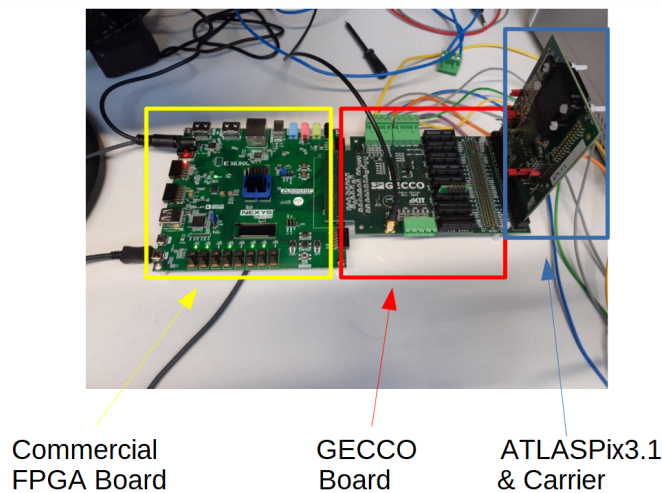


Figure 6.1: Picture of the GECCO DAQ system for AP3(.1).

the FPGA via FMC (FPGA Mezzanine Card). The FPGA is used to configure the sensor and to process the data before sending it to the computer, where the data is written to the hard drive. The FPGA used in the GECCO system is a commercial Artix-7 on a Nexys video development board [36].

6.1.2 Firmware

The firmware on the FPGA that is used to control the sensor is written in Verilog¹. The firmware can be divided into three main firmware modules. One is the configuration module sending commands received from the computer to the configuration modules of the sensor. The configuration is done by two independent firmware modules: writing via shift-registers or SPI (Serial Peripheral Interface) protocol. The main module of the firmware is the readout. The readout receives the data from the sensor, decodes it and writes it to the FIFOs (First In First Out)² of the communication modules. In the readout module of the firmware the timestamps TS1 and TS2 of the sensor are extended from 10 bit (1024 clks)³ and 7 bit (128 clks) to 40 bit (10¹² clks) to achieve a time ordering of the data at FPGA level. Additionally, the readout module includes a trigger module, which can be used to include trigger information into the data stream to provide an external time reference. The communication to the computer used to control the measurement can be established via Ethernet or USB. Each connection type has its own firmware module, which can be used simultaneously. However, the Ethernet connection can be only used to read the data output but not to configure the sensor. Additionally, the FPGA is used

¹Verilog is a standardized hardware description language.

²A FIFO is a data buffer.

³clks: Clock cycles of the timestamp.

to provide the readout clock of the pixel sensor AP3. In the GECCO system, the FPGA provides a 200 MHz external clock as the readout clock for the sensor, resulting in a 400 Mbit/s data rate, since the data is sent at both edges of the readout clock.

The firmware of the GECCO system is improved in this thesis to increase the clock speed (and readout speed) from 200 MHz to 400 and 600 MHz. The clock speed can not be increased to reach the maximum AP3 clock speed of 640 MHz, since the FPGA used in the GECCO system can not provide higher clock frequencies. Additionally, changes are applied to the readout module of the firmware to provide a data arrival timestamp in the FPGA. Although not used here, the trigger information in the firmware of the untriggered readout is improved, which can be used for a time resolution measurement with a scintillator as time reference for example.

6.1.3 Control Software

The control software is the visual interface to the user. In the control software, the user sets the DAC values and configuration of the sensor. Additionally, the control software writes the data stream coming from the FPGA to the hard drive. It is possible to decode the data stream from binary to decimal data during the storing process. Online monitoring of the measurement and debugging features are implemented as well. In addition, measurement routines are implemented. Moreover, the control software is written in a way that it is easily adaptable to extend the catalog of measurement routines.

UDP Readout

Another part of the control software is the UDP readout protocol, which is used for the Ethernet connection between computer and FPGA. This readout software is excluded from the main control software. The UDP readout software uses two different threads on the computer to read the data from the FPGA and write it onto the hard drive to achieve the highest possible data rate in the storing process. Hence, only the binary data stream from the FPGA is written to storage without an online decoding. Online monitoring of the data taking and the beam profile are implemented as well.

6.2 Signal & Particle Sources

A signal to determine the sensor characteristics of an HV-MAPS can be created in various ways. Electronic injection pulses can be used to determine the threshold of the pixels, while particles from radioactive sources can be used to determine the energy response of the sensor under test. Photons from an X-ray tube can be used to study hit rate dependent effects in the data taking of HV-MAPS. Large energy depositions in the sensor and their impact on the sensor response can be analyzed with ion beams. The following sections describe the different sources used in this thesis to create a signal in the sensor.

6.2.1 Injection Pulses

Injection pulses created on the sensor (Section 5.1) can be used to characterize the sensor. The chip allows to inject an electronic pulse into the amplifier circuit independent of a charge deposition in the pixel diode. The pulse height can be chosen with a small variation in amplitude and allows to characterize the behavior of the amplifier and comparator circuit at a chosen signal height. For example, the injection pulses are used to determine the threshold of a pixel.

6.2.2 Radioactive Particle Sources

For measurements in the lab two radioactive sources are used: Iron-55 (^{55}Fe), a γ -source and strontium-90 (^{90}Sr), a β^- -source. Both sources can be used to determine the energy response of an HV-MAPS.

Iron-55

The dominant decay process of the iron-55 (^{55}Fe) isotope is electron capture with a half-life of $\tau_{1/2} = 2.7$ years. Electron capture is a weak interaction, where an electron of closely bound state interacts with a proton from the nucleon. The electron and proton convert into a neutron and an electron neutrino ($e^- + p \rightarrow \nu_e + n$). In case of ^{55}Fe , the resulting isotope produced by electron capture is manganese-55 (^{55}Mn). An electron in a higher state occupies the now empty state of the captured electron. During its transition into the lower state, an Auger electron or a photon is emitted. The emittance of an Auger electron is the most dominant process. However, due to its low energy of $E = 5.2$ keV, the Auger electron does not leave the source and therefore can not be detected. The second most dominant process is photon emission. The most probable photon emissions are the $K_{\alpha 1}$ and $K_{\alpha 2}$ lines. Because of their small energy difference, these two different lines can be treated as one monochromatic line with $E_{\gamma} = 5.9$ keV, which makes ^{55}Fe suitable for energy calibration measurements. At production in 2008 the iron-55 source, which is used for the measurements presented in this thesis, had an activity of 740 MBq and an emission rate of 15 MHz/steradian, which is lower than the activity, since the

Auger electrons and several photons are absorbed in the source. This results in an estimated emission rate of 250 kHz/steradian during the measurements performed here.

Strontium-90

Strontium-90 (^{90}Sr) decays via a β^- decay ($n \rightarrow p + e^- + \bar{\nu}_e$) into yttrium-90 (^{90}Y) with a half-life of $\tau_{1/2} = 28.8$ years. During this decay an electron with a maximum energy of $E_{\text{max}} = 0.55$ MeV is emitted. Since yttrium-90 is not a stable isotope, it decays via a β^- decay into zirconium-90 (^{90}Zr), which is stable. The electron emitted in this process has a maximum energy of $E_{\text{max}} = 2.3$ MeV and this process has a half-life of $\tau_{1/2} = 64$ hours. Thus, the observable electron spectrum is continuous and ranges up to a maximum energy of 2.3 MeV. Since electrons with an energy of 1 – 2 MeV lose a similar amount of energy in silicon as a MIP, electrons from a strontium-90 source can be used to mimic a MIP-like energy deposition. [22] The strontium source used in this thesis had an activity of 3.7 MBq at production in 1985. It is estimated that the strontium-90 source has an activity of 1.5 MBq during the measurements performed in this thesis.

6.2.3 X-Ray Tube

An X-ray tube can be used for high particle rate measurements. X-Ray is created by an electron beam hitting an anode material. The electrons emit bremsstrahlung photons or create photons by scattering with the anode material. These photons created by scattering are the so-called characteristic X-ray lines, whose energy depends on the anode material. Thus, an X-ray tube creates a beam of photons with an energy distribution consisting of a continuous bremsstrahlung spectrum and discrete energy peaks created by the characteristic lines. The intensity of this photon beam is linearly dependent on the electron flux incident on the anode material, such that the photon rate of the tube can be controlled via the applied electron current. The end-point energy of the bremsstrahlung spectrum depends on the acceleration voltage of the electron beam. In this thesis a PHYWE XR 4.0 [37] X-ray tube with tungsten, copper and molybdenum anodes and an acceleration voltage of $V = 35$ kV is used. The electron anode current can be regulated between 0.01 and 1.0 mA in steps of 0.01 mA.

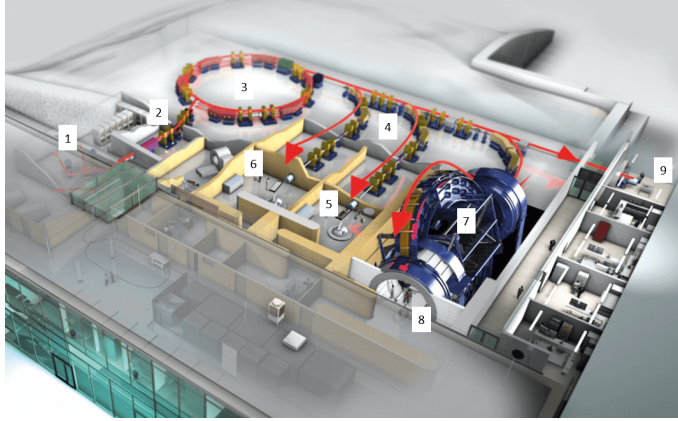


Figure 6.2: Graphic of the HIT accelerator complex. 1: Ion injection. 2: Linear accelerator. 3: Synchrotron. 4: Beam Lines. 5, 6, 8: Patient treatment. 7: Gantry. 9: Testbeam location.[39]

6.2.4 Heidelberg Ion Therapy Center

The Heidelberg Ion Therapy Center (HIT) [38] is a medical facility treating cancer patients. An ion beam is accelerated using a synchrotron, which accelerates protons and helium ions to about 220 MeV/u and heavier ions like oxygen and carbon up to about 430 MeV/u. For treatment intensities are typically between $10^6 - 10^9 \text{ s}^{-1}$ [38]. The accelerator complex is shown in Figure 6.2. The testbeam location marked with 9 is used for the measurements presented in this thesis. Ion beams can be used to study the effect of large energy deposition in the sensor diode. Additionally, high intensity ion beams are suitable to measure single event upsets in an HV-MAPS sensor. Single event upsets are bit flips caused by ionization in the configuration modules and registers of the sensor, leading to errors in the configuration of the sensor.

6.3 Sensor Configuration

Since the MightyPix will be an untriggered sensor, the AP3.1 is used in untriggered readout mode within this thesis. The sensor under test is operated with different clocking configurations, which change for example the readout speed and the timestamp precision. Table 6.1 shows the different clocking configurations of the AP3.1 used in this thesis. As explained in Section 5.3, the state machine of ATLASPix3 sensors can not be operated above 40 MHz. The data corruption observed at a state machine speed of 60 MHz is shown in appendix B.1. Therefore, the state machine of the 1.2 Gbit/s readout is slow downed by a factor of 2 with the setting *timerend* = 1, while the 400 Mbit/s and 800 Mbit/s configuration use the setting *timerend* = 0. Unless otherwise specified, the 1.2Gbit/s configuration of the sensor is used for the measurements presented in this thesis. The values of the parameter of the sensor

Readout Mode	External Clock	Readout Speed	Command	State Machine	Timestamp
Untriggered	200 MHz	400 MBit/s	40 MHz	20 MHz	40 MHz
Untriggered	400 MHz	800 MBit/s	80 MHz	40 MHz	80 MHz
Untriggered	600 MHz	1.2 GBit/s	120 MHz	30 MHz*	120 MHz

Table 6.1: Settings used in measurements presented in this thesis. *timerend = 1

configuration and the voltages supplied to the sensor can be found in appendix A.

The substrate of the sensor under test is not thinned to 100 μm , which will be the thickness of the MightyPix sensors, which will be operated at LHCb. As a consequence, more than 600 μm of undepleted silicon is beneath the depletion zone of the sensor under test. It is therefore possible that ionization in the undepleted region contributes to the signal.

7 Calibration Measurements

In this chapter, measurements to calibrate the sensor response are presented, since within the scope of this thesis the GECCO system is commissioned in Heidelberg. Therefore, the basic characteristics of the sensor like the diode breakdown and the threshold are measured to confirm the functioning of sensor and DAQ system. Moreover, the threshold tuning algorithm of the GECCO DAQ system is tested. Threshold tuning on pixel basis is important for large scale detectors like the MightyTracker to achieve a high hit efficiency with a low noise rate, which is necessary for a high tracking performance of the detector. Lastly, the energy deposition response of the sensor is determined using radioactive particle sources.

7.1 Global Sensor Calibrations

In the following the characteristics of the global parameters of the sensor, like the on-sensor generated voltages and the breakdown of the sensor diode, are determined. The calibration of the on-sensor generated voltages can be used to determine the threshold applied to a signal, while the sensor diode characteristics can be used as a measure of functionality. Firstly, the IV-characteristic of the sensor diode is determined. Secondly, the tuneable voltages parameters Bl , Th and Inj are calibrated to the voltage generated on-sensor.

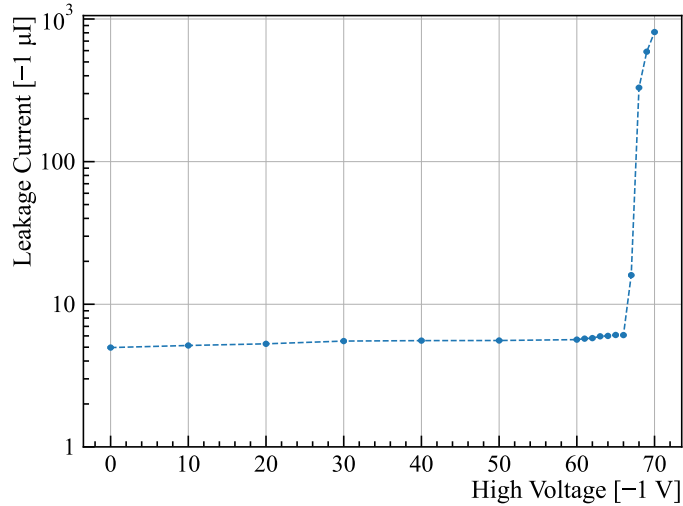


Figure 7.1: Leakage current against depletion voltage

IV - Scan

An IV-scan measures the leakage current against the bias voltage of the sensor diode. This measurement can be used as a quick check if the diode of the sensor is working correctly. Additionally, the IV-curve can be used as a measure of irradiation effects, which change the effective charge carrier density of the sensor.

As a first measurement, the breakdown¹ of the sensor diode is measured. For that, an IV-curve between 0 and -60 V with a step size of 10 V and between -60 and -70 V with a step size of 1 V is measured (Figure 7.1). The breakdown is determined to be at $V_{\text{Bias}} = -67 \pm 1$ V. The leakage current in the plateau region of the IV-curve is in the order of $\mathcal{O}(1 \mu\text{A})$. This leakage current is not measured directly on the sensor but with the power supply. Therefore, the measured current includes currents created by safety components in the DAQ system. Both breakdown voltage and leakage current are compatible with measurements performed in [32].

¹The breakdown described here is likely caused by a local effect in the pixel structure. The breakdown of the diode of the ATLASPix3 is currently under investigation.

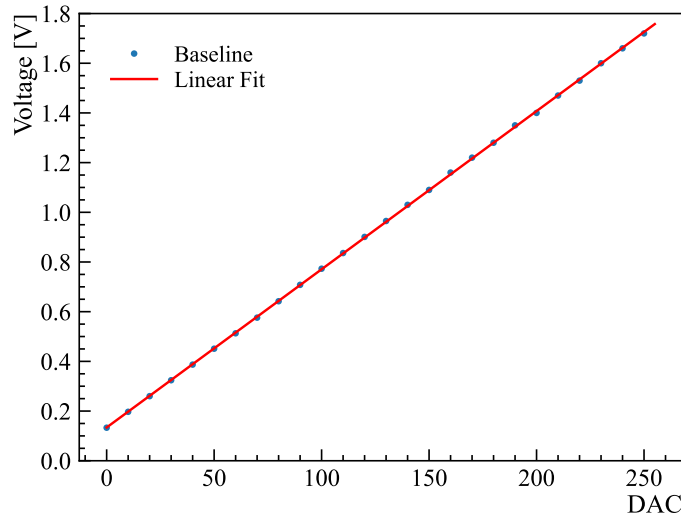


Figure 7.2: Calibration measurement of *Bl* VDAC: Applied voltage against DAC counts.

Baseline Voltage Calibration

The baseline voltage V_{BI} of the comparator, where the amplifier signal is coupled to, can be tuned between 0 – 1.8 V in 256 steps using the VDAC *Bl*. The baseline voltage has to be determined to know the low level of the comparator input. A measurement is performed to determine the baseline voltage against the VDAC values. The measured voltage is linearly dependent on the VDAC value (Figure 7.2) as it is designed. The measured data is fitted with a linear function to determine a calibration function. The fit yields a slope of ≈ 6.4 mV/DAC count, which deviates slightly from the theoretical value of 7 mV/DAC count. The theoretical value is determined by a linear spacing between 0 and 1.8 V in 256 steps. It is only possible to measure the globally applied baseline voltage and not the actual in pixel baseline, which may vary between pixels.

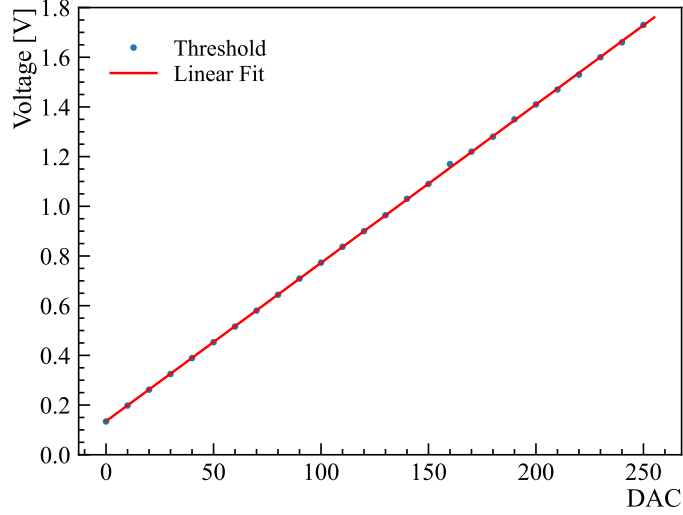


Figure 7.3: Calibration measurement of Th VDAC: Applied voltage against DAC counts.

Threshold Voltage Calibration

Similarly to the baseline, the threshold voltage V_{Th}^{set} used for the comparator can be tuned between 0–1.8 V in 256 steps using the VDAC Th . Again, a linear calibration curve with a slope of ≈ 6.4 mV/DAC count is determined (Figure 7.3), which agrees with the baseline VDAC. With the baseline and threshold calibrated to a voltage value, the global threshold V_{Th}^{global} applied to a signal is calculated:

$$V_{Th}^{global} = V_{Th}^{set} - V_{Bl} \quad (7.1)$$

In the following measurements a baseline of 140 DAC counts (1.03 V) and thresholds between 155–170 DAC counts corresponding to a voltage of 1.12–1.22 V are used, which results in thresholds applied to the comparator between 100–200 mV.

Since the amplitude of the amplifier and the threshold and baseline of the comparator of different pixels may vary, the threshold can be tuned with a so-called tune DAC (TDAC) on pixel basis. Hence, the pixel threshold V_{Th}^{Pix} is given as:

$$V_{Th}^{Pix} = V_{Th}^{set} - V_{Bl} + V_{TDAC}^{Pix} \quad (7.2)$$

The calibration between tune voltage V_{TDAC}^{Pix} and TDAC value is determined in [32], where a linear dependency between threshold height and TDAC value is observed.

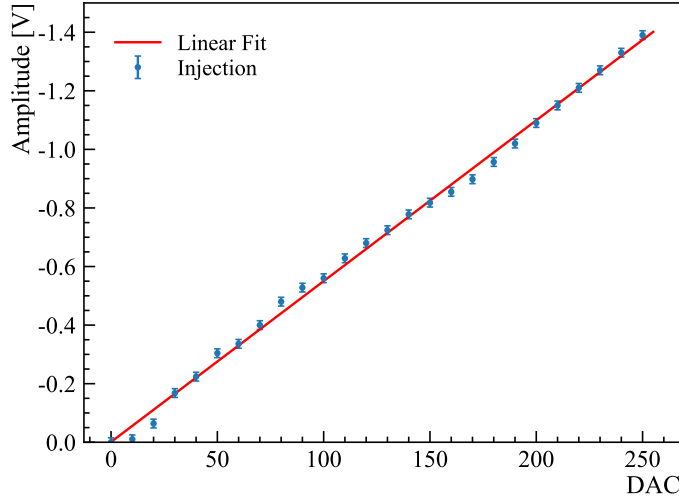


Figure 7.4: Calibration measurement of Inj VDAC: Applied voltage against DAC counts.

Injection Pulse Calibration

The in-pixel electronics of every pixel can be tested with a so-called injection pulse, which injects a charge signal into the pixel readout structure. The amplitude of the injected pulse can be set using the VDAC Inj . The calibration between voltage amplitude and DAC counts can be found in Figure 7.4, where the amplitude is given as the voltage difference between high level (charged capacitor) and low level (discharged capacitor). The slope of the fit yields a calibration factor of ≈ -5.5 mV/DAC count.

7.2 Injection Pulses: Local Threshold Calibrations

Since the threshold applied to the amplifier pulse varies between pixels, the on-sensor created threshold has to be calibrated locally on pixel level. Injection pulses, which do not vary significantly in amplitude between pixels, are used to measure the in-pixel threshold of the comparator with so-called S-Curves. A threshold calibration at pixel level is required, since sensors operated in a tracking detector need a per-pixel calibrated threshold to achieve a consistent hit efficiency for all pixels of the detector.

Injection pulses are on-chip generated test pulses created by discharging the injection capacitor. In the ATLASPix3.1, it is observed that large injection signals create crosstalk² between injection lines of the same column. As a result, a small fraction of the signal which is injected into one pixel of a column is injected into the other pixels of the column.

²Crosstalk is the effect of a signal inducing a signal on a neighboring line. More information on crosstalk between injection lines can be found in [32].

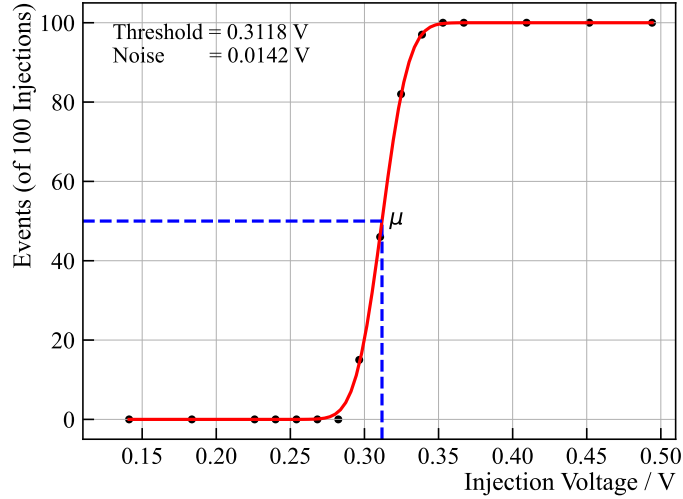


Figure 7.5: Example of a measured S-Curve with an error-function fit. μ indicates the 50% value and the threshold.

7.2.1 S-Curves

S-Curve measurements are used to determine the actual in-pixel threshold. An S-Curve describes the number of hits passing the threshold as a function of the injection amplitude. Since the threshold is a binary decision one would expect a step function between 0 and 100 % of the injected pulses detected. However, due to electronic noise in the amplifier and comparator circuit, the step function is smeared out. If one assumes a Gaussian error noise source, this smeared out step function can be described with the Gaussian error function *erf*, the S-Curve (Figure 7.5):

$$N(V_{\text{inj}}) = \frac{N_{\text{inj}}}{2} \left(1 + \text{erf} \left(\frac{V_{\text{inj}} - \mu}{\sqrt{2}\sigma} \right) \right) \quad (7.3)$$

where $N(V_{\text{inj}})$ is the number of detected injection pulses for an injection amplitude V_{inj} , N_{inj} the number of injected pulses, μ the 50% value corresponding to the threshold and σ the Gaussian noise. With a fit to the data of a single pixel, its threshold and its electronic noise can be determined. An example of such a fit is given in Figure 7.5. 100 pulses are injected into the amplifier of a pixel for different injection voltages between 0.14 – 0.5 V. For each voltage step, the number of hits passing the threshold is recorded. The number of detected pulses per injection amplitude is fitted with an S-Curve. The error-function fit describes the data well and yields in this example a threshold of 310 mV and an electronic noise of 14 mV.

This measurement and fit can be performed for every pixel to determine the pixel threshold distribution of the sensor. The threshold distribution of an AP3.1 sensor with an externally applied threshold of $V_{\text{th}}^{\text{set}} = 160$ DAC counts and a constant threshold tuning for all pixels of TDAC = 4 is shown in Figure 7.6 in blue. The mean of pixel threshold distribution at this threshold setting is about 138 mV, which

corresponds to a signal of 1290 electrons³ in the pixel diode. However, the standard deviation of the threshold distribution is broad with 15 mV (150 e). The mean of the noise distribution is 9 mV (95 e) with a standard deviation of 3 mV (30 e) (Figure 7.7). The threshold and noise distribution of the sensor under test shows no dependency on the position of the pixel.

A wide threshold distribution reduces the time of the sensor. Additionally, the pixel thresholds of a sensor have to be calibrated to achieve a narrow threshold distribution and a high detection efficiency. The threshold distribution can be calibrated to a target threshold and the width of the distribution can be decreased using the threshold tuning TDAC's. The process of threshold tuning is called TDAC trimming.

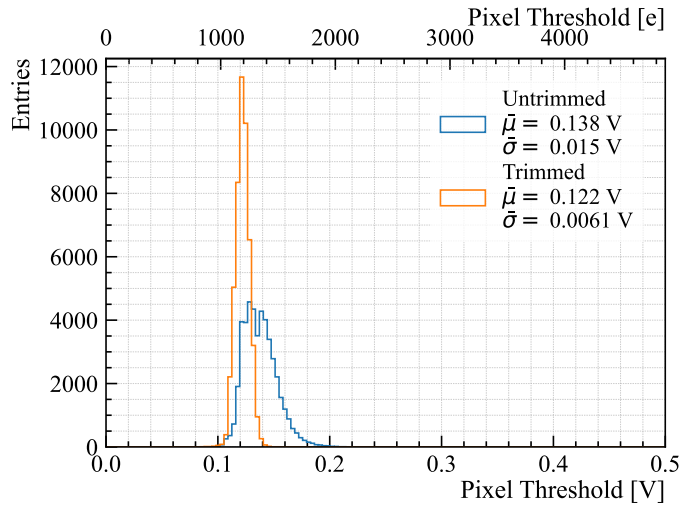


Figure 7.6: Histogram of all pixel thresholds determined with S-Curve measurement. The blue histogram shows the measured threshold with an untrimmed sensor and the orange the resulting threshold distribution after trimming.

³A calibration measurement between threshold and signal height in electrons is performed in Section 7.3.2

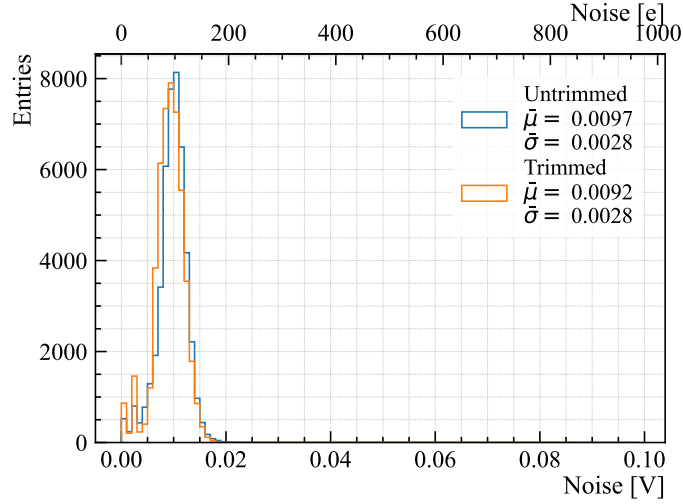


Figure 7.7: Histogram of the electronic noise determined with S-Curve measurements. Blue shows the noise for an untrimmed sensor and orange for a trimmed sensor.

7.2.2 Threshold Trimming

A threshold (TDAC) trimming can be used to fine-tune the global threshold on pixel basis in 8 steps (0 – 7) by the tune DACs (TDAC). An algorithm for tuning the TDAC values of every pixel is already implemented in the GECCO DAQ system. For this algorithm a so-called target threshold has to be specified. The target threshold voltage does not necessarily have to be the chosen external threshold voltage $V_{\text{Th}}^{\text{set}}$. However, the target threshold should be chosen such that the resulting trimmed TDAC values have an average of 3.5 over the entire sensor, since this allows to use the maximum trimming range to higher and lower pixel thresholds.

The trimming algorithm determines the TDAC value of a pixel, which matches the target threshold, in a binary search. For that, 3 to 4 S-Curve measurements at different TDAC values are performed for every pixel. The decision tree at which TDAC values S-Curve measurements are performed is shown in Figure 7.8. The first S-Curve measurement is performed at TDAC = 3. The resulting pixel threshold is compared to the target threshold. If the pixel threshold is larger than the target threshold the second S-Curve is measured at TDAC = 1, if it is smaller than the target the second S-Curve measurement is performed at TDAC = 5. As before, the pixel threshold at this TDAC value is compared to the target threshold. If the threshold is smaller than the target threshold the TDAC value is increased by 1, if its larger the TDAC value is reduced by 1 and an S-Curve measurement to determine the threshold is performed at the changed TDAC value. If the last TDAC value measured is 6 and the measured threshold is larger than the target, a fourth S-Curve measurement at TDAC = 7 is performed to determine the threshold at this value. After the 3 or 4 S-Curve measurements the threshold determined by the S-Curves is compared with the target threshold. The TDAC value at which the

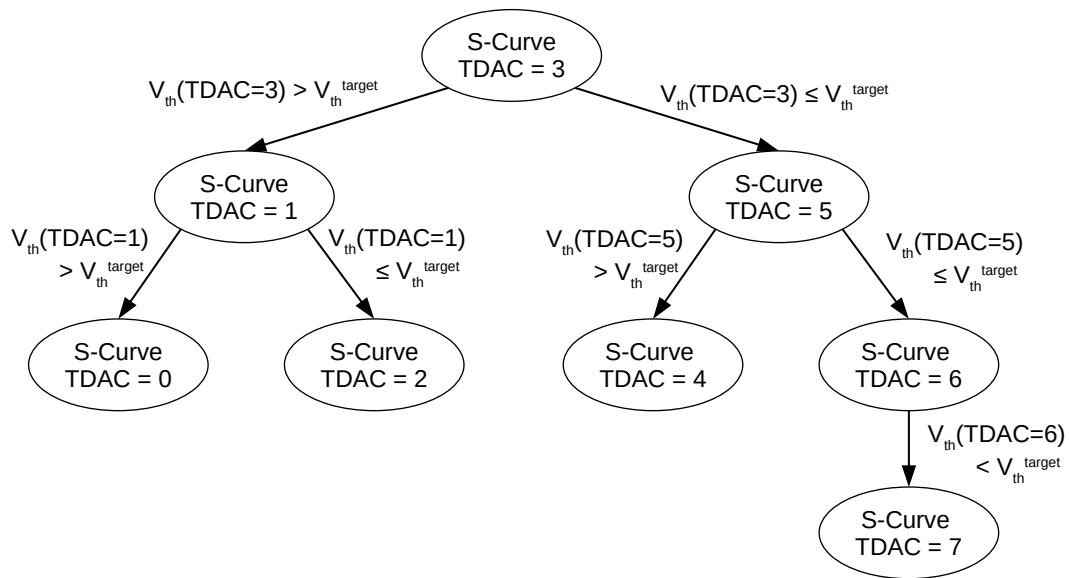


Figure 7.8: Scheme of the S-Curve measurements in the threshold trimming process. V_{th}^{target} indicates the target threshold, while $V_{th}(TDAC)$ indicates the measured threshold of the pixel.

corresponding pixel threshold deviates the least from the target threshold is selected as the tuned TDAC value of the pixel. Due to the multiple S-Curve measurements this trimming process can take several hours. A more detailed description of the trimming process can be found in [32].

The sensor tested in this thesis is trimmed to a pixel threshold of 120 mV at an external threshold of 160 DAC counts. After the threshold trimming, an S-Curve measurement is performed to validate the resulting threshold distribution (orange in Figure 7.6). The mean of the resulting threshold distribution is 122 mV (1190 e), which corresponds to the target threshold within the measurement accuracy. The standard deviation of the threshold distribution is 6 mV (60 e). This value is more than two times smaller than the standard deviation of the threshold of the untrimmed sensor (15 mV), which shows that the trimming is successful. As expected, the trimming does not affect the electronic noise (Figure 7.7), since the noise is independent of the threshold height.

In addition, to the threshold trimming, a noise trimming is performed to reduce the number of pixel measuring noise hits on the targeted threshold. Noise hits are fluctuations of the noise which pass the threshold of the comparator. For the noise trimming, the noise hits of the sensor are measured for a chosen period of time. All pixels measuring hits exceeding a specified number are assigned a higher TDAC to suppress noise hits. This process is repeated until an acceptable noise rate is seen. If a pixel with a TDAC value of 7 still measures noise, it is deactivated by setting the mask bit. However, for an unirradiated sensor with a threshold of 122 mV only minimal noise trimming needs to be performed and no pixels need to be masked to achieve a noise rate close to 0 Hz/pixel. Although it is not done here, further noise trimming can allow the operation of the sensor at lower thresholds, which may improve the time resolution of the sensor. [40]

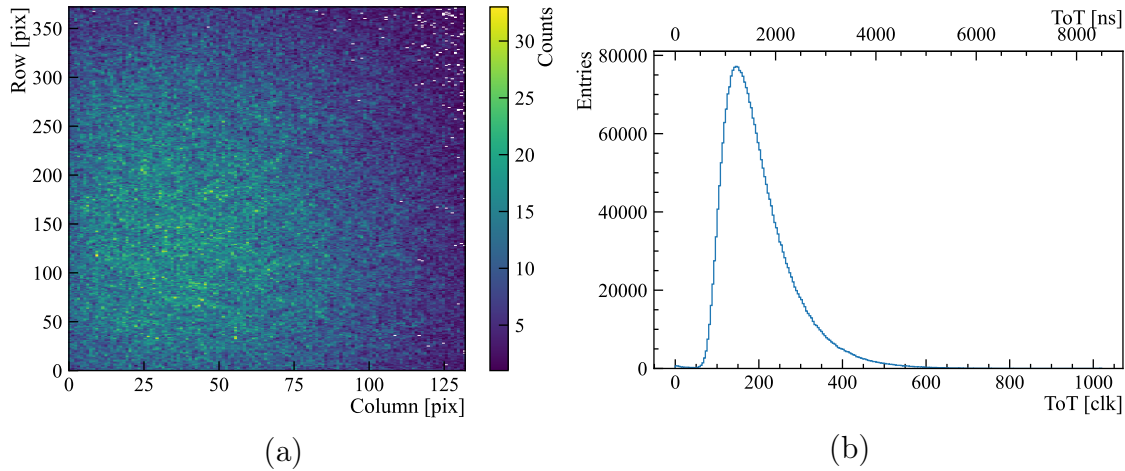


Figure 7.9: a) Measured hit map of a ^{90}Sr source 2 cm in front of the sensor.
 b) ToT spectrum of ^{90}Sr measured with AP3.1.

7.3 Radioactive Particle Source: Energy Response

With injection pulses only the amplifier and comparator circuits of the pixels are tested. A radioactive particle source can test the characteristics of the charge deposition in the pixel diode together with the readout of the sensor. For this, a strontium-90 β -source and an iron-55 γ -source are used. In addition to the abilities as a general test of the sensors diodes, electrons from ^{90}Sr can be used to mimic the energy deposition of a MIP, since 1 - 2 MeV electrons deposit a similar energy as MIP in silicon [22]. On the other hand, the monochromatic photons from ^{55}Fe are suitable for energy calibration measurements of the pixel response.

7.3.1 Strontium-90

The measurement with a ^{90}Sr source shows that all pixel diodes of the sensor under test are responding and are working correctly. The hitmap of this measurement can be seen in Figure 7.9a. A clear but diffuse irradiation spot is visible in the lower left quadrant due to the distance between source and sensor. In the source profile no obvious electronic effects are seen. The interaction between the electrons and the sensor material lead to the formation of clusters of hits. The distribution of the size of these clusters is shown in Figure 7.10. Since electrons of a strontium-90 source have a MIP-like energy deposition in silicon, one expects little charge sharing between pixels and a mean cluster size of 1 pixel. However, in the measurement a mean cluster⁴ size of 1.95 pixel and a standard deviation of 1.5 is measured. The difference between the expected and the actual size can be explained by inclined tracks

⁴A cluster is defined here as hits, which have a distance of 5 pixels to the cluster and occur in a 2 μs time window after the first hit of the cluster. More information on the clustering algorithm can be found in Section 9.2.

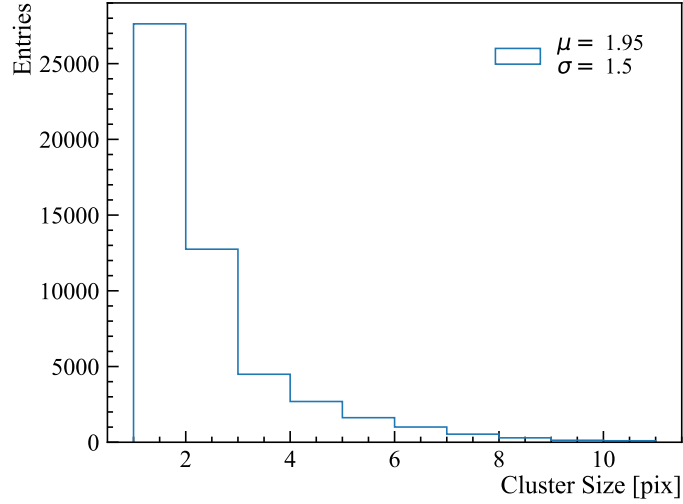


Figure 7.10: The size of hit cluster in pixel measured with a strontium-90 source.

of the electrons through the sensor, causing the electrons to traverse several pixels where they deposit energy. This is visible in the spatial structure of large clusters. These clusters do not extend equally in column and row direction, which would be expected for charge sharing, but are observed to have a bias in one direction.

The time-over-threshold spectrum of the measurement shows the energy deposition of the ^{90}Sr electrons, although the ToT spectrum is not linearly dependent on the energy deposition. The ToT spectrum (Figure 7.9b) peaks at $1.2 \mu\text{s}$ (180 clks) and has a long tail structure up to $5 \mu\text{s}$ (600 clks). One would expect that this spectrum is described by a Landau distributed energy deposition. However, the spectrum is deformed by the non-linearity of the ToT measurement. The pulse height and time-over-threshold of a pixel is logarithmically dependent on the energy deposition as found in [32]. Additionally, the ToT spectrum varies between pixels. This variation is mainly created by a variation of the feedback currents in the amplifier circuit between different pixels. [32] This feedback current of the AP3 is of the order of 60 pA nominally. However, such a small current is sensitive to production variance, hence the current varies between pixels. The rise time of the amplifier and thus the time-over-threshold is logarithmic dependent on the feedback current. [32] Therefore, the time-over-threshold distribution of the sensor is given by a log-normal distribution. As a result the observed ToT spectrum of the ^{90}Sr β -particles is a Landau distribution of the ionization loss folded with the log-normal distribution of the sensor response.

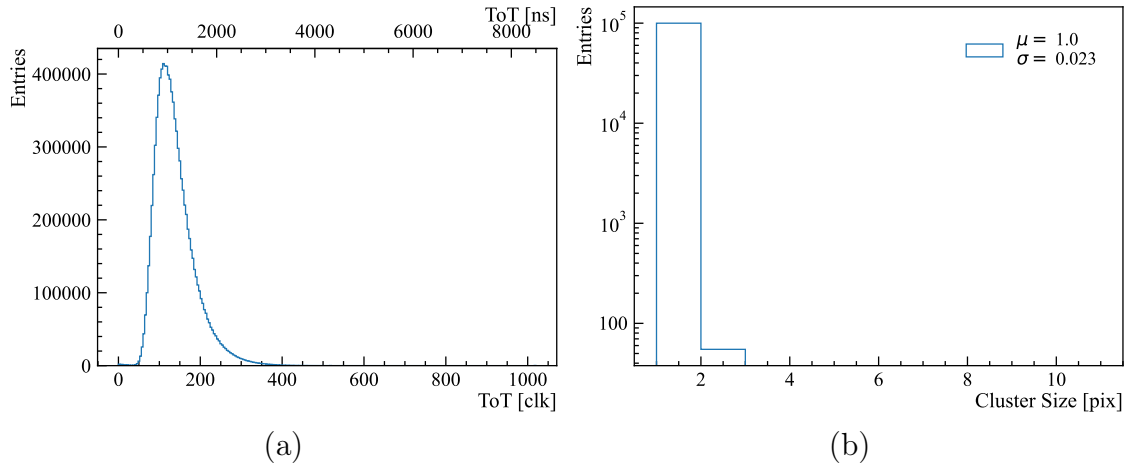


Figure 7.11: a) Measured time-over-threshold spectrum of iron-55. b) Measured cluster size distribution of iron-55 photons.

7.3.2 Iron-55

In contrast to the ^{90}Sr source, which produces a continuous energy spectrum, iron-55 produces monochromatic photons with an energy of about 5.9 keV. Additionally, photons detected by the sensor are absorbed in one pixel, which reduces the charge sharing between pixels almost completely. This effect can be seen in the cluster size distribution measured with a ^{55}Fe source in Figure 7.11b. The largest cluster observed consists of 2 pixels and the mean cluster size is 1.00 pixel with a standard deviation of 0.02. Therefore, the iron source can be used for an energy calibration of the sensor under test.

The time-over-threshold spectrum of the iron-55 source is shown in Figure 7.11a. Because of the lower energy deposition the ToT spectrum of the ^{55}Fe photons peaks at 1 μs (150 clks). The spectrum still shows the tail structure produced by the ToT variation between pixels. However the tail contribution is reduced in respect to ^{90}Sr with a maximum ToT of 3 μs (400 clks), since the observed energy deposition of the photons follows a Gaussian distribution instead of a Landau distribution. Because of the non-linear dependence between ToT and energy deposition, the iron-55 line alone is not sufficient for energy calibration of the time-over-threshold response. However, ^{55}Fe can be used to calibrate the amplitude of injection pulses to an energy deposition.

The ToT spectrum of the iron-55 source peaks at about 1 μs , which corresponds to an injection pulse amplitude of 30 DAC counts. Therefore, the injection amplitude of 165 mV (30 DAC) corresponds to an energy deposit of 5.9 keV or 1620 electron charges collected by the pixel diode. The calibration measurement in Section 7.1.1 is used to calculate the corresponding energy deposition of an injection amplitude. With the injection strength known in terms of energies and electron-hole pairs, the pixel threshold measured by S-Curves can be expressed in terms of energy or number

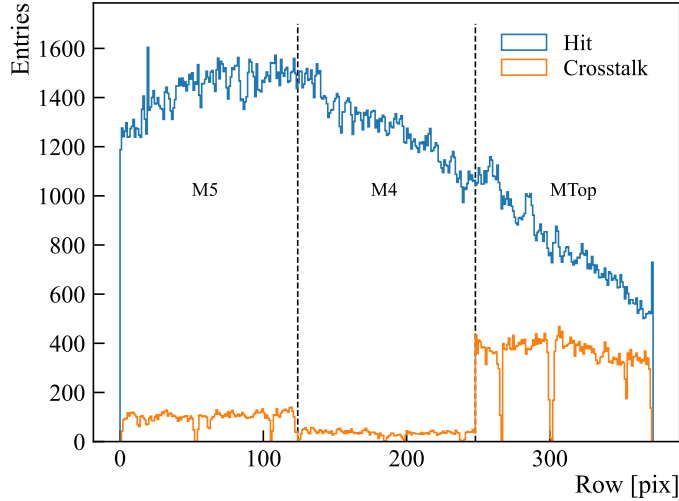


Figure 7.12: Row distribution of physical hits (blue) and crosstalk hits (orange) measured with a ^{90}Sr source. The dashed lines indicate the metal layers of the signal lines.

of electrons. The threshold measured in Section 7.2.2 and used in this measurement ($V_{\text{th}} = 122$ mV) corresponds to about 1200 electrons detected or an energy deposition of 4.3 keV in the sensor. As a reference, a MIP produces a signal of 10 ke in $100\ \mu\text{m}$ of silicon [22].

7.3.3 Crosstalk Hits

In measurements with strontium-90 and iron-55 sources and in later measurements at HIT (chapter 9) crosstalk hits are observed. Crosstalk is the effect of signals on the transmission lines between pixel and periphery spilling over from one line to another. Therefore, crosstalk hits are only observed in the same column as the crosstalk-inducing hit [41]. Crosstalk is a short pulse induced by the raising edge of a signal. Crosstalk hits are therefore short with a ToT of $0 - 5$ clks. The pulses can be shorter than the step size of the timestamps. As a result, the hit time can be digitized in the wrong timestamp bin, which results in a ToT calculation to the maximum ToT value of 1024 clks. Both possible ToT values make crosstalk hits easily distinguishable from physical hits in the sensor. Crosstalk hits occur with a row dependency matching the metal layers of the signal lines as shown in Figure 7.12. The lowest metal layer M4, which is the signal line for row $125 - 247$, shows the least crosstalk, while the top metal layer, which corresponds to row $248 - 371$, shows the most crosstalk. Additionally, twelve rows, four per metal layer, show less to no crosstalk. The signal lines of a column are arranged in two bunches, which are divided by the power lines to the pixel. Therefore, four lines per metal layer are placed at the edges of the signal line bunches. Hence, the corresponding pixels of these signal lines are less likely to observe crosstalk, since fewer lines which could

induce a signal are in the neighborhood.

Since crosstalk between the transmission lines leads to ghost hits in the sensor and deteriorates the tracking performance of a large scale detector like the Mighty-Tracker, crosstalk must be reduced. Two sensor parameters can be used to reduce crosstalk. The first parameter is the line driver voltage V_{Minus} , which can be generated on chip with the VDAC $minus$ or applied externally, which is done here. Increasing V_{Minus} reduces the pulse height on the signal line (see Equation 5.1 and 5.2) and so the induced current on neighboring lines. However, a smaller signal worsens the time resolution of the sensor [40][42]. Secondly, the input level of the receivers in the periphery $VNBiasRec$ and $VPBiasRec$ can be increased to reduce crosstalk. Increasing the input level of the receiver reduces time resolution of the sensor, however the influence on the time resolution is lower than that of V_{Minus} [40][42]. With a V_{Minus} of 0.58 V and a receiver of $VNBiasRec = 30$ and $VPBiasRec = 30$ it is possible to reduce crosstalk below a measurable level.

8 High Rate Measurements

The MightyPix sensors will be located close to the beam pipe and will be operated at mean particle rate of 50 MHz per sensor¹. At this particle rate, the challenge for the detector is to read all hit information from the pixels and send it to the DAQ with a minimum latency allowing an online event building at a rate of 40 MHz. The high rate behavior of the ATLASPix3.1 sensor is therefore studied in the following. An X-ray tube can provide high rates of photons, which can be used to study the behavior of the sensor at LHC-like particle rates. As described in Section 6.2.3, the photon rate of an X-ray tube is linearly dependent on the anode current. Hence, the X-ray tube provides a photon rate tuneable within its range of anode currents of $I = 0.01 - 1.0$ mA. It is measured that the mean hit cluster size of X-ray photons with a maximum energy of 35 keV is 1.03 with a standard deviation of 0.28 as shown in Figure 8.1a. The clustering algorithm applied to the data is described in Section 9.2. Since the cluster size is about 1, the photon rate provided by the X-ray tube is approximately equal to the hit rate on the sensor. To confirm this hypothesis, the hit rate on the sensors is measured in dependency of the anode current of the X-ray tube. The measured hit rate is indeed linearly dependent on the anode current and a linear fit agrees well with the measured data as seen in Figure 8.1b. Therefore, the anode current of the X-ray tube can be used as a measure of photon and hit rate on the sensor. The rate measurement shown here is further discussed in Section 8.2. The X-ray tube is used to study the rate dependent delay in the readout and the hit rate capability of the sensor under test.

In the following measurements, the untriggered readout mode is used in different clocking configurations, which are shown in Table 6.1. The main difference between the different clocking configurations is the external clock applied to the sensor. As a result, the state machine speed and the timestamp precision differ between the configurations. Since the data stream from the FPGA is too large for the USB 2.0 standard, the Ethernet / UDP readout of the GECCO system is used for all measurements presented in this chapter. The two different measurement setups used in this chapter are depicted in Figure 8.2. The readout delay measurement is taken as the first proof of principle measurement that the AP3.1 and the GECCO system can be stably operated in an X-ray tube. The sensor uses the 400 Mbit/s readout speed in this measurement, which is not optimized for a delay measurement. The measurement should be therefore re-done with a faster clocking configuration.

¹See Section 3.3.2

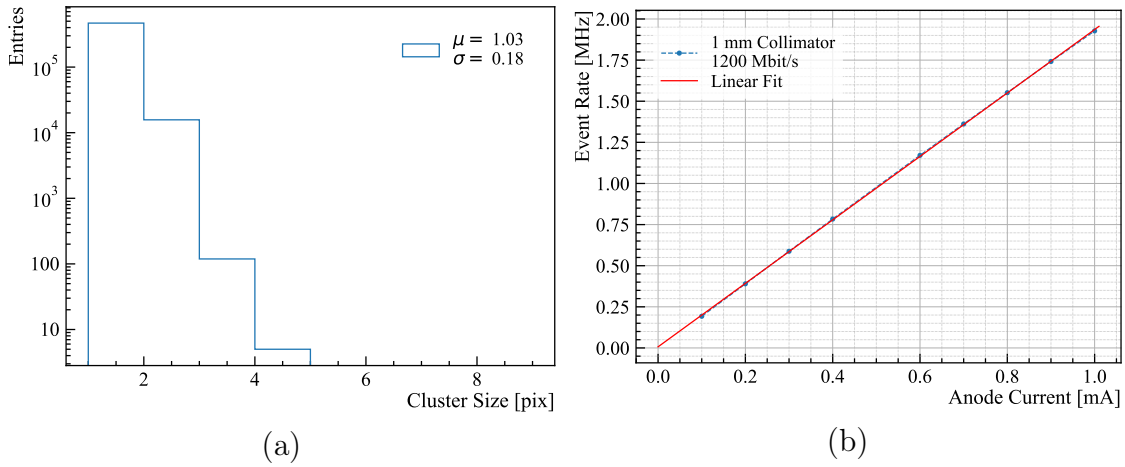


Figure 8.1: a) Measured cluster size distribution of tungsten X-ray. b) Hit rate on the sensor measured against the anode current of the X-ray tube using a 1 mm collimator.

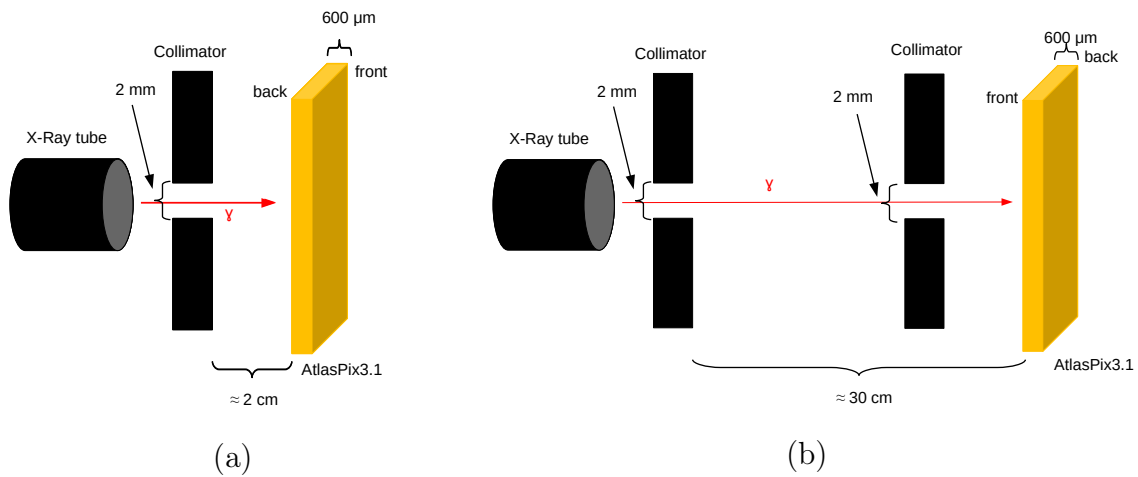


Figure 8.2: Scheme of the two setups used for X-ray measurements. a) shows a backside and b) a frontside irradiation.

8.1 Readout Delay

Although the delay between the particle hit and the time-of-arrival timestamp TS1 is in the range of $\Delta t_{\text{hit}} = \mathcal{O}(\text{ns})$ in the ATLASPix3(.1) sensors [32][40], the processing of the hit information can be delayed by $\mathcal{O}(\mu\text{s})$. The readout structure of the ATLASPix3(.1) allows for multiple kinds of delay effects in the processing of a hit, which are shown in Figure 8.3. The first delay Δt_{ToT} in the readout of a hit is caused by the digitization of the hit in the periphery. A hit is only processed in the peripheral readout once both of its timestamps, the leading (the hit timestamp) and trailing edge timestamp, are recorded. Therefore, the readout of a hit is delayed by its time-over-threshold:

$$\Delta t_{\text{ToT}} = \text{ToT} \quad (8.1)$$

Moreover, the readout of a hit can be delayed by the column drain structure and the finite state machine (FSM) of the readout. Since only one pixel per column can be read out in a single readout cycle, hits have to be stored in the hit buffers until they are processed by the end-of-column structure. In addition to the waiting time in the hit buffers, a delay is caused by the process time of the FSM to collect the data from the hit buffers and send it to the DAQ system. The delay caused by the hit buffers and the state machine is referred to as Δt_{FSM} in the following. To confirm this expectation, a measurement of the readout delay is performed. Since it is not possible to measure the delay of the readout on the sensor itself, a timestamp t_{FPGA} , which marks the arrival of the hit data in the FPGA of the DAQ system, is implemented in the firmware of the GECCO system. This timestamp is in phase with the timestamp clock of the sensor. The readout delay Δt_{meas} is determined by the time difference between the time-of-arrival timestamp TS1 and the arrival of the hit data on the FPGA:

$$\Delta t_{\text{meas}} = t_{\text{FPGA}} - \text{TS1} \quad (8.2)$$

This definition of the readout delay measures the delay caused by the digitization of a hit and by the processing of a hit in the FSM. Additionally, the measured readout delay includes a processing time on the FPGA Δt_{FPGA} in the order of $\mathcal{O}(10 \text{ ns})$, which may vary between different DAQ systems:

$$\Delta t_{\text{meas}} = \Delta t_{\text{ToT}} + \Delta t_{\text{FSM}} + \Delta t_{\text{FPGA}} \quad (8.3)$$

Since the delay caused by the FPGA is two orders of magnitude smaller than the delay caused by the sensor, the delay of the FPGA Δt_{FPGA} is neglected in the following:

$$\Delta t_{\text{meas}} \approx \Delta t_{\text{ToT}} + \Delta t_{\text{FSM}} \quad (8.4)$$

The readout delay of the ATLASPix3.1 is measured as a function of the hit rates

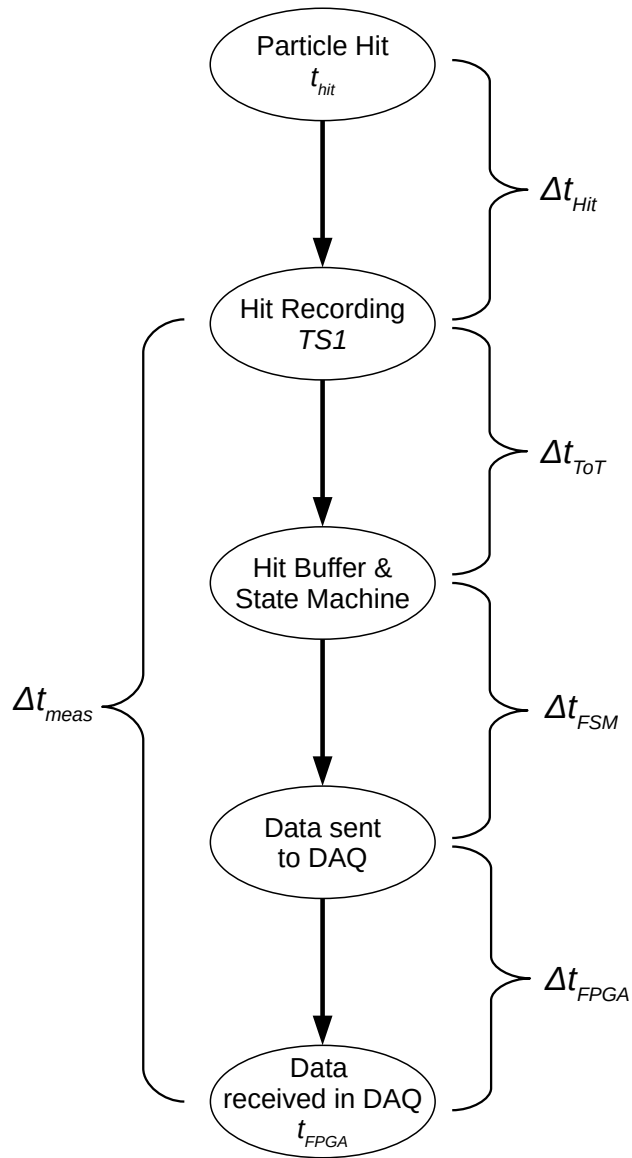


Figure 8.3: Scheme of the origin of delay in the readout structure of the ATLASPix3.1.

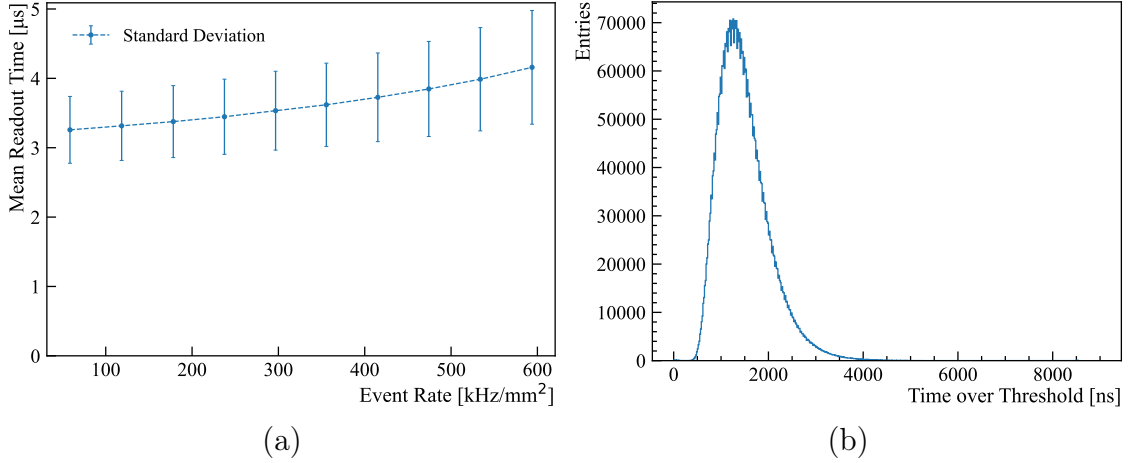


Figure 8.4: a) The mean delay in sensor readout measured with 200 MBit/s readout, the error bars give the standard deviation. b) The time-over-threshold spectrum of the tungsten X-ray anode used for the measurement in a).

provided by the X-ray tube. The sensor under test is placed behind two 2 mm collimators, as shown in Figure 8.2b. As a consequence of the small focus, only 40 rows (row 220 – 260) and 14 columns (column 24 – 39) are irradiated. The sensor uses the 400 MBit/s readout speed configuration with a timestamp width of 25 ns. The readout delay is measured for 10 different X-ray currents in steps of 0.1 mA over the entire current range of the tube. The resulting hit rate range detected by the sensor is between 0.22 – 2.3 MHz and in the beam spot between 59 – 594 kHz/mm². At the lowest photon rate a mean readout delay of $\Delta t_{\text{meas}} = 3.3 \mu\text{s}$ with a standard deviation of $0.7 \mu\text{s}$ is measured (Figure 8.4a). The delay caused by the digitization of a hit Δt_{ToT} can be determined from the time-over-threshold distribution of the measurement. Looking at the time-over-threshold spectrum of the measurement (Figure 8.4b) one can see that the mean time-over-threshold is about 1.5 μs . Therefore, a mean delay of 1.5 μs is created by waiting for the trailing-edge timestamp. As a consequence, a delay $\Delta t_{\text{FSM}} \approx 1.8 \mu\text{s}$ is caused by the FSM and hit buffers (Equation 8.4). Since the standard deviation of the measured time-over-threshold distribution is about 500 ns, the standard deviation of the readout delay distribution ($0.7 \mu\text{s}$) is mainly caused by the ToT distribution. The magnitude and distribution of the delay caused by the ToT can be decreased by shortening the pulse length of the signal. The time-over-threshold can be shortened by a faster fall time of the amplified pulse. This can be tuned with the feedback DAC parameter of the amplifier circuit.

The mean of the measured readout delay Δt_{meas} and the width of the distribution increase non-linearly with the photon rate. At the highest measured photon rate of 594 kHz/mm², the mean delay of the readout is $\Delta t_{\text{meas}} \approx 4 \mu\text{s}$ (see Figure 8.4a). An increasing delay with the hit rate is expected, since more events need to be processed by the readout structure. Since the delay caused by the digitization of a hit Δt_{ToT}

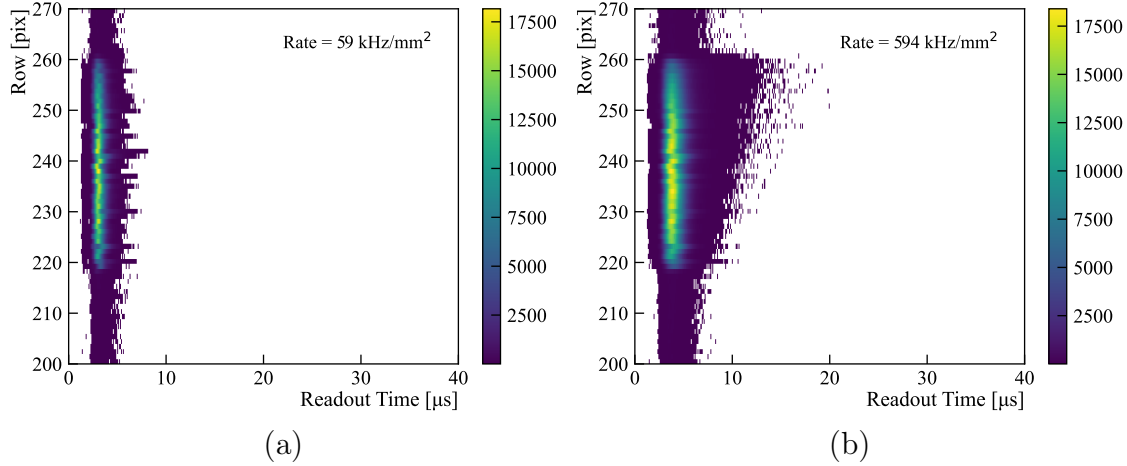


Figure 8.5: Histogram of delay in readout against row address for lowest (a) and highest (b) rate setting. The beam spot is between row 220 - 260.

depends on the ToT and is independent of the photon rate, the increased delay has to be caused by the FSM. Moreover, the standard deviation of delay distribution increases with the hit rate. The column drain structure of the readout can create a row dependent delay Δt_{FSM} caused by waiting times in the hit buffers, which would increase the magnitude and width of the delay distribution with the hit rate.

To verify this assumption, the row dependency of the readout delay is analyzed. Figure 8.5 shows the correlation between row address and readout delay Δt_{meas} of hits in the beam spot for the lowest and highest hit rate measured. For the lowest rate, no row dependency of the readout delay is observed. On the other hand, the measurement taken with the highest hit rate shows an increasing delay distribution with row address in a triangular shape. The readout delay in higher rows is larger and more widely distributed than in lower rows. This fits the expectation of an increased delay Δt_{FSM} caused by the column drain structure, since the readout structure is only able to read one hit with the lowest row address per column in a single readout cycle. Therefore, hits in lower rows are more likely to be read out without a waiting time in the hit buffers than hits with higher row addresses. Hence, the waiting time in the hit buffers increases with the row number, resulting in a larger delay. The delay Δt_{FSM} should be reduced by a faster state machine speed. This can be achieved by a faster external clock of 400 or 600 MHz for example. However, no readout delay measurements with these sensor configurations have been performed yet, such that this hypothesis is still under investigation.

To measure the readout delay and the row dependency of the delay in a MightyTracker-like setup, the whole sensor has to be irradiated uniformly, such that all pixels measure an equal hit rate. For this, the sensor is irradiated without a collimator from the backside close to the X-ray tube (Figure 8.2a). During this measurement, it is seen that the readout of the sensor works only up to a hit rate in the order of 2 – 4 MHz.

At higher rates the sensor measures noise pattern. Since this noise pattern occurs at the second lowest current setting of the X-ray tube, it is impossible to measure the hit rate dependency of the readout delay in a full-sensor irradiation. At the lowest rate setting, the hit rate detected by the sensor is 2.0 MHz (5.3 kHz/mm²), the mean readout delay is 4.1 μ s and the standard deviation is 1.7 μ s. At this hit rate, no significant row dependency of the readout delay is observed.

8.2 Rate Limitations

Triggered by the limitations seen in the readout delay measurement, a study about the rate limitations of the GECCO system and the ATLASPix3.1 is performed. For that, estimations on the theoretical limitations of the sensor and the GECCO DAQ system are made and the experimental rate limitations are measured. Moreover, rate measurements will be important for MightyPix prototypes, which will be operated at higher particle rates than other HV-MAPS, to be able to scan for hit rate induced effects. Rate measurements with the AP3.1 can be used as a proof of principle that lab X-ray tubes can be used to determine hit rate limitations.

8.2.1 Theoretical Limitations of the Setup

The rate limitations observed in Section 8.1 can be caused by the sensor itself or by the DAQ system. In this section the theoretical rate limitations of the DAQ system and the ATLASPix3.1 are determined.

Rate Limitation of ATLASPix3(.1)

The only possible limitation of the sensor is the finite state machine collecting the data from the hit buffers and sending them to the DAQ system. Rate limitations from dead/busy pixels can be excluded, since the hit rate per pixel is much smaller than the maximum readout delay observed in the previous measurement.

The FSM can process one hit per column in one readout cycle. (Section 5.2.1) Assuming one hit in every column, the theoretical rate limitation can be calculated from the duration of one readout cycle. Each readout cycle starts with nine preparation steps, which shift the hit information from the hit buffers to the end-of-column buffers. Four steps per available hit are required to read the hit information from the EoC and send it to the DAQ system. A detailed description of the state machine can be found in [32]. At maximum hit rate, a readout cycle takes $9 + 132 \times 4$ states. One readout cycle with a hit in every column takes about 18 μ s at a state machine frequency of 30 MHz. 132 hits processed in 18 μ s results in a rate limitation of about 7 MHz. Table 8.1 shows the theoretical rate limitation of different clocking configuration used in this thesis. These theoretical rate limitations are much lower than the expected particle rates at the MightyTracker, which was to be expected since the ATLASPix3 is designed for a triggered readout.

Readout Speed	External Clock	State Machine	Readout Cycle	Maximum Hit Rate
400 Mbit/s	200 MHz	20 MHz	26.9 μ s	4.9 MHz
800 Mbit/s	400 MHz	40 MHz	13.4 μ s	9.8 MHz
1.20 Gbit/s	600 MHz	30 MHz*	17.9 μ s	7.3 MHz

Table 8.1: Theoretical rate limitations of the AP3(.1) state machine. *timerend = 1

Rate Limitation of GECCO DAQ

The hit rate capability of the DAQ system is limited by the connection to the computer. In the GECCO system, 192 bit (3×64 bit) per hit are sent to the computer to be written to the hard drive. The connection to the computer can be established by using USB or UDP (Ethernet) protocols.

The rate limitation of the USB based readout can not be determined precisely, since it is used to send data to the computer and configuration to the sensor. However, the link speed is estimated to be in the order of Mbit/s [34], which corresponds to a rate limitation of approximately 10 kHz.

The rate limitation of the Ethernet based readout can be determined more easily, since it is only used to send the data output to the computer. The Ethernet connector on the FPGA is capable of a data rate of 1 Gbit/s, which results in a rate limitation of 5.2 MHz at a data size of 192 bit/hit sent to the computer. Since this value is smaller than the rate limitation of the sensor, it is assumed that the observed rate limitations in Section 8.1 are caused by the DAQ system. Therefore, the firmware of the DAQ system is adapted to reduce the number of bits per hit sent to the computer. By removing the trigger (time reference) information (64 bit) from the data flow, which is unused in the setup used for the X-ray measurements, the data per hit can be reduced to 128 bit/hit. However, this data size corresponds to a rate limitation of 7.8 MHz, which is still smaller than the rate limitation of the sensor. Therefore, the data per hit ratio needs to be reduced further. Since the firmware is built to send 64 bit data words to the computer, this structure remained unchanged. Therefore, a decision has to be made what information is stored into these 64 bit. In principle, all information of one hit sent from the sensor is stored in 34 bit (10 bit TS1, 7 bit TS2, 8 bit column, 9 bit row). However, both timestamps are extended to 40 bit timestamps in the DAQ system to achieve a time ordering of the data on FPGA level, because the latency between FPGA and computer is too large to achieve a time ordering at software level. Since the ToT information is not needed for measuring the rate limitation, the following data format was chosen: 7 bit identifier to identify the starting of a hit, 8 bit column, 9 bit row and 40 bit TS1. The identifier is needed in the decoding process of the binary data on the computer. With a data format of 64 bit/hit, the GECCO system is capable of a hit rate above 15 MHz. A summary of the maximum hit rate of different data formats is shown in Table 8.2.

Data Format	Data per Hit	Maximum Hit Rate
3×64 bit/hit	192	5.2 MHz
2×64 bit/hit	128	7.8 MHz
1×64 bit/hit	64	15.6 MHz

Table 8.2: Theoretical rate limitations of GECCO 1 Gbit/s Ethernet readout

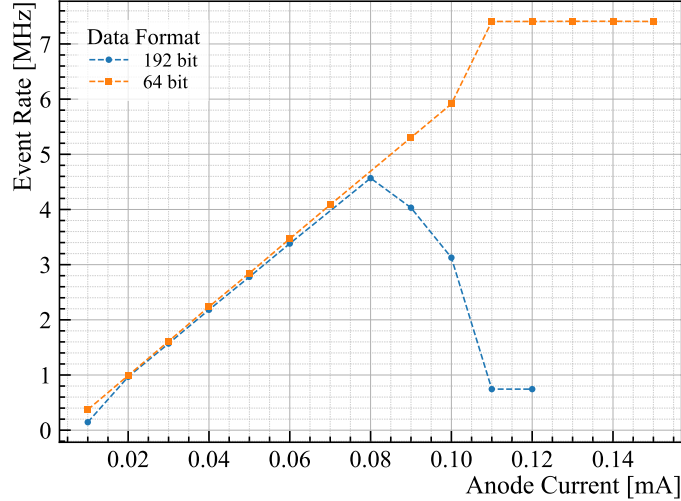


Figure 8.6: Measured hit rate with the 192 bit and 64 bit data format against the anode current of the X-ray tube.

8.2.2 Experimental Limitation

To verify the assumption made in the previous section, rate measurements with photons from the X-ray tube are performed. The sensor is irradiated from the backside as shown in Figure 8.2a. Firstly, the influence of the data size in the DAQ system on the rate limitation is determined. Secondly, the rate limitation is measured in dependency of the state machine frequency to compare the experimental to the theoretical limitations. Lastly, local rate limitations depending on the beam size are measured.

Rate Limitation of GECCO DAQ: Ethernet

The rate limitation is measured with the 192 bit and 64 bit data format (Table 8.2) of the DAQ system to determine if the previously observed rate limitations are caused by the DAQ system. If the rate capability of the 64 bit data format is higher than that of the 192 bit data format, it is likely that the previously observed rate limitations are caused by the DAQ system. Therefore, the hit rate observed by the sensor is measured against the anode current of the X-ray tube, which is linearly dependent on the photon rate. It is assumed that rate instabilities of the tube are negligible. The sensor backside is irradiated using a 5 mm collimator with X-ray

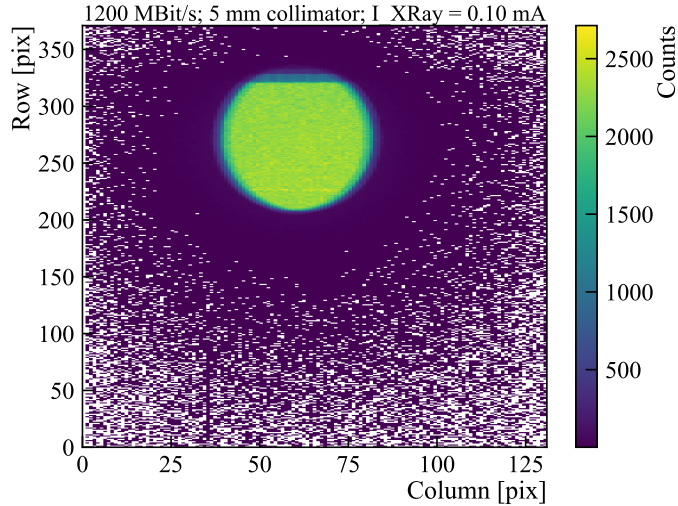


Figure 8.7: Measured beam profile of tungsten X-ray using a 5 mm collimator.

anode currents between 0.01 – 0.20 mA in steps of 0.01 mA. The measurement is performed using the 1200 Mbit/s readout configuration (external clock of 600 MHz), which has a theoretical rate limitation of 7.3 MHz (Table 8.1).

At lower photon rates, the measured rate is linearly dependent on the anode current for both readout data formats as expected (Figure 8.6). Moreover, the measured hit rate anode current dependency of both readout formats are compatible. However, the measured hit rate with the 192 bit data format (blue in Figure 8.6) drops steeply to 0.7 MHz at photon rates larger than 4.5 MHz. On the other hand, the hit rate measured with the 64 bit data format (orange in Figure 8.6) increases linearly to 6.0 MHz. After this point, the measured rate increases non-linearly to the next data point and stays constant at 7.5 MHz for the last data points. Looking at the beam profiles in Figure 8.7 and 8.8, the effects observed in the rate measurements of the two data formats can be explained.

Figure 8.7 shows the photon beam profile taken with the 64 bit data format at a hit rate of 6 MHz, where a linear dependency between anode current and hit rate is measured. The edge in the beam spot is caused by photo absorption in the material of the carrierboard to which the sensor under test is attached since the sensor is irradiated from the backside. The measured hit maps (Figure 8.8a) in the falling slope of rate measurement of the 192 bit data format at $I = 0.09$ and 0.10 mA show that pixels in columns with lower column addresses are less likely to be read out, although the beam profile of the X-ray tube is symmetrical in column direction, as seen in Figure 8.7. This kind of effect can not be caused by on-chip effects since during every readout cycle one hit in every column can be read out. Hence, this effect has to be caused by the DAQ system. Since the estimated hit rate of these two data points are above the 5 MHz limitation of the 192 bit data format, it is assumed that the DAQ system is the cause of the rate limitation. The observed structure in the measured hit map might be caused by a blocked FIFO in the DAQ system.

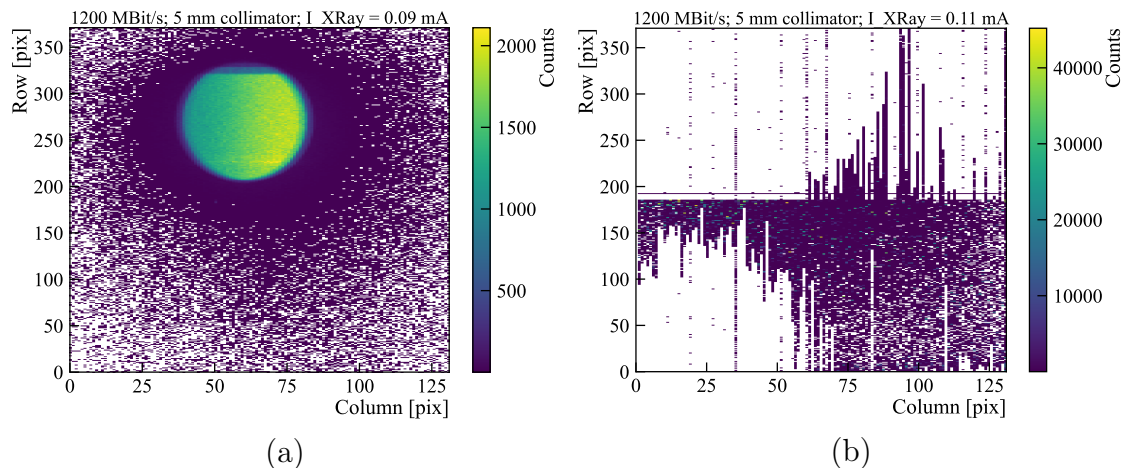


Figure 8.8: Hit map pattern observed above the Ethernet (a) and sensor state machine limitation (b).

The state machine on the sensor starts its readout cycle at column 131 and ends in column 0, therefore hits with high column number are sent to the DAQ system first. It is likely that, the FIFO of the UDP readout is full after the first couple of hits have arrived from the sensor. Thus, hits with lower column address are less likely to be send to the computer and written on the hard drive. The data measured at an X-ray current of more than 0.10 mA, which equals a photon rate of 6.5 MHz estimated by extrapolation, shows the same pattern in the measured hit maps of both data formats. The hit maps (Figure 8.8b) show an extreme column drain effect. A column drain effect is the effect that only pixels with low readout addresses² are read, while higher addresses are not. Since only one pixel per column can be read out in one readout cycle, only the hit with the lowest address is processed by the state machine. If the hit rate is so high that a second hit in a lower row occurs before a hit in a higher row is read, pixels in higher rows are not read at all from their hit buffers by the state machine. This effect is observed at a rate above 6 MHz in every column of the sensor. However, the hit rate outside of the beam spot is not high enough to cause a column drain effect there. This kind of hitmap pattern is also observed in a so-called oscillation state of the sensor. If the sensor is not configured correctly or the threshold is very low, an oscillation like structure is observed on the signal lines from the pixels to the periphery. These oscillations are an ATLASPix3(.1) specific problem and are currently under investigation. The data sent to the DAQ system is still valid and at least for the 64 bit data format, the data is sent with the maximum theoretical rate calculated. Thus, it is assumed that this effect might not be caused by the peripheral readout structure of sensor but by the in-pixel structure or the signal lines. However, this rate-induced oscillation is not understood. Because of the rate limitation observed with the larger data format, the 64 bit data format is used in the following rate measurements.

²Priority order: Row 185 \rightarrow 0; 186 \rightarrow 371

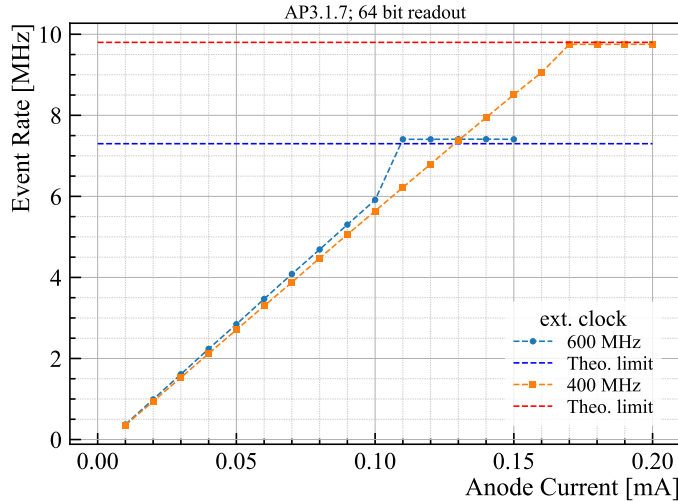


Figure 8.9: Measured hit rate with different readout and state machine speed against anode current of the X-ray tube. The theoretical rate limitations of the state machine are indicated with dashed lines.

Rate Limitation: State Machine

The next measurement performed determines the influence of the speed of the state machine on the rate capabilities of the sensor. For that, a hit rate measurement with the 800 Mbit/s readout mode (external clock of 400 MHz) and the 1.2 Gbit/s readout mode (external clock of 600 MHz) is performed. Since the base speed of the state machine of the 800 Mbit/s configuration is lower than in the 1.2 Gbit/s configuration (Table 8.1), the state machine can run at its base speed without an extra slow-down factor ($\text{timerend} = 0$). As a consequence, a higher rate capability of 9.8 MHz is expected for the 800 Mbit/s readout mode (Table 8.1). A rate measurement with a 5 mm collimator is performed for both sensor configurations.

The hit rate measurements and the theoretical limitations of the two state machine speeds are shown in Figure 8.9. As described in the previous section, the hit rate measured with the 1.2 Gbit/s readout (blue in Figure 8.9) increases linearly with the anode current of the X-ray tube up to a hit rate of 6 MHz. At higher photon rates the sensor measures only a noise oscillation pattern with a rate of 7.5 MHz. On the other hand, the rate measured with the 800 Mbit/s readout speed (orange in Figure 8.9) increases linearly to 9.7 MHz. At higher photon rates (anode currents) the measured hit rate is constant at 9.7 MHz. Unlike with the 1.2 Gbit/s readout speed, the sensor does not oscillate at photon rates higher than the hit rate limitations, which can be seen from the pattern observed in the hitmap (Figure 8.10). Although the pattern of the 800 Mbit/s readout seems to be similar to the oscillation patterns, a beam spot can still be seen in the hitmap at photon rates above 9.7 MHz. The beam spot (column ~ 40 to ~ 80) shows a column drain effect. Since the photon rate is higher than the rate limitations of the state machine, the FSM can not process all hits in a column before new hits in lower rows occur. As a result pixels, in higher

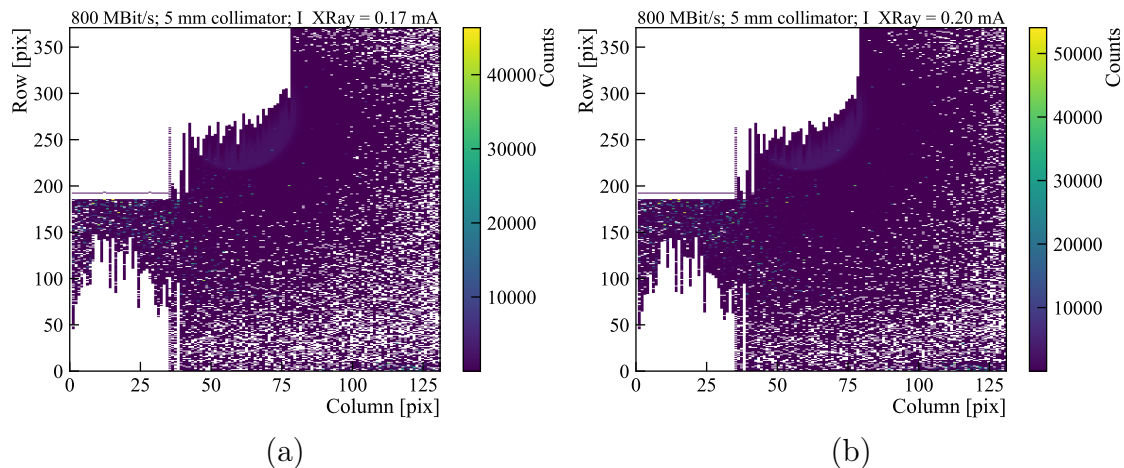


Figure 8.10: Hit map pattern observed above the rate limitations of the 800 Mbit/s readout.

rows are not read out. This hypothesis is supported by the fact that the column drain effect in the beam spot slightly increases with the anode current and so the incident photon rate as well (Figure 8.10). However, the column drain effect should be symmetric in columns in respect to the center of the beam spot, which is not observed here. A second column drain effect-like structure is observed on the left side of the beam spot (column 0 to ~ 40). This structure is caused by highly noisy pixels between rows 150 – 185, which block the column drain for pixel with higher row addresses. This noise is not observed at lower photon rates. It is still under investigation why this noise is created at this the photon rate.

The theoretical rate limitations of the state machine agree well with the measured limitations. The sensor is operational up to the last hit rate data point before the rate limitation. At photon rates above the rate limitation of the state machine, noise pattern with hit rates close to the theoretical rate limitations are observed. The occurrence of noise patterns at photon rates close to the theoretical rate limitation needs to be studied with higher granularity in photon rate. This could be achieved by for example inserting photon absorbers between the X-ray beam and the sensor under test.

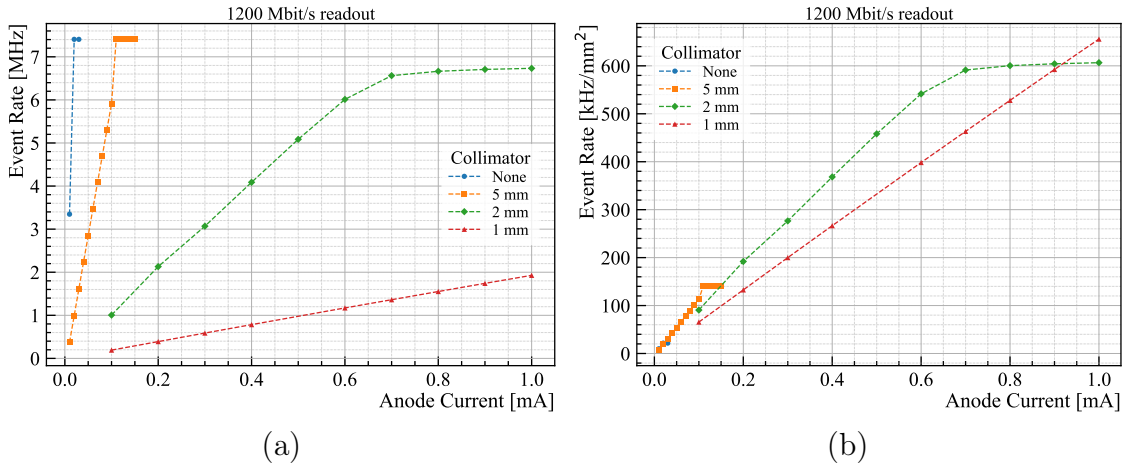


Figure 8.11: Rate measurement of different collimator sizes in terms of global rate (a) and local rate (b)

Beam Spot Size

Lastly, the impact of the beam size on the rate limitations is studied. For that, measurements with 1 and 2 mm collimators and no collimator are taken and compared to the 5 mm collimator measurement. The 1.2 Gbit/s readout configuration with the theoretical hit rate limitation of 7.3 MHz is used (Table 8.1).

The measured hit rate against the anode current of the four different collimator sizes is shown in Figure 8.11a. For the measurements with the 1 and 2 mm collimator the entire current (photon rate) range of the tube is used. The hit rate measurement with the 1 mm collimator is below 2 MHz for the whole anode current range of the tube. As shown in Figure 8.13a, no rate dependent effects in the beam profile are observed. The hit rate measured with the 2 mm collimator increases linearly with the X-ray anode current from 1 to 6 MHz. Figure 8.12a shows the beam profile of a 2 mm photon beam taken at a hit rate of 6 MHz. After this data point, the measured hit rate saturates to 6.8 MHz. This saturation is created by a column drain effect in the beam spot, which can be seen in the beam profile taken at an anode current of 1 mA in Figure 8.12b. The local rate in the beam spot is so high that pixels in higher rows are not read out before a hit in the same column but with lower row address is registered. Therefore, higher rows are not read out. In contrast to the 5 mm collimator measurement, no noise structures are observed and the column drain effect is limited to the beam spot. Without a collimator, only the hit rate of the lowest anode current can be measured. At the second lowest anode current, the hit rate estimated by extrapolation is above the theoretical rate limitations of the sensor and the sensor measures oscillation patterns. Since the sensor under test is irradiated from the backside, the structure of the carrierboard on which the sensor is attached and bonded is visible in the beam profile (Figure 8.13b) due to photo-absorption in the material of the carrierboard. The edges of the sensor measure a lower photon rate, since they are attached to the carrierboard

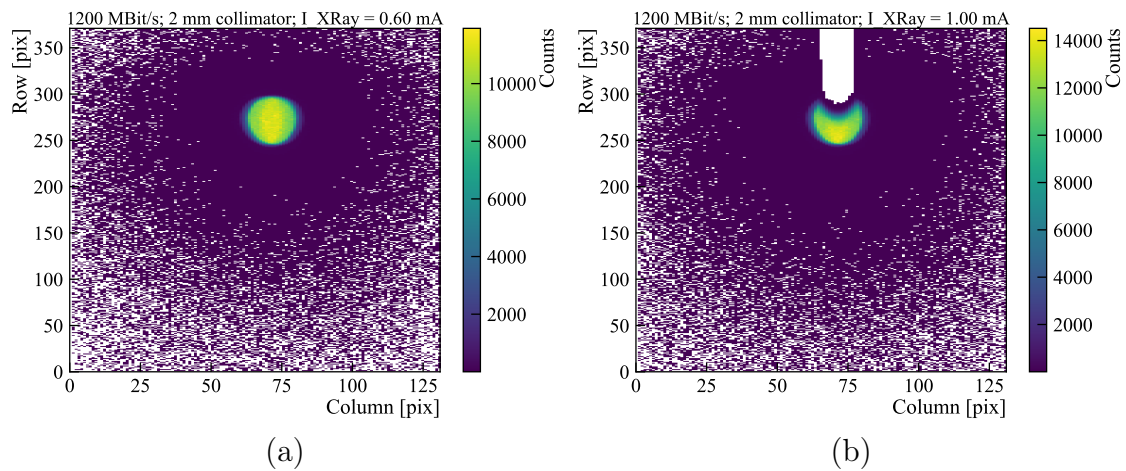


Figure 8.12: Measured X-ray beam profile using a 2 mm collimator at 6 MHz (a) and 6.8 MHz (b).

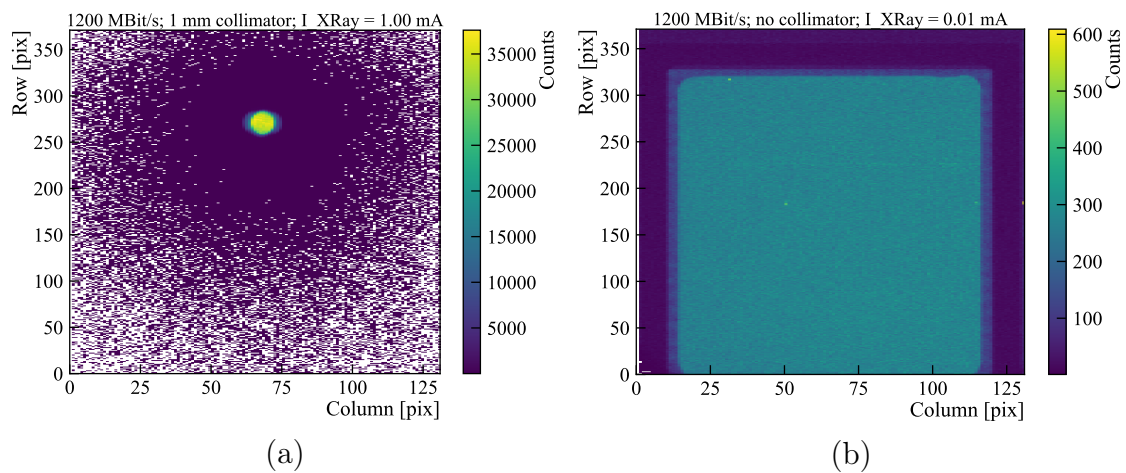


Figure 8.13: Beam profile measured with a 1 mm collimator (a) and without a collimator (b).

Readout	Collimator	Theoretical Rate Limitation	Experimental Rate Limitation	Cause of Limitation
800 Mbit/s	5 mm	9.8 MHz	9.7 MHz	Column drain
1200 Mbit/s	None	7.3 MHz	3.4 MHz	Sensor Oscillation
1200 Mbit/s	5 mm	7.3 MHz	6.0 MHz	Sensor Oscillation
1200 Mbit/s	2 mm	7.3 MHz	6.8 MHz	Column drain
1200 Mbit/s	1 mm	7.3 MHz	–	Limit above measure range

Table 8.3: Theoretical and measured hit rate limitations of the ATLASPix3.1

while the center of the sensor measures a higher hit rate since the carrierboard is cut out behind the center of the sensor.

These measurements show that the hit rate limitation of the state machine does not depend on the number of irradiated pixels. However, effects caused by the column drain mechanism are possible at high local rates. For example, the local rate is 540 kHz/mm² in the 2 mm beam spot when the column drain effect occurs. Figure 8.11b shows the local rate as a function of the X-ray current for the four different collimator measurements performed. Since the readout is limited by the global rate, a higher local rate is achieved for smaller beam profiles. With the 1 mm collimator, the highest local hit rate is achievable. At the highest possible anode current of 1 mA, the hit rate reaches almost 660 kHz/mm² in the beam spot. This value is more than 5 times higher than the expected mean local particle rate of the hottest sensor at the MightyTracker (125 kHz/mm²) [19]. This measurement shows that the in-pixel electronics of the AP3.1 are capable of operation at MightyTracker-like particle rates.

8.2.3 Summary

The hit rate limitations of the ATLASPix3.1 are determined for different readout speeds and depending on the collimator sizes. The observed rate limitations agree with the theoretically calculated rate limitations. The results of the rate measurements are summarized in Table 8.3, where the experimental rate limitations are given by the highest hit rate at which physical data is measured.

A 20×20 mm² sized sensor, which is located at the innermost region of the MightyTracker, is expected to detect a mean of 1.7 particles per non-empty bunch crossing. [19] At a non-empty bunch crossing rate of 30 MHz, this results in a particle rate of 50 MHz per 20×20 mm². This is about 5 times higher than the measured hit rate limitation of the ATLASPix3.1. Therefore, the readout of the MightyPix v1 is structured differently. The number of data links is increased from 1 link to 4 links, which reduces the active area per data link by a factor of four (5×20 mm²). As a consequence, the mean particle rate per data link and readout structure is reduced to 12.5 MHz and only 29 columns are read out by one finite state machine. The state machine of the MightyPix v1 will run at 40 MHz and will have a link speed

of 1.28 Gbit/s achieving a rate capability above 12.5 MHz. This hit rate capability is sufficient for the sensors in the outer regions but not in the innermost part of the MightyTracker, where peak particle rates exceeding the rate capabilities can occur. [33] In principal, the state machine of the MightyPix v1 could be operated at higher frequencies which would increase the rate capability. However, a faster state machine of 80 MHz would increase the data stream from 1.28 Gbit/s to 2.56 Gbit/s for example. Further investigation has to be undertaken to determine whether a link speed higher than 1.28 Gbit/s to the DAQ system is feasible for the innermost sensors or if the data size per hit can be reduced to operate the sensor with a faster state machine and a link speed of 1.28 Gbit/s.

9 Ion Beam Measurements

An ion beam is useful to determine the response of the ATLASPix3.1 to very large energy depositions, which might occur at a low rate in MightyPix sensors in the MightyTracker. With a carbon ion beam, energy deposition 100 times larger than that of a MIP can be created. A large energy deposition in the sensor can lead to saturation effects in the amplifier circuit or can increase the occupancy in the sensor due to extensive charge sharing created by the large energy deposition. Large charge generation by ions in the DAC registers and RAM of the sensor could lead to single event upsets, which changes the sensor parameters and configurations, resulting in an altered sensor response.

Within the scope of this thesis, it was possible to join a testbeam effort for a scintillating fiber beam monitor at the Heidelberg Ion Therapy center [43]. Typically, the synchrotron provides ion beams with intensities of up to $10^6 - 10^9 \text{ s}^{-1}$ depending on the ion type. Since the testbeam at HIT was for a beam monitor, which operates at lower intensities, the beam intensities of this campaign were chosen to be $\mathcal{O}(10^4 - 10^5 \text{ s}^{-1})$. The intensities and particle types are varied for different measurements. Table 9.1 provides an overview of the different particle beams used during the testbeam. Three different types of beam particle were provided during the testbeam: protons, helium and carbon ions. The helium ion and proton beam measurements are taken with one energy setting, while the carbon ion beam is measured at 4 different energy settings (Table 9.1). The measurement setup at HIT is shown in Figure 9.1. For measurements with the helium beam, the scintillating fiber detector is placed in front of the AP3.1 as shown in Figure 9.1, while for measurements with the carbon ion and proton beam, the position of the two detectors is switched. No shielding is applied in front of the peripheral structure of the sensor as it will be the case for the MightyPix sensor at the MightyTracker. Therefore, significant energy is deposited in the configuration registers and the readout structure.

During the testbeam, the sensor experienced an increased amount of noise and crosstalk. It is found that the noise and crosstalk is created by a bad grounding scheme of the sensor and DAQ system. However, the grounding problem could not be fixed during the testbeam, since the testbeam lasted only for 5 hours in one night. Therefore, the following measurements show significant noise and crosstalk.

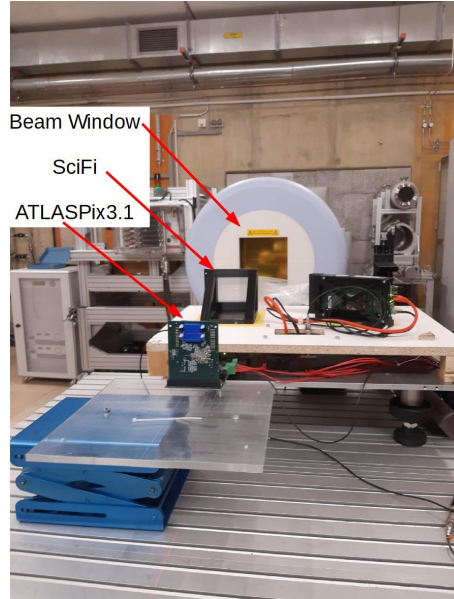


Figure 9.1: Measurement setup at the HIT testbeam. The scintillating fiber beam monitor is indicated as SciFi here.

Particle	Beam Energy [MeV/u]	Beam Energy [MeV]	Energy Deposition [MeV/mm]
Proton	221	221	0.795
Helium Ion	220	880	3.19
Carbon Ion	430	5160	20.0
Carbon Ion	354	4250	22.0
Carbon Ion	242	2900	27.1
Carbon Ion	176	2110	33.1
MIP			0.390

Table 9.1: Particle types and their energies used for measurements during the HIT testbeam. The mean energy deposition is calculated using the Bethe formula (Equation 4.1). The energy deposition of a MIP in silicon is included as a reference.

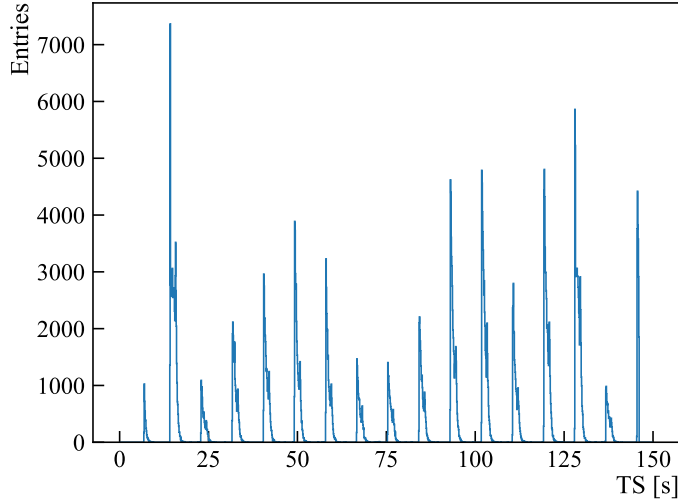


Figure 9.2: Histogram of the time-of-arrival timestamp TS1 of a measurement with helium ions of $E = 220$ MeV/u.

9.1 Spill Structure

To verify the proper operation of the sensor under test the measured spill structure is analyzed and compared to the specifications of the accelerator. In standard operation, HIT's synchrotron provides ion spills of 3 s with a constant intensity every 8 s. Since the machine is operated below its typical intensity settings during our test, the intensity control mechanism can not provide constant intensities during a spill. Moreover, the intensities vary between spills.

For all particle types, the measured spill structure agrees with the specification of a 3 s spill with 5 s break between the spills. Figure 9.2 shows the histogram of hit timestamps TS1 of a measurement with helium ions with an energy of 220 MeV/u. The histogram displays the structure and the varying intensities of the spills produced by HIT. If one neglects the intensity difference, the structure of the spills is as expected. Figure 9.3a shows a zoom into a single spill. At the beginning, a short ramp up of intensity is observed. Then, the intensity falls almost exponentially for the first second of the spill. After the first second, the intensity control mechanism attempts to ramp up the intensity, which results in a second intensity peak. After this second peak, the spill fades out. Due to problems with the DAQ system, which can not be solved during the test beam, the UDP based readout is not used. Hence, the USB readout of the FPGA has to be used. Since the particle rates are above the limitations of the USB readout, data is lost randomly in the FIFO of the FPGA, resulting in saturation effects in the measured spill structure (Figure 9.3b). Thus, it is not possible to determine the hit rate on the sensor from the sensor data itself. Since the scintillating fiber beam monitor and the ATLASPix3.1 are not aligned, the data collected by the fiber detector can not be used to determine the particle rate on

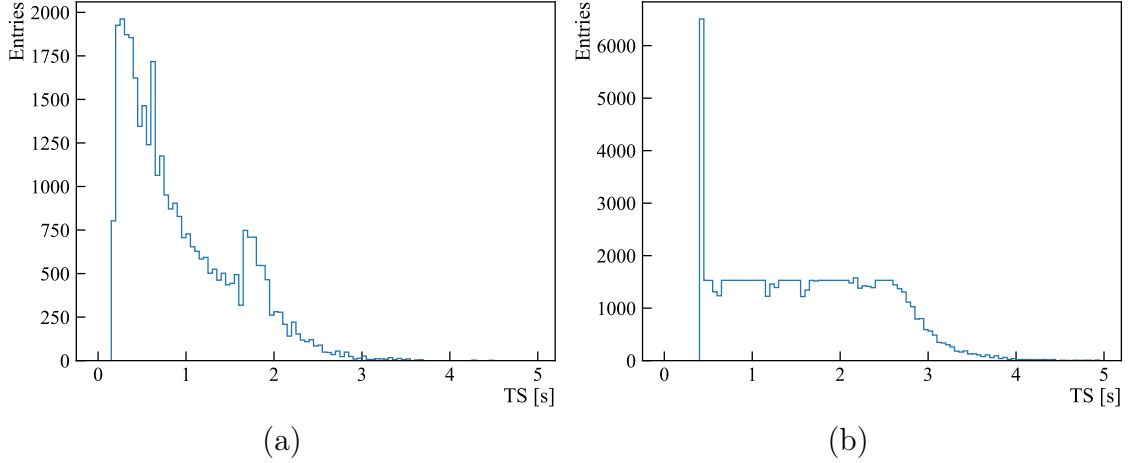


Figure 9.3: Timestamp distribution of a spill of helium ions with energy of $E = 220$ MeV/u at lower (a) and higher (b) intensities showing the saturation effect.

the silicon sensor either. However, the time structure observed by the scintillating fiber detector is similar to the time structure measured with the AP3.1 [44].

9.2 Energy Spectra & Clustering

Since the energy deposition of ion beams is much larger than that of radioactive sources in the lab, it is of interest to analyze the response of the sensor for high energy depositions. Table 9.1 shows the calculated energy deposition of the different particles and beam energies measured during the test beam. Comparing the energy deposition of the ions with the energy loss of a MIP in silicon, one sees that the helium ion beam deposits an energy 10 times higher in the silicon than a MIP, while the carbon ion beam loses up to 100 times more energy in silicon than a MIP. Since the amplifier of the ATLASPix3(.1) is designed to detect MIP-like particles, it is expected that the energy deposition in the sensor diode creates a charge pulse, which saturates the amplifier leading to saturation effects in the ToT response.

Figure 9.2 shows the hit profiles measured with the proton, helium ion and carbon ion beam. From the hitmaps it is already visible that the high energy deposition of ions in the active area and the periphery does not lead to oscillation effects as observed in the X-ray measurements in Chapter 8. However, the large energy deposition in the detector leads to large clusters of hits in the beam profiles of helium and carbon ion measurements. Hence, a cluster algorithm is developed and applied to the data.

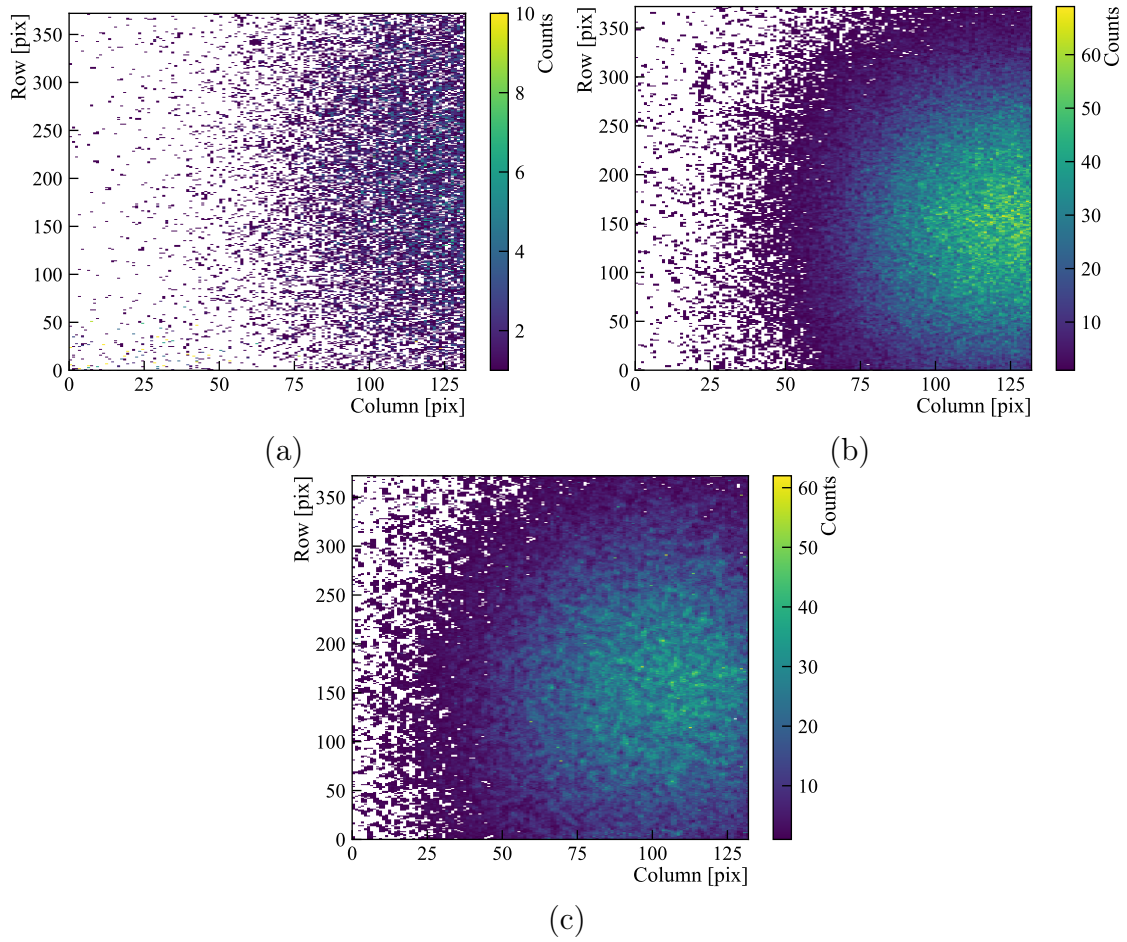


Figure 9.4: Beam profiles of proton of 221 MeV/u (a), helium ion of 220 MeV/u (b) and carbon ion of 176 MeV/u measured at HIT.

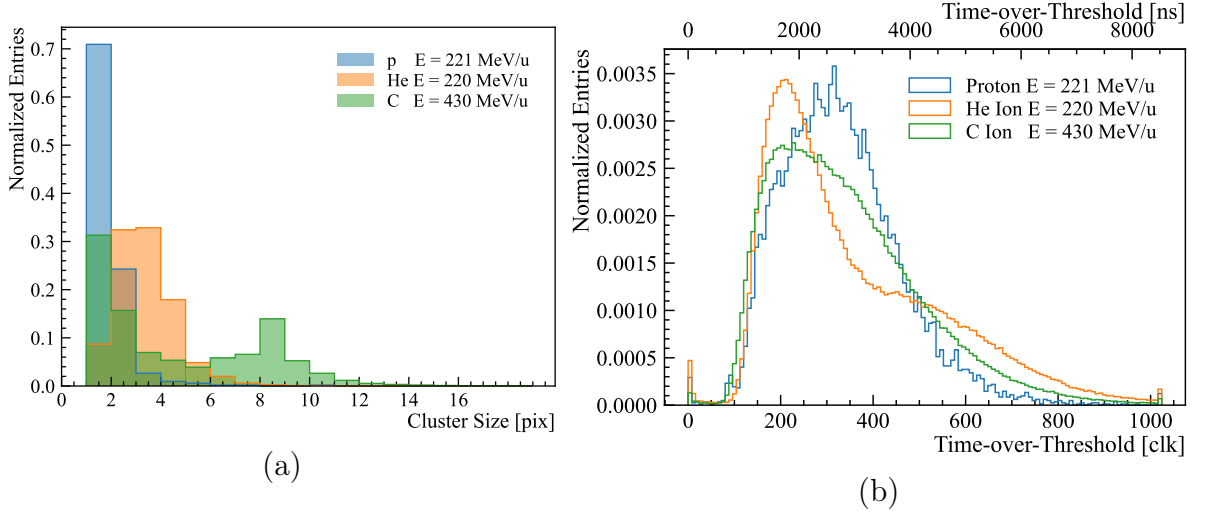


Figure 9.5: a) Cluster size distribution observed at HIT for proton, helium and carbon ion beams. b) Time-over-threshold distribution of single hits occurred in protons, helium and carbon ion measurements in clock cycles and ns measured at HIT. No clustering applied.

Since the rate is rather low and the beam spot is large, loose clustering cuts are applied. The clustering algorithm starts with a so-called seed pixel which is the first hit of the cluster recorded by the sensor. Other hits are added to this cluster if they occur in a time window of $4 \mu\text{s}$ together with the seed hit and if their distance to the cluster is below 5 pixels. Due to the difference in energy deposition the average cluster size varies between ion types. The size of the resulting hit clusters of the 3 different particle types is shown in Figure 9.5a. The proton beam produces hit clusters with a mean size of 1 pixel and the helium beam clusters with a mean size of 2 – 3 pixels. In contrast, the carbon ion beam produces two different types of clusters: one with a mean cluster size of 1 and larger clusters with a mean cluster size of 8. The data has to be further analyzed to understand the two peak structures in the carbon ion measurement.

It is expected that the ToT spectra of different ion types differ, caused by their differing energy deposition in the sensor. The measured time-over-threshold spectra, where no clustering is applied to the data, (Figure 9.5b) differ from the spectra measured with electrons and photons in previous chapters (Figure 7.9b and 8.4b). In all ToT spectra of ion beams, no clear peak structure as in the lab measurements is visible. Naively, one would expect that there is a clear order of peak positions. The peak of the carbon ToT spectrum should have the largest average ToT value and the proton spectrum the lowest average ToT value of the three particles. In contrast, the ToT spectra of helium and carbon ions peak below the ToT spectrum of protons. This is caused by the formation of hit cluster for the carbon and helium ion beams. The peaks at low ToT values in the spectra of the helium and carbon ion

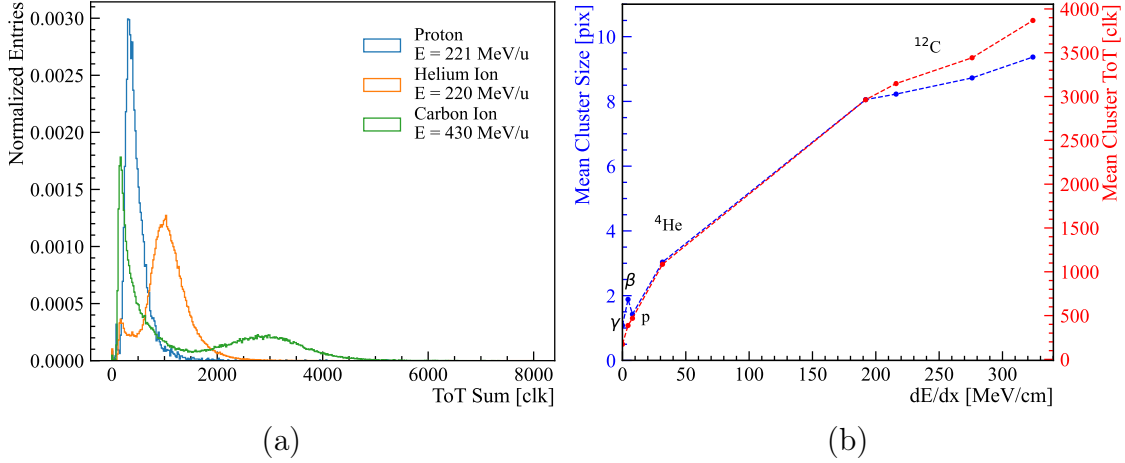


Figure 9.6: a) Sum of the ToT response of clusters for proton, helium and carbon ion beam. b) Mean measured cluster size (blue) and mean cluster ToT (red) as a function of the energy deposition in silicon with the particle type indicated. A cut on the non-ion like cluster of the carbon measurement is set at cluster size > 4 pixels.

beam are created by pixels measuring charge sharing, since pixels detecting charge sharing measure smaller signals with lower ToT values. The tail structure towards higher ToT values is created by the ion hits. Since the ToT response varies between pixels and the amplifier of the pixels saturate at different amplitudes, the ion hits do not create a peak but a tail structure in the ToT measurement. Furthermore, the ToT distributions of helium and carbon ions extend over the entire acceptance range of the time-over-threshold measurement of $8.5 \mu\text{s}$. As can be seen, the ToT spectrum of carbon is non-zero at the maximum possible ToT value of 1024 clks ($8.5 \mu\text{s}$). Time-over-thresholds larger than $8.5 \mu\text{s}$ lead to an overflow of the ToT measurement and are recorded with a lower ToT value. However, this effect contributes to less than 1% in the measurements performed here.

To compare the ToT measurement and energy deposition of the different particle types, the ToT response of a cluster has to be calculated. Although the ToT response between different pixels varies non-linearly, the ToT measurement of the pixels in a cluster is summed up to obtain an estimation of the energy loss of the particle detected. The non-linearity is caused by three different effects described in Section 7.3.1. Figure 9.6a shows the resulting ToT cluster distributions of the proton, helium ion and carbon ion measurement. In this distribution the expected order of peak position of the different ions is observed. The ToT sum of the proton clusters peaks at a similar ToT value as in Figure 9.5b where no clustering is applied, since the protons produce hit clusters with a mean size of almost 1. Since the helium beam produces hit clusters with a size of 2 to 3 pixels, the ToT sum of the helium ion measurements peaks at 1000 clks. In the cluster ToT distribution of the carbon beam, two peak structures are seen similar to the cluster size distribution: A broad

peak at higher ToT values of 3000 clks and a sharp peak below 500 clks. This leads to the assumption that not only carbon ions but also another type of particle are detected by the sensor. The origin of this second particle type is studied in detail in the next section. For now it is assumed that the cluster with high ToT and larger cluster size corresponds to the ion hit. Neglecting the second peak at low ToT in the carbon ToT sum distribution, a positive dependency between energy deposition and ToT response is observed.

Since the mean cluster size and the mean cluster ToT are positive dependent on the energy deposition, the mean cluster size and mean cluster ToT can be used as estimative measure of the energy deposition. The mean ToT of a cluster as a function of the energy deposition in silicon is shown in red in Figure 9.6b, while the mean cluster size as a function of the energy deposition is shown in blue. A cut is set on the non-ion-like clusters (cluster size < 4) for the calculation of the mean cluster size and mean cluster ToT in the carbon measurements, since it is assumed that these clusters are not caused by carbon hits. In addition to the HIT measurements, Figure 9.6b includes the typical cluster size and ToT observed in lab measurements with β -particles from strontium-90 (Figure 7.9b and 7.10) and photons from the X-ray tube (Figure 8.1a and 8.4b). In Figure 9.6b, an increase in cluster size and ToT with the energy deposition is observed. However, the β -particles from ^{90}Sr produce larger cluster sizes than the protons from the HIT beam even so the energy deposition is lower. This is likely caused by a skewed track of the electrons through the sensor, since the radioactive source is not orthogonally aligned to the sensor and the beam profile of the source is diffuse (Figure 7.7a). The increase in cluster size and ToT with energy deposition is expected since the number of electron-hole pairs produced in the silicon substrate, which create the signal amplitude and can be shared between pixels, is proportional to the energy deposition. However, both measured quantities are not linearly dependent on the energy deposition and a saturation effect is observed. The saturation of the energy dependency of the mean cluster ToT is likely caused by the saturation of the ToT measurement for large energy depositions, described previously. The saturation effect of the mean cluster size is likely caused by a suppression of signals created by charge sharing which have a low amplitude. Since the signal created by charge sharing decreases with the distance from the particle hit, outer pixels of the cluster measure a signal which does not pass the threshold.

For the carbon data it is observed that the ion-like cluster extends in time up to 3.5 μs , where the signal in outer pixels of the cluster arrives later. The time distribution of the cluster is spatially symmetric around the seed hit, such that a skewed track can be excluded. It is assumed that these hits are produced by lateral diffusion caused by ionization in the undepleted region of the sensor. Since the electrons created in the undepleted region are diffusing into the depletion zone, they are delayed by the diffusion time. Since the sensor under test is not thinned, more than 600 μm of undepleted silicon is beneath the depletion zone. It is unknown how

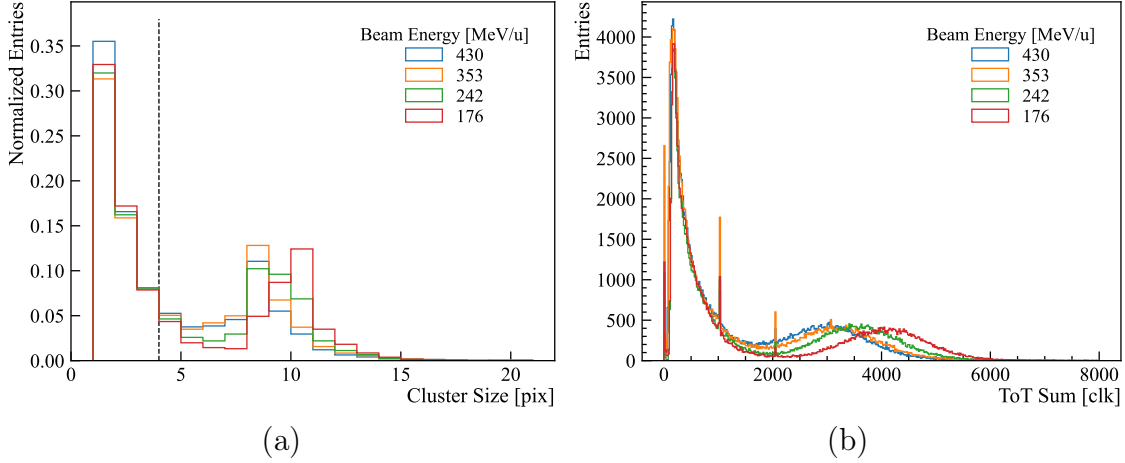


Figure 9.7: a) Measured cluster size distribution of carbon ions for four different beam energies. The black dashed line indicates the cut used between ion-like and non-ion-like cluster. b) Distribution of the ToT sum of clusters for different carbon beam energies. The peaks at 0, 1024 and 2048 clock cycles are created by crosstalk.

many of the electron-hole-pairs created in the undepleted region contribute to the signal seen in the pixels. Since no thinned sensor is available, the difference between an almost completely depleted sensor and a largely undepleted sensor can not be determined experimentally. Delayed hits are not observed in the data of protons and helium. Since helium and protons create 10 and 100 times fewer electron-hole pairs in silicon than carbon ions (Table 9.1), respectively, this might be a hint that only a fraction of the diffusing charges are reaching the depletion zone and create a signal which passes the threshold. Therefore, the influence of diffusing electrons on the signal is studied in a simulation performed in Section 9.3.2.

9.2.1 Cluster Analysis of the Carbon Ion Measurements

In this section, the cluster structure of the carbon beam is analyzed to study the origin of the two types of clusters. Comparing the cluster size histograms of different beam energies of carbon ions (Figure 9.7a), it is observed that the distribution of the small clusters (size < 4) does not change with energy, although the cluster size of the larger clusters (size ≥ 4) decreases with the beam energy (increases with energy deposition). This leads to the assumption that the small clusters are not caused by the ions from the beam.

The sum of the ToT of hits in a cluster can serve as hint for the energy of the particle causing the cluster. Figure 9.7b shows the histogram of the ToT sum distribution of the 4 different energies of the carbon beam used. The histogram shows two peaks for all beam energies: A sharp one at lower ToT below 500 clks and a broad peak at ToT larger than 2000 clks. The peak position of the broad peaks

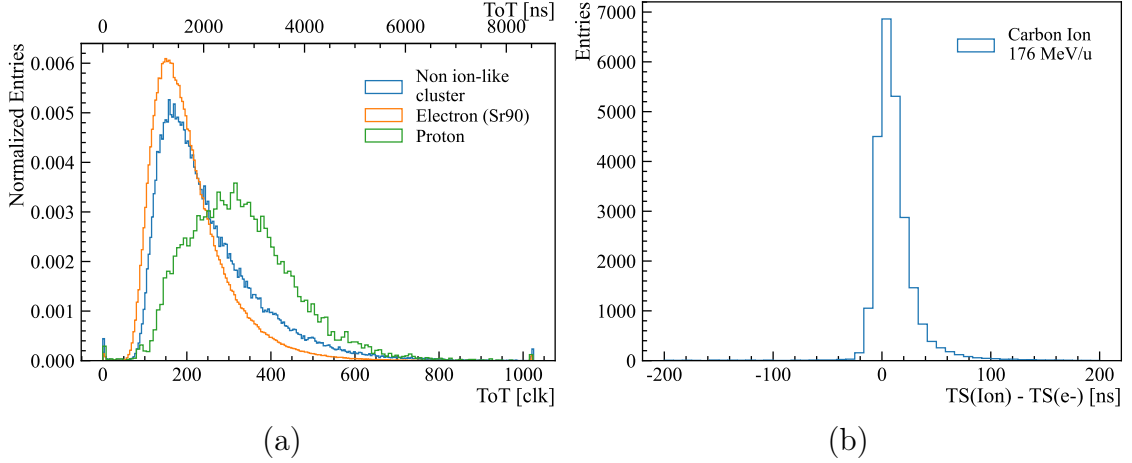


Figure 9.8: a) Comparison of the ToT histogram of non-ion-like clusters observed in the carbon beam measurement with the ToT distributions of electrons and protons. b) Measured time difference between a carbon-like cluster and an electron-like cluster.

shifts towards higher ToT with decreasing beam energy which is expected as the energy transfer to the sensor increases. In contrast, the position of the sharp peak at lower energies does not change with the beam energy. This is in accordance with the hypothesis that these hits are "non-ion like".

The ToT distribution of the non-ion-like small clusters is compared to the ToT spectra of electrons and protons to hint on the particle type of these clusters (Figure 9.8a). The electron ToT spectrum is measured with ^{90}Sr β -particles in the lab, while the proton ToT is measured at HIT. The comparison of the spectra shows that the ToT of the non-ion like clusters is similar to the ToT distribution of electrons. Therefore, these clusters are called "electron-like" in the following.

Another argument for the hypothesis that there is another type of particle measured is the time structure between the ion- and electron-like hits. Electron-like clusters are heavily time correlated to the ion-like clusters, however they are not spatially correlated. The time difference between ion-like and electron-like hits is shown in Figure 9.8b. The minimum difference between the seed timestamp of the ion-like and electron-like clusters peaks around 10 ns, where the peak width is mainly given by the time resolution of the sensor and is affected by timewalk, since all electron-like hits have small ToT (Figure 9.7b). Although they are heavily time-correlated, these electron-like hits are not delta electrons created by an ion hit in the silicon, since delta electrons are created by an ion hit and are therefore spatially correlated with the ion hit. Additionally, almost all delta electrons are clustered together with the ion hits because of their small range in silicon and the clustering cuts applied to the data. At this point, no other production process of these electron-like particles is obvious such that a simulation studying this effect is performed in Section 9.3.1.

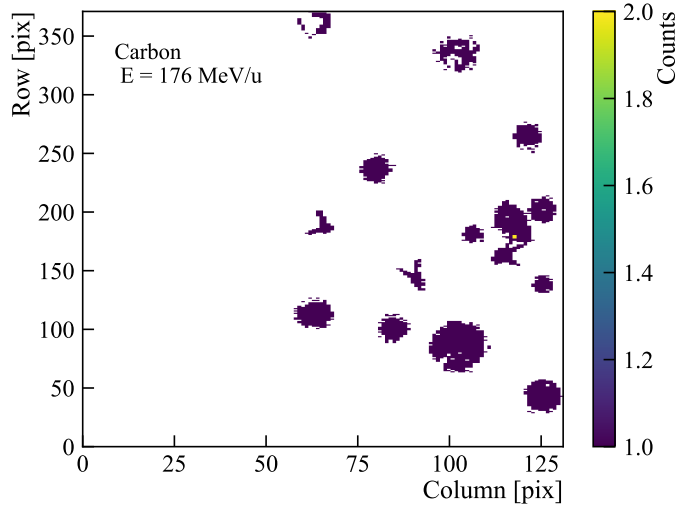


Figure 9.9: Position and structure of bumps measured with carbon ion beam with an energy of 176 MeV/u.

9.2.2 Bumps

In the measurements of helium and carbon beams, very large hit clusters with a size of more than 75 pixels are observed (Figure 9.10a). Because of their size and their round profile, they are referred to as bumps in the following. Bumps that have occurred in a measurement of carbon ions with a beam energy of 176 MeV/u can be seen in Figure 9.9. The non-circular clusters observed in this hit map are caused by delta-electrons scattering in the sensor until they are absorbed. Due to the readout limitations caused by a blocked FIFO on the FPGA, some hits of a bump are not recorded, which can be seen by the missing hits in the center of the bumps in Figure 9.9. Each of these so-called bumps has a seed pixel with a high ToT in the center of the cluster and the ToT distribution of the hits in a bump decreases towards the edges of the cluster. Because of their large size their readout is delayed by buffer times in the column drain up to 100 μs . For a correct time ordering on the FPGA a hit has to be read out in the time period of the 10 bit TS1 of 8.5 μs (600 Mbit/s readout), otherwise a TS1 with a delay of 8.5 μs is assigned to the hit. Therefore, hits of bumps with higher row addresses are delayed by multiple TS1 time periods. Hence, bumps are very hard to detect in the data and therefore to assign to the cluster. However, the delay effect can be corrected in the clustering algorithm. Firstly, the time cut on the time ordering timestamp is set above 100 μs to be able to cluster bump hits to one cluster. However, this reduces the efficiency of the clustering algorithm, because hits are assigned to a cluster to which they are not connected. This effect can be reduced by introducing an additional time cut on the 10 bit TS1 (8.5 μs), which is not delayed by the readout. This second time cut is set to 4 μs as in the clustering algorithm in the previous sections. Because of the low rate, this change in the clustering algorithm has no influence on the clustering performance of non-bump clusters.

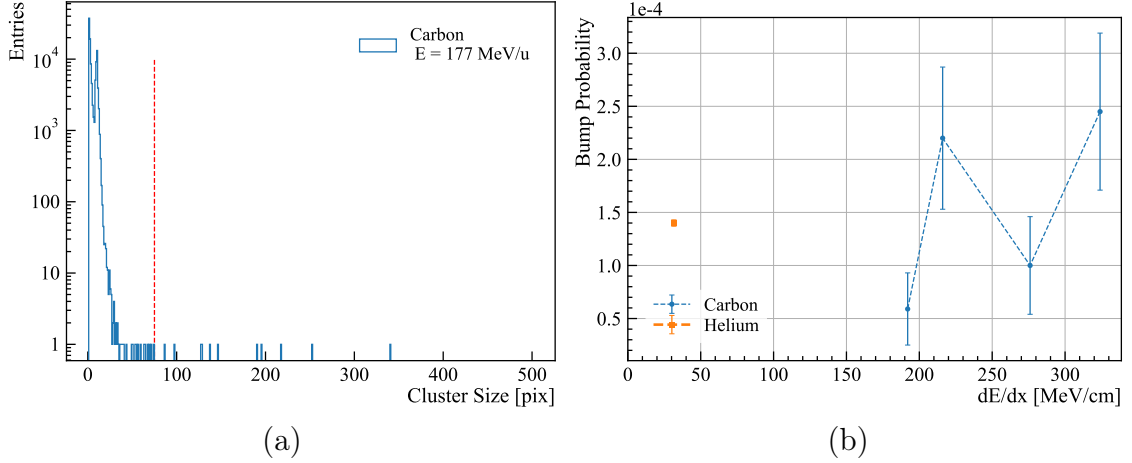


Figure 9.10: a) Logarithmic histogram of the measured cluster size distribution with a carbon ion beam of $E = 176$ MeV/u. The red dashed line indicates the definition of a bump by cluster size. b) The occurrence probability of a bump by particle type and energy deposition.

Since a physical ToT structure similar to the hit clusters is observed, it is unlikely that these bumps are created by an electronic effect on the sensor. A first assumption is that these bumps are statistical outliers of the energy deposition distribution of the ionization. If this is the case, the probability of the occurrence of a bump will increase with the energy deposition. Therefore, the probability P_{bump} of the occurrence of a bump is calculated for the different ion types and beam energies.

$$P_{\text{bump}} = \frac{N_{\text{cluster} > 75}}{N_{\text{cluster}}} \quad (9.1)$$

N_{cluster} describes the total number of measured clusters, while $N_{\text{cluster} > 75}$ describes the number of clusters with a size larger than 75 pixels. The statistical uncertainty on the bump probability is described by σ_P :

$$\sigma_P = \frac{\sqrt{N_{\text{cluster} > 75}}}{N_{\text{cluster}}} \quad (9.2)$$

For the probability calculation, a cut on the electron-like clusters in the carbon measurements is set. Because of this cut on the carbon measurement, the statistical uncertainties on the bump probability of the carbon measurements are larger than on the helium measurement. Unfortunately, the calculation of the bump probability suffers from the data loss in the USB FIFO, which is not considered in the calculation of the uncertainties. Figure 9.10b shows the bump probability against the mean energy deposition of the beam. No energy dependence on the probability, especially in the difference between helium and carbon ions, is found. Thus, it can be concluded that these bumps are no statistical outliers of the ionization distribution.

Ion	Geometric cross section	Target length	Bump probability
Helium	5300 mb	100 μm	2.7×10^{-3}
		600 μm	1.6×10^{-2}
Carbon	7100 mb	100 μm	3.5×10^{-3}
		600 μm	2.1×10^{-2}

Table 9.2: Calculated geometrical cross section of helium and carbon ion nuclear interaction with silicon using Equation 9.3 and 9.4.

The bump occurrence is independent of the energy deposition and these bumps could be created by nuclear interaction between ion beam and the silicon of the sensor substrate. This hypothesis is consistent with the non-observation of bumps in measurements with protons, since they are less likely to collide inelastically with the silicon atoms because of their nucleon number of 1. A theoretical upper limit on the probability of nuclear interaction can be calculated using the geometrical cross section σ :

$$\sigma = \pi r_0^2 (A_{\text{Si}}^{1/3} + A_{\text{Ion}}^{1/3})^2 \quad (9.3)$$

where r_0 is the electron radius and A the nucleon number. From the cross section the interaction probability P_{IA} is determined:

$$P_{\text{IA}} = n\sigma x \quad (9.4)$$

where n is the atom density of silicon and x the target length. Since the effect of ionization in the undepleted region is not known, the interaction probability is calculated for a thickness of 100 and 600 μm for helium and carbon ions, which is an upper limit on the size of the depletion zone and a lower limit on the size of the undepleted region. The results are shown in Table 9.2. The upper limit on the interaction probability for 100 μm silicon is one order of magnitude larger and for 600 μm silicon two orders of magnitude larger than the measured probability of a bump. The observed bumps can thus be caused by nuclear interaction and this hypothesis has to be studied further using a simulation.

9.2.3 Sensor Response

Since large energy depositions in the sensor might change the response or damage the sensor, the sensor response is monitored. During the operation at HIT, no significant change in sensor response is observed. It is therefore assumed that the ion beam and bumps do not lead to a measurable rate of single event upsets in the periphery of the sensor at the measured beam intensities. This assumption has to be verified with a measurement on the change of the configuration stored in the DAC registers in the periphery of the sensor during ion beam irradiation, which was not performed during the testbeam campaign. Before and after the measurement

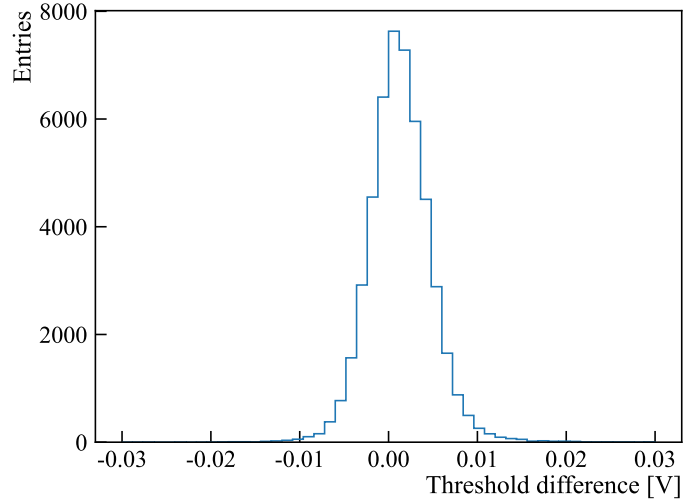


Figure 9.11: Threshold difference per pixel between S-Curve measurements before and after the HIT testbeam.

at HIT, S-Curve measurements are taken to determine a possible permanent change in sensor response. The threshold distribution of both measurements is compatible in terms of the measurement accuracy and all pixels are responding. Figure 9.11 shows the distribution of the threshold changes per pixels between the two S-Curve measurements. Moreover, both S-Curve measurements yield a compatible noise distribution. It is therefore concluded that the ion beams and the bumps do not have a permanent damaging effect on the pixels of the sensor.

9.3 Simulation

In order to qualitatively understand the bumps and electron-like cluster observed at the testbeam, two simulations are performed. First, a GEANT4 [45] simulation dedicated to the interaction between ion beams and sensor material is performed. Second, an AllPix² [46] simulation is performed, focusing on in-pixel effects. However, all simulations performed in this section are only used for a qualitative understanding rather than a quantitative analysis of the expected response of the HV-MAPS in ion beams.

9.3.1 GEANT4 Simulation

GEANT4 is a Monte Carlo simulation for particle-matter interaction developed by the GEANT4 collaboration [45]. This toolkit is widely used in high energy physics. For example, all 4 large LHC experiments use GEANT4 for detector simulation. GEANT4 is based on C++ and has a modular structure allowing an easy access to the toolkit. Physics processes can be simulated by different so-called physics lists. These lists describe an interaction process and can be divided into electromagnetic

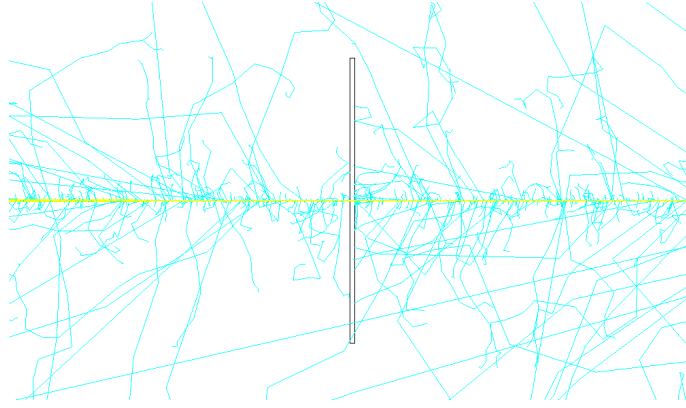


Figure 9.12: GEANT4 event display of 100 primary carbon ions with an energy of 430 MeV/u. The silicon sensor is shown in black. The tracks of positively charged particles are shown in yellow and negatively charged in blue. The primary particles fly from the right side to the left side of the event display.

and hadronic components. The simulation performed here uses the standard electromagnetic physics module of GEANT4 *EMStandard*, which covers an energy range of 0 – 100 TeV, however the accuracy worsens below energies of 1 keV. The electromagnetic interaction of ions is described by the Urban model [47] and the ionization by ions is described by the Bethe equation (Equation 4.1) in this physics module. The entire description of this physics description can be found in [48]. The inelastic hadronic component is described by the physics list *QGSP_BIC_HP*¹ and by the additional inelastic ion cross section module *IonPhysicsXS*. [48] The track of every primary and secondary particle is simulated in a customizable step size. At each step, ionization and scattering effects are calculated. It is possible to suppress the simulation of short-ranged secondary particle tracks with a minimum track length requirement. If the track of a particle is shorter than the chosen minimum track length requirement, the particle is not produced and its absorption energy is added to the ionization loss of the primary particle. In this simulation, the cut on the track length of secondary particle is set to 50 μm , which would correspond to a secondary particle traveling at least to the neighboring pixel. The toolkit allows to build detectors and absorbers out of different pre-built and customizable materials. For each created volume all information on the particle traversing the material is accessible and can be logged, for example its particle type or its energy. It is also possible to create an active detector response and electromagnetic fields. However, this is beyond the scope of the simulation performed here.

The simulation setup is chosen here to consist of a $20 \times 20 \times 0.6 \text{ mm}^3$ passive silicon block in a volume consisting of air using the pre-built material *G4Air*. The silicon

¹QGSP: Quark-gluon string precompound model. BIC: Binary light ion cascade. HP: High precision neutron model.

sensor is not simulated as an active pixel sensor, since a pixel structure increases the computing time significantly. If a particle loses energy by ionization in or scatters on the silicon, the position, the time, the energy loss and the particle type are logged. In front of the sensor $15\ \mu\text{m}\ \text{SiO}_2$ ² are placed, representing the NMOS and PMOS transistor layer and metal layers of the sensor. This layer may lead to absorption or creation of secondary particles. GEANT4 allows to produce primary particles with a given energy. In addition, the particles can be produced point like or in a diffuse beam-like shape. Since this simulation does not focus on a readout or pixel structure, the position of the primary particle is not of significance. The ion beam is created point-like 20 cm in front of the sensor, which is shorter than the distance between beam window and sensor at HIT to reduce the computing time. For each particle and beam energy used at HIT a simulation run with 10^5 primary particles is produced. Figure 9.12 shows the event display of 100 primary events of a carbon ion with an energy of 430 MeV/u.

The resulting energy deposition distribution (Figure 9.13a) shows two peaks for all simulations. One at the expected position of ionization energy loss calculated by the Bethe-formula (Equation 4.1) and a second peak below < 100 keV energy loss. This second peak corresponds to mostly short ranged secondary particles created in the silicon, for example δ -electrons. However, in case of the carbon energy loss distribution, this peak is larger than in the distribution of protons and helium.

Carbon Beam Analysis

The GEANT4 simulation is used to determine whether the electron-like particles observed in the HIT measurements are created by a carbon ion beam and whether these particles are electrons which are in time but not spatially correlated with carbon hits. The larger peak of secondary particles below < 100 keV energy deposition in the carbon spectrum could explain the additional electrons observed at HIT. Since the GEANT4 simulation includes the particle type creating the energy loss, it is determined that this second peak is almost entirely created by electrons traversing the detector (Figure 9.13b). However, other types of secondary particles contribute to this peak, which is discussed in more detail in the next section. In case of the carbon beam, an electron is detected every second event, while for a helium beam of 220 MeV/u only in 2 % of all events an electron is detected (Figure 9.14). The other particles detected and shown in Figure 9.14 are created by interactions discussed in the next section. The number of electrons detected in the sensor includes δ -electrons created in the silicon, but in addition electrons which are not created in silicon are detected. These electrons are produced by ionization in the air in front of the sensor and fly with the ion beam to the detector. The event display in Figure 9.12 visualizes this effect, where the carbon beam is shown in yellow and the electrons in blue. The cross section of this process is quadratically dependent on the charge number Z of

²Estimation: Typical thickness of the transistor and metal layers in HV-CMOS sensors. [49]

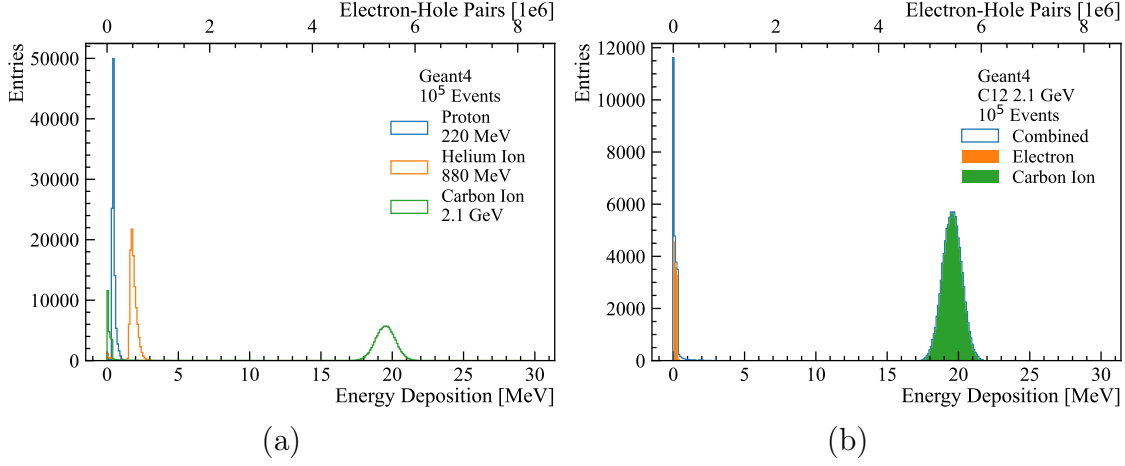


Figure 9.13: a) Histogram of the energy deposition of different particles in 600 μm silicon simulated with GEANT4. b) Simulated energy deposition of carbon ion beam with an energy of 176 MeV/u.

the particle beam. Thus, the ratio R_{e^-} of electrons detected in the sensor between a helium and a carbon beam should follow:

$$R_{e^-} = \frac{Z_{\text{He}}^2}{Z_{\text{C}}^2} = \frac{2^2}{6^2} = \frac{1}{9} \quad (9.5)$$

$$R_{e^-} \approx 0.11 \quad (9.6)$$

In contrast, a ratio of $R_{e^-} = 0.03$ is determined by the Monte Carlo simulation. The deviation between expectation and simulation is caused by the different beam energy of helium and carbon. Since the energy transfer to the electron depends on the beam energy, it is more likely that electrons created by an interaction between air and the carbon beam have high enough energy to reach the detector than electrons created by a helium beam. The electrons produced in the air and reaching the detector are not spatially correlated to the ion hit and can explain the additional electron-like clusters. Additionally, it is observed that the carbon ion and the electron hit are correlated in a time range of about 2 ns. At HIT a time correlation of 10 ns is measured, which is compatible with the simulation in terms of the time resolution of the sensor. Therefore, it is concluded that the small clusters observed in the carbon ion beam at HIT are electrons. However, a quantitative comparison of the number of electrons detected between simulation and experiment is not possible. On one hand, the readout and pixel structure is neglected in the simulation, hence it is not possible to determine the number of detected electrons correctly. On the other hand, the total number of electrons measured at HIT can not be determined precisely, since the ToT and the cluster size distribution of electrons and carbon ions are overlapping and therefore they are not precisely distinguishable. Additionally, data is lost in the FIFO, which results in large uncertainties.

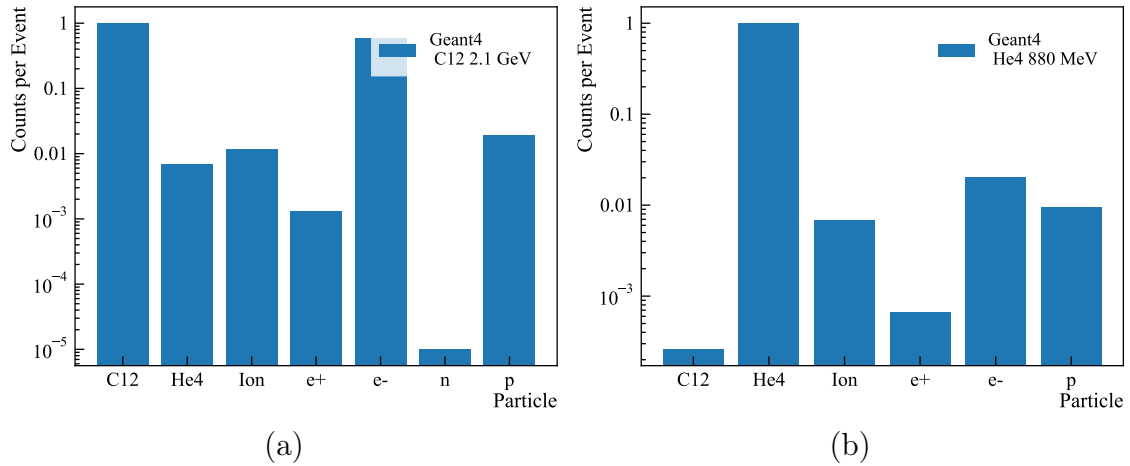


Figure 9.14: Histogram of particle types traversing a 600 μm silicon sensor. Carbon (a) and helium (b) beams are used, simulated by using GEANT4. The bin "Ion" contains other ions excluding ^{12}C and ^4He ions.

Bumps

Lastly, GEANT4 is used to simulate the number of inelastic nuclear interactions. For that, the same simulation data set as before is used. The particle types observed in the sensor hint on the inelastic interaction between silicon atoms and the ion beam, since secondary ions are produced. Figure 9.14 shows the histogram of particle types traversing the detector using a helium and carbon beam. The simulation shows that secondary ions produced by an inelastic collision between a carbon beam and silicon sensor material deposit up to 200 MeV in the sensor, which equals 55×10^6 electron-hole pairs created in the silicon (Figure 9.15b). For helium and proton beams, secondary ions created by an inelastic collision deposit up to 50 MeV and 20 MeV in the sensor material, respectively. The high number of electron-hole pairs produced in an inelastic collision of helium and carbon ions with the silicon sensor could lead to a large cluster structure like a bump. A second simulation is performed to determine the number of inelastic collisions more precisely.

GEANT4 includes various example simulations to become familiar with the toolkit. One of these simulations is Had03, which simulates a fixed target experiment to quantify nuclear processes and simulate the particles produced. This simulation is used to determine the probability of an inelastic interaction in order to compare it with the bump probability. The Had03 simulation uses the same hadronic physics model as before, however it neglects electromagnetic interaction. Neglecting ionization effects reduces the computing time significantly. As a result the number of simulated events is increased to 10^6 . The definition of a silicon target and an ion beam is easily possible in this pre-built simulation. This simulation is performed for the different helium and carbon beam settings used at the HIT testbeam for a 100 and a 600 μm silicon target simulating an upper limit on the depleted and a lower limit on the undepleted region of the detector. The resulting probabilities for

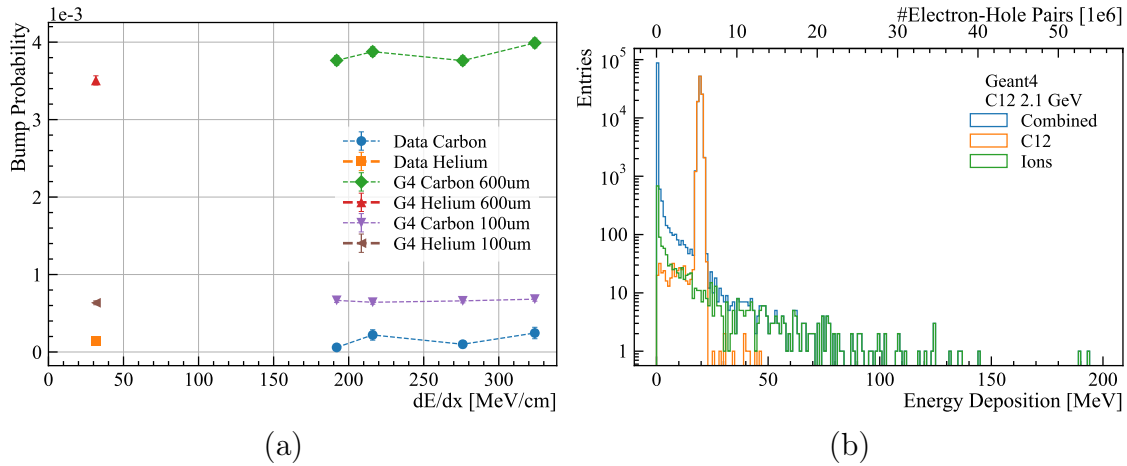


Figure 9.15: a) Comparison between measured bump probability and probability of inelastic collision simulated with GEANT4 in dependency of the calculated energy deposition. The simulation data is shown for a 100 μm and 600 μm thick silicon target. b) Energy deposition per particle type of a 176 MeV/u (2.1 GeV) carbon ion beam simulated with GEANT4.

an inelastic collision are shown in Figure 9.15a. The simulation yields almost 4000 inelastic interaction between a carbon ion with an energy of 2.1 GeV and 600 μm silicon out of 10^6 primary events. 17000 free protons and 16000 neutrons are produced together with isotopes in the 4000 inelastic collisions. The most common isotopes produced are deuterons, helium (including α -particles), silicon, aluminum and magnesium.

The resulting probabilities of an inelastic interaction are compared to the bump probability measured at the HIT test beam in Figure 9.15a. The simulated probability of an inelastic interaction in 600 μm is almost an order of magnitude larger than the measured bump probability for carbon and helium. This indicates that nuclear interactions in the undepleted region do not create a bump like signal in the detector. The interaction probability for a 100 μm target is about 1.5 larger than the measured bump probability. Different reasons could cause the discrepancy between the 100 μm simulation and the measured data. Firstly, it is unknown how much energy deposition is needed to create a bump. Therefore, it is not known if every inelastic interaction can create a bump cluster. Secondly, the depletion zone is likely smaller than 100 μm and the contribution of diffusing charges to the signal is unknown. Hence, the number of inelastic collisions determined by the simulation overestimates the number of detected bumps in the sensor. To understand the effect of diffusion charges on the signal, a simulation including the pixel structure needs to be performed.

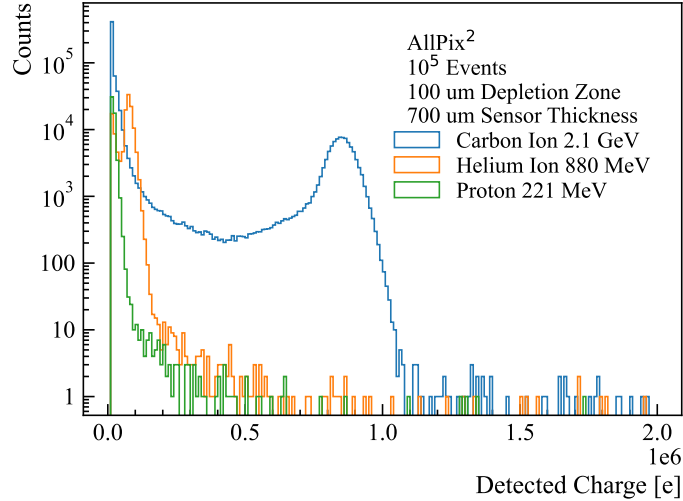


Figure 9.16: Number of electron-hole-pairs detected by a QDC-like readout simulated using Allpix².

9.3.2 Allpix² Simulation

Allpix² [46][50] is a simulation toolkit for simulating the pixel structure of a silicon detector. The major difference between GEANT4 and Allpix² is that Allpix² allows different approaches to simulation of drifting and diffusing electron-hole pairs created by ionization, which reduces the computing time of a simulated active pixel sensor significantly. Additionally, it simulates the charge collection and signal generation in the pixel electronics. The initial charge deposition in the detector can be simulated in three ways, a point like deposition of a specified number of electron-hole pairs, a charge deposition based on GEANT4 and a cosmic ray module. In the simulation used here, the GEANT4 based deposition module is used. A similar description as in the GEANT4 simulation performed before (Section 9.3.1) is used. However, it is not possible to adapt the pre-built physics list as used in the GEANT4 simulation. As a result, the optional *IonInelasticXS* description is not used, which provides a more precise cross section of light ion interaction.

The creation of detector material is similar based on GEANT4. AllPix² allows to build the device under test as a monolithic or hybrid pixel sensor. In addition, it is possible to arrange multiple sensor layers in one simulation. An AP3.1 like monolithic silicon sensor with a substrate thickness of 700 μm with a depletion zone of 100 μm , which is probably larger than the depletion zone of AP3.1, and a transistor and metal layer of 15 μm silicon dioxide, like in Section 9.3.1, is created. This sensor is placed in a volume of air. The start of the beam simulation is 20 cm in front of the sensor to allow ionization effects in air similar to the GEANT4 simulation. The depletion zone of the sensor and the electric field can be described by a mathematical function, for example a constant, a linear or a parabolic function or by a mesh of field strength externally provided in an "INIT" data file. Within the scope of this simulation here, a linear description of the electric field in the entire depletion

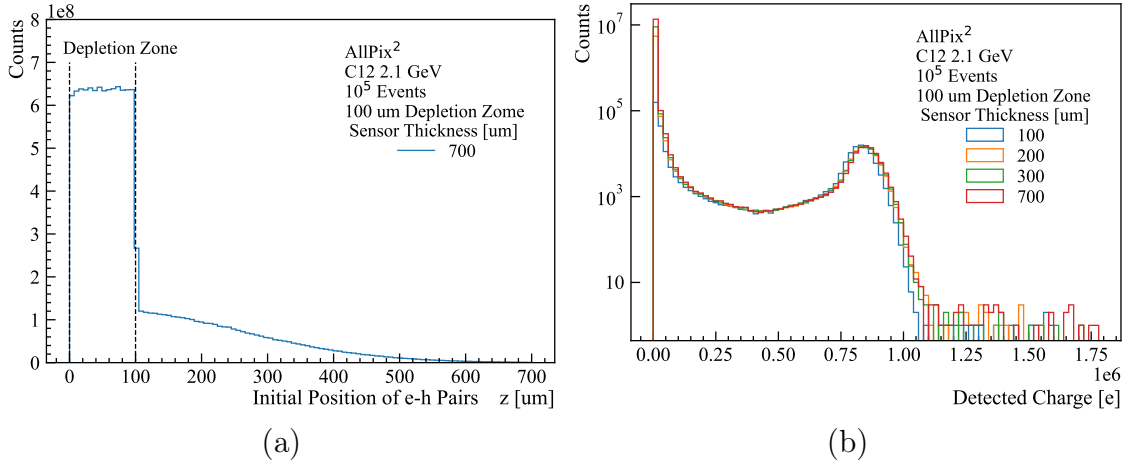


Figure 9.17: a) Initial position of charge carriers detected by the readout implant.
b) Simulation of the detected signal per pixel in electron for all pixels and different sensor thicknesses.

zone with a bias voltage of -60 V is assumed to be sufficient. The electron charges generated by the deposition module are propagated to the readout implants in the depletion zone. During this propagation, both diffusion and drift effects are simulated. Allpix² provides three different ways to describe the propagation of charge carriers. For this simulation, the projection module is used to reduce the computing time, caused by the large amount of electron-hole pairs created by the carbon ion beam. In addition to the charge propagation charge sharing between pixels is also simulated, where one can choose between the 3 different types of charge sharing mechanisms: CapacitiveTransfer, InducedTransfer and PulseTransfer. In this case, only the PulseTransfer module can be used, because the other modules need a more complex description of the electric field. This module sums up the propagated charges to one short pulse per pixel. This approach overestimates the effect of a diffusion current, since it creates a short pulse out of a long but low current of diffusion charges.

The simulated pulse is read by a digitizer module. One can choose between the simulation of a charge sensitive amplifier (CSA), a QDC (Charge-to-digital) and TDC (time-to-digital). For this simulation, a QDC like readout without a threshold is chosen to register the amount of collected charge, although the CSA is a better description of the amplifier in the AP3.1. The CSA is not used because it does not simulate the saturation effects of the amplifier, which are required for the large pulses created by the ion beam. Additionally, the CSA module amplifies the short pulse created by the PulseTransfer module, which leads to an overestimation of the signal amplitude in respect to the experiment, where a long pulse with low amplitude has to be amplified by the CSA. The simulation description used here is not suitable for studying the effects of diffusion charges in the AP3.1, since it will detect small but constant current of charge carriers, which might not induce a signal in a

real sensor. The simulation is still used to determine the number of electron charges reaching the depletion zone of the sensor.

A proton beam with an energy of 221 MeV, a helium beam of 880 MeV and a carbon beam of 2.1 GeV with 10^5 primary particles each are simulated. For each event, a hit information of the QDC digitizer is stored for all hits. The hit information contains the pixel address, the timestamp and the number of electrons collected in the pixel. Additional debug histograms of the simulation modules are stored for each simulation run.

The histogram of the detected electron-hole pairs (Figure 9.16) looks similar to the energy deposition histogram (Figure 9.13a) created by the GEANT4 simulation. In the spectra of the helium and carbon beams, two peaks are visible, one at a higher number of electron-hole pairs corresponding to the particle hit and a peak below 10 ke corresponding to hits in adjacent pixels detecting charge sharing. In case of the proton beam the peak of the proton hit and the peak caused by charge sharing are overlapping. However, the number of detected electrons in the seed pixel is much lower than in the GEANT4 simulation for all three particle types. For example, the number of created electron-hole pairs of the carbon beam with an energy of 176 MeV/u (2.1 GeV) is more than 7 times higher in the GEANT4 simulation than in the Allpix² simulation. This leads to the assumption that not all diffusion charges are detected by the pixel readout. The propagation module of the simulation produces a histogram of the initial position of the electron-hole pairs created by ionization that are detected by the pixels. Figure 9.17a shows that almost all detected electrons are created in the depletion zone of the sensor. A steep step between the depleted and undepleted region of the sensor is visible. This step is caused by the description of the electric field in the sensor, since no variation of the electric field between different pixels is simulated. Outside of the depletion zone, the number of detected electrons decreases exponentially with the initial position of the charge carrier creation in z-direction (depth). To understand the contribution of diffusion charges to the signal, a simulation with different sensor thicknesses is performed. For that, a carbon beam with a beam energy of 2.1 GeV is used. The histogram of the detected electrons for different sensor thicknesses is shown in Figure 9.17b. For all sensor thicknesses, the same two peak structure as in Figure 9.16 is observed. The broad peak, which corresponds to the seed pixel of a hit cluster, peaks at 900 ke for all sensor thicknesses between 200 and 700 μm , while for the 100 μm sensor the peak is shifted to a lower value by 100 ke. This yields that the number of detected charge carriers in the seed pixel, the pixel hit by the ion, do not increase with the sensor thickness above a sensor thickness of 200 μm . In contrast, the number of pixels recording a small signal, which corresponds to the sharp peak in Figure 9.17b, increases with the sensor thickness. The hits with a small signal are caused by charge sharing due to lateral diffusion in the undepleted region of the sensor. In total, the number of electrons collected by all pixels is 1.7 times larger in a 700 μm sensor than in a completely depleted 100 μm silicon sensor. This indicates that the sensor thickness affects the cluster size of an ion hit, but does not increase the

signal amplitude at the center of the cluster significantly. Thus, the observed delay of hits in outer pixels of a cluster in the carbon measurement can be caused a contribution of lateral diffusion to the signal. However, this simulation cannot be used to determine the expected cluster size of ion hits for the HIT test beam because it is not known how many of these small signals will pass the threshold of a real sensor.

9.3.3 Summary

In this section a GEANT4 and an Allpix² are performed to qualitatively study the observation of the ion beam measurement. GEANT4 is a useful simulation tool to determine the interaction between beam particles and sensor material. The simulation used here yields that electrons are created by interactions between carbon beam and air and hints that bumps are created by nuclear interaction between an ion beam and the sensor material.

In contrast, Allpix² is a tool to simulate the electronic response of pixels sensors. Different approaches can be used to reduce the computing time for the simulation of a pixel detector. However, the response of a largely undepleted sensor can not be simulated easily. The Allpix² simulation performed here hints that only a fraction of the electron-hole pairs created in the undepleted region of the sensor create a signal in the sensor. However, the diffusing charges in the undepleted region can increase the size of hit clusters due to lateral diffusion.

10 Conclusion

In this thesis, the ATLASPix3.1 HV-MAPS sensor together with the GECCO DAQ system are used to develop and validate different measurement environments which can be used to test the MightyPix v1 prototype with respect to its application in the LHCb experiment. Moreover, the measurements performed in this thesis can hint on the expected performance of the MightyPix v1 prototype, since the ATLASPix3(.1) is predecessor of the MightyPix.

The GECCO DAQ system is commissioned in Heidelberg and its proper functioning is verified. The firmware of the GECCO system is improved to operate the sensor at higher data rates and to increase the hit rate capabilities of the DAQ system. The ATLASPix3.1 is successfully tuned using injection pluses, which are calibrated using an iron-55 γ -radiation source. A similar tuning procedure is foreseen for the calibration of the MightyPix prototype.

The hit rate capabilities of the ATLASPix3.1 are determined using a photon beam of an X-ray tube. It is determined that the hit rate limitations of the ATLASPix3.1 are caused by its finite state machine. The experimental rate limitations of the AP3.1 is 9.7 MHz and agrees with the theoretical limit calculation of 9.8 MHz. Rate measurements with X-ray tubes can be a useful to determine hit rate dependent effects in MightyPix prototypes, which will be operated in a high particle rate environment.

It is demonstrated that ion beams can be used to study the response of the AP3.1 sensor to large energy depositions. The energy deposition of an ion beam in the ATLASPix3.1 sensor is correlated with the size of the hit cluster and the ToT of a cluster. Large cluster, here called bumps, are observed in the beam of helium and carbon ions. There is evidence that these bumps are created by nuclear interaction between an ion beam and the sensor material. The knowledge of the detector response of HV-MAPS to ion beams is important for future tests using ion beams to study the effect of single events upsets and the energy dependence of hit cluster sizes.

For a more comprehensive understanding of the physical processes driving the detector response of HV-MAPS to large energy depositions by ion beams a GEANT4 and an Allpix² simulation are performed. The GEANT4 simulation is used to determine effects in the interaction between ion beam and sensor material. The results of this simulation support the hypothesis that the bumps are caused by nuclear interactions between the beam and the sensor material. An Allpix² simulation is performed to determine the influence of ionization in the undepleted substrate of the sensor. This

simulation yields that electron-hole pairs created in the undepleted region of the sensor increase the size of a hit cluster. However, a more detailed simulation study is necessary to determine how many of the signals created by lateral diffusion in the undepleted region pass the threshold of an HV-MAPS. A simulation study about the signal caused by diffusing charges can be supplemented by a comparison measurements between sensors, which have different thicknesses.

In conclusion, setups to study hit rate dependent effects in the readout of the AP3.1 and setups and simulations to study large energy deposition in the AP3.1 have been developed. The developed measurement setups allowed to systematically study the ATLASPix3.1 sensor and these setups can be used to test the MightyPix sensors as well.

A Sensor Configuration

Voltage	Voltage on Sensor	Voltage on GECCO
HV	-60 V	-60 V
VDD33	-	3.10 V
VDD	1.85 V	1.93 V
VSSA	1.26 V	1.30 V
VMinus	0.58 V	0.63 V
VLVDS	-	1.60 V
Gate	2.08 V	2.10 V

Table A.1: Voltages applied to the sensor and DAQ system.

VDAC Parameter	DAC Value
Bl	140
Th	155 – 170
Inj	0 – 255

Table A.2: VDAC settings used for measurements.

Configuration Parameter	Value
ckdivend	0
ckdivend2	7
timerend	0 or 1*
slowdown	3
maxcycend	255

Table A.3: Configuration bits used for measurements. *Only for external clock of 600 MHz.

Parameter	DAC Value
BIRes	8
IThRes	8
VN1	20
VNFoll	13
VNRegc	8
VNDel	8
VPComp	8
VPDAC	8
VN2	0
VBlresdig	8
VNBias	8
VPLoad	8
VNOut	8
VPDclMux	11
VNDclMux	11
VPDelDcl	11
VNDelDcl	11
VPDelPreEmp	11
VNDelPreEmp	11
VPDcl	11
VNDcl	11
VNLVDS	20
VNLVDSDel	3
VPPump	0
VPreRegCasc	20
VPrampDig	20
VNComp	22
VPFoll	16
VNDAC	7
VPBiasRec	30
VNBiasRec	30

Table A.4: DAC settings used for measurements

B Hitmap Pattern

B.1 State Machine Error

When the state machine of the 1.2 Gbit/s readout runs at 60 MHz the hit information is corrupted. The data is corrupted by the FSM not setting certain bits of the data. This shows up in the hitmap as a kind of grid pattern. Additionally, both timestamps are corrupted as well.

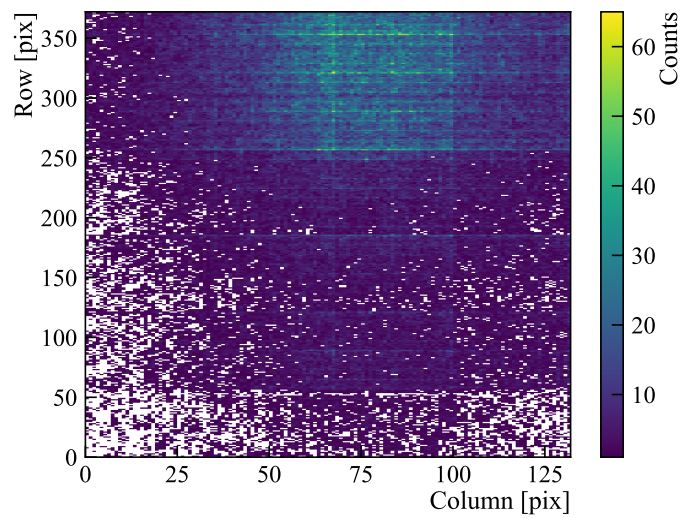
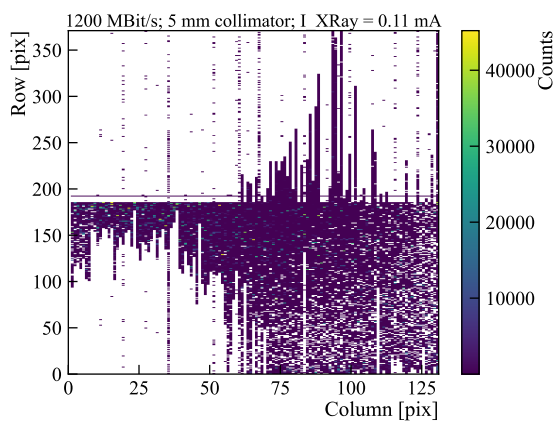


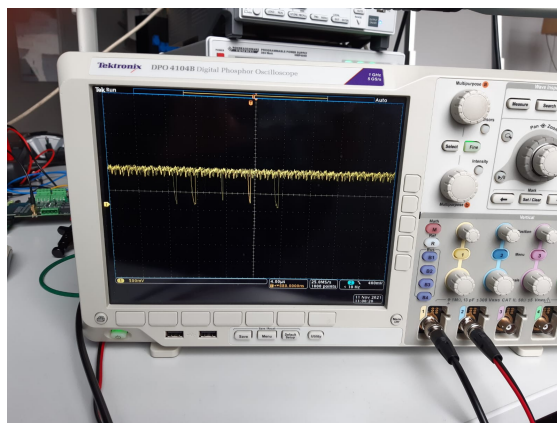
Figure B.1: Pattern observed at $f_{SM} = 60$ MHz using an ^{90}Sr source. Radiation spot in row 250 – 350.

B.2 Oscillation

If many pixels are noisy, the other pixels of the sensor also become noisy. This leads to a cascade effect, whereby all pixels send hits continuously. This effect is visible at the Hitbus test output, where only a noisy high level is seen (Figure B.2). In the hitmap (Figure B.2a) this leads to encoding failures and column drain effects.



(a)



(b)

Figure B.2: Sensor in oscillation state: a) Measured hitmap. b) Hitbus test output.

C Bibliography

- [1] Peter W. Higgs. “Broken Symmetries and the Masses of Gauge Bosons”. In: *Phys. Rev. Lett.* 13 (16 Oct. 1964), pp. 508–509. DOI: [10.1103/PhysRevLett.13.508](https://doi.org/10.1103/PhysRevLett.13.508).
- [2] ATLAS Collaboration. G. Aad et al. “Observation of a new particle in the search for the Standard Model Higgs boson with the ATLAS detector at the LHC”. In: *Physics Letters B* 716.1 (Sept. 2012), pp. 1–29. DOI: [10.1016/j.physletb.2012.08.020](https://doi.org/10.1016/j.physletb.2012.08.020). URL: <https://doi.org/10.1016%2Fj.physletb.2012.08.020>.
- [3] CMS Collaboration. S. Chatrchyan et al. “Observation of a new boson at a mass of 125 GeV with the CMS experiment at the LHC”. In: *Physics Letters B* 716.1 (Sept. 2012), pp. 30–61. DOI: [10.1016/j.physletb.2012.08.021](https://doi.org/10.1016/j.physletb.2012.08.021). URL: <https://doi.org/10.1016%2Fj.physletb.2012.08.021>.
- [4] A.D. Sakharov. “Violation of CP Invariance, C asymmetry, and baryon asymmetry of the universe”. In: *Sov. Phys. Usp.* 34.5 (1991), pp. 392–393. DOI: [10.1070/PU1991v034n05ABEH002497](https://doi.org/10.1070/PU1991v034n05ABEH002497).
- [5] Super-Kamiokande Collaboration: Y. Fukuda et al. “Measurements of the Solar Neutrino Flux from Super-Kamiokande’s First 300 Days”. In: *Physical Review Letters* 81.6 (Aug. 1998), pp. 1158–1162. DOI: [10.1103/physrevlett.81.1158](https://doi.org/10.1103/physrevlett.81.1158). URL: <https://doi.org/10.1103%2Fphysrevlett.81.1158>.
- [6] Gianfranco Bertone, Dan Hooper, and Joseph Silk. “Particle dark matter: evidence, candidates and constraints”. In: *Physics Reports* 405.5-6 (Jan. 2005), pp. 279–390. DOI: [10.1016/j.physrep.2004.08.031](https://doi.org/10.1016/j.physrep.2004.08.031). URL: <https://doi.org/10.1016%2Fj.physrep.2004.08.031>.
- [7] Ivan Perić. “A novel monolithic pixelated particle detector implemented in high-voltage CMOS technology”. In: *Nuclear Instruments and Methods in Physics Research Section A: Accelerators, Spectrometers, Detectors and Associated Equipment* 582.3 (2007). VERTEX 2006, pp. 876–885. ISSN: 0168-9002. DOI: <https://doi.org/10.1016/j.nima.2007.07.115>.
- [8] Wikimedia Commons. *Standard Model of Elementary Particles*. URL: https://en.wikipedia.org/wiki/File:Standard_Model_of_Elementary_Particles.svg.
- [9] Sheldon L. Glashow. “Partial-symmetries of weak interactions”. In: *Nuclear Physics* 22.4 (1961), pp. 579–588. ISSN: 0029-5582. DOI: [https://doi.org/10.1016/0029-5582\(61\)90469-2](https://doi.org/10.1016/0029-5582(61)90469-2).

- [10] A. Salam and J.C. Ward. “Electromagnetic and weak interactions”. In: *Physics Letters* 13.2 (1964), pp. 168–171. ISSN: 0031-9163. DOI: [https://doi.org/10.1016/0031-9163\(64\)90711-5](https://doi.org/10.1016/0031-9163(64)90711-5).
- [11] Steven Weinberg. “A Model of Leptons”. In: *Phys. Rev. Lett.* 19 (21 Nov. 1967), pp. 1264–1266. DOI: [10.1103/PhysRevLett.19.1264](https://doi.org/10.1103/PhysRevLett.19.1264).
- [12] M.E. Peskin and D.V. Schroeder. *An Introduction To Quantum Field Theory*. Frontiers in Physics. Avalon Publishing, 1995. ISBN: 9780813345437.
- [13] LHCb Collaboration. *LHCb Tracker Upgrade Technical Design Report*. Tech. rep. 2014. URL: <https://cds.cern.ch/record/1647400>.
- [14] LHCb Collaboration. *LHCb VELO Upgrade Technical Design Report*. Tech. rep. 2013. URL: <https://cds.cern.ch/record/1624070>.
- [15] LHCb Collaboration. *LHCb PID Upgrade Technical Design Report*. Tech. rep. 2013. URL: <https://cds.cern.ch/record/1624074>.
- [16] Ryunosuke O’Neil. “HV-MAPS for the LHCb Upgrade-II Mighty Tracker”. The International Workshop on Vertex Detectors (VERTEX 2022). 2022. URL: <https://cds.cern.ch/record/2838632>.
- [17] LHCb Collaboration. *Framework TDR for the LHCb Upgrade II - Opportunities in flavour physics, and beyond, in the HL-LHC era*. Tech. rep. Geneva: CERN, 2021. URL: <https://cds.cern.ch/record/2776420>.
- [18] T. Ackernley et al. *Mighty Tracker: Design studies for the downstream silicon tracker in Upgrade Ib and II*. Tech. rep. Geneva: CERN, 2019. URL: <https://cds.cern.ch/record/2658015>.
- [19] Heiko Augustin et al. *Preliminary Specification of a HV-CMOS Pixel Chip for LHCb Upgrade II*. Tech. rep. Geneva: CERN, 2020. URL: <https://cds.cern.ch/record/2730494>.
- [20] R. L. Workman et al. “Review of Particle Physics”. In: *PTEP* 2022 (2022), p. 083C01. DOI: [10.1093/ptep/ptac097](https://doi.org/10.1093/ptep/ptac097).
- [21] A. Bethe and J. Ashkin. “Passage of radiation through matter”. In: *Experimental Nuclear Physics* 1 (1953).
- [22] Hermann Kolanoski and Norbert Wermes. *Teilchendetektoren. Grundlagen und Anwendungen*. 1. Aufl. 2016. Berlin, Heidelberg: Springer Spektrum, 2016. ISBN: 978-3-662-45350-6. URL: <http://dx.doi.org/10.1007/978-3-662-45350-6>.
- [23] Lev Landau. “On the energy loss of fast particles by ionization”. In: *J. Phys.* 8 (1944), pp. 201–205. URL: <https://cds.cern.ch/record/216256>.
- [24] Wikimedia Commons. *PN-junction equilibrium*. URL: <https://en.wikipedia.org/wiki/File:Pn-junction-equilibrium.png>.

- [25] Frank Thuselt. *Physik der Halbleiterbauelemente. einführendes Lehrbuch für Ingenieure und Physiker*. ger. 3. Auflage. Berlin: Springer Spektrum, 2018. ISBN: 978-3-662-57638-0. DOI: [10.1007/978-3-662-57638-0](https://doi.org/10.1007/978-3-662-57638-0).
- [26] Tuomas Poikela et al. “The VeloPix ASIC”. In: *JINST* 12 (2017), C01070. 8 p. DOI: [10.1088/1748-0221/12/01/C01070](https://doi.org/10.1088/1748-0221/12/01/C01070). URL: <https://cds.cern.ch/record/2275005>.
- [27] A Lattucaon. “MAPS application for the ITS upgrade”. In: *Nuovo Cimento C* 39 (2016), 259. 6 p. DOI: [10.1393/ncc/i2016-16259-0](https://doi.org/10.1393/ncc/i2016-16259-0). URL: <https://cds.cern.ch/record/2282361>.
- [28] W. Shockley. “Currents to Conductors Induced by a Moving Point Charge”. In: *Journal of Applied Physics* 9.10 (Oct. 1938), pp. 635–636. DOI: [10.1063/1.1710367](https://doi.org/10.1063/1.1710367).
- [29] Ivan Perić. *ATLASPix3 User Manual*. 2019.
- [30] *Technical Design Report for the ATLAS Inner Tracker Pixel Detector*. Tech. rep. Geneva: CERN, 2017. DOI: [10.17181/CERN.FOZZ.ZP3Q](https://doi.org/10.17181/CERN.FOZZ.ZP3Q). URL: <https://cds.cern.ch/record/2285585>.
- [31] H. Augustin et al. “MuPix8 — Large area monolithic HVCMOS pixel detector for the Mu3e experiment”. In: *Nuclear Instruments and Methods in Physics Research Section A: Accelerators, Spectrometers, Detectors and Associated Equipment* 936 (2019). Frontier Detectors for Frontier Physics: 14th Pisa Meeting on Advanced Detectors, pp. 681–683. ISSN: 0168-9002. DOI: <https://doi.org/10.1016/j.nima.2018.09.095>.
- [32] Rudolf Schimassek. *Development and characterisation of integrated sensors for particle physics*. Karlsruhe, 2021. URL: <http://dx.doi.org/10.5445/IR/1000141412>.
- [33] Klaas Padeken. “MightyTracker - Upgrade 1B and 2”. Jahrestreffen der deutschen LHCb-Gruppen (Theorie und Experiment). 2022.
- [34] Rudolf Schimassek. *Description of the GECCO Test System*. 2021. URL: https://git.scc.kit.edu/adl_documents/gecco_documentation.
- [35] Felix Ehrler. “Characterization of monolithic HV-CMOS pixel sensors for particle physics experiments”. PhD thesis. Karlsruher Institut für Technologie (KIT), 2021. DOI: [10.5445/IR/1000133748](https://doi.org/10.5445/IR/1000133748).
- [36] Digilent Inc. *Nexys Video Reference Manual*. Sept. 2020. URL: https://digilent.com/reference/_media/reference/programmable-logic/nexys-video/nexys-video_rm.pdf.
- [37] PHYWE Systeme GmbH. *XR 4.0 Operating Instructions*. Göttingen. URL: https://www.phywe.com/physics/modern-physics/x-ray-physics/xr-4-0-expert-unit-35-kv_1557_2488/.

- [38] David Ondreka and Udo Weinrich. “The Heidelberg Ion Therapy (HIT) accelerator coming into operation”. In: *European Physical Society Accelerator Group, Proceedings of EPAC* (2008), pp. 23–27.
- [39] Universitätsklinikum Heidelberg. *Heidelberger Ionenstrahl-Therapiezentrum (HIT): Die Beschleunigeranlage*. URL: https://www.klinikum.uni-heidelberg.de/fileadmin/hit/images/Beschleuniger_mit_Beschriftung.png.
- [40] Dohun Kim. *Timing Study and Optimization of ATLASPix3 a full-scale HV-MAPS Prototype*. Master Thesis. 2020.
- [41] Heiko Augustin. *Development of a novel slow control interface and suppression of signal line crosstalk enabling HV-MAPS as sensor technology for Mu3e*. eng. Heidelberg, 2021. DOI: [10.11588/heidok.00030885](https://doi.org/10.11588/heidok.00030885). URL: <http://nbn-resolving.de/urn:nbn:de:bsz:16-heidok-308858>.
- [42] David Maximilian Immig. *Characterization of ATLASPix1, an HV-CMOS Demonstrator for the Phase-II Upgrade of the ATLAS Inner Tracker*. Master Thesis. 2019.
- [43] R. Hermann. “Development of a Scintillation Fiber Transverse Profile Monitor for Low-Intensity Ion Beams at HIT”. Heidelberg Workshop on Particle Detectors for Ion Beam Therapy Applications. 2022.
- [44] R. Hermann. “Discussion of testbeam results”. Private Communication.
- [45] S. Agostinelli et al. “Geant4—a simulation toolkit”. In: *Nuclear Instruments and Methods in Physics Research Section A: Accelerators, Spectrometers, Detectors and Associated Equipment* 506.3 (2003), pp. 250–303. DOI: [https://doi.org/10.1016/S0168-9002\(03\)01368-8](https://doi.org/10.1016/S0168-9002(03)01368-8).
- [46] S. Spannagel et al. “Allpix2: A modular simulation framework for silicon detectors”. In: *Nuclear Instruments and Methods in Physics Research Section A: Accelerators, Spectrometers, Detectors and Associated Equipment* 901 (2018), pp. 164–172. ISSN: 0168-9002. DOI: <https://doi.org/10.1016/j.nima.2018.06.020>.
- [47] László Urbán. *A model for multiple scattering in GEANT4*. Tech. rep. Geneva: CERN, 2006. URL: <https://cds.cern.ch/record/1004190>.
- [48] GEANT4 Collaboration. *User Documentation Version: Geant4 11.0*. Tech. rep. 2021. URL: https://geant4.web.cern.ch/support/user_documentation.
- [49] H. Augustin. “Layout of HV-CMOS sensors”. Private Communication.
- [50] P. Schütze, S. Spannagel, and K. Wolters. *Allpix² User Manual*. Version v2.3.1. July 2022. URL: <https://project-allpix-squared.web.cern.ch/project-allpix-squared/usermanual/allpix-manual.pdf>.

Acknowledgments

First, I would like to thank Prof. Ulrich Uwer for giving me the opportunity to work in on this interesting research topic in the Heidelberg LHCb group. Thanks to Prof. André Schöning for agreeing to be the second examiner of my thesis.

I would like to thank the MightyPix team in Heidelberg Sebastian Bachmann and Maja Lecher for the great work together and helpful discussions towards an understanding of the ATLASPix3.1.

Furthermore, I am thankful for the several helpful discussions with the MightyPix sensor group and the Heidelberg HV-MAPS meeting. Especially, I would like to thank David Immig, Heiko Augustin and Jan Hammerich for the answers to my several questions on various HV-MAPS topics, which allowed me to gain a lot of knowledge. I am thankful to David, Heiko, Jan, Maja and Sebastian for reviewing my thesis.

I would like to thank Rudolf Schimassek for helping me setting up the GECCO system in the early stages of my thesis. Furthermore, I would like to thank Richard Hermann for the possibility to join his testbeam effort and for the discussion of the results of the testbeam.

Erklärung:

Ich versichere, dass ich diese Arbeit selbstständig verfasst habe und keine anderen als die angegebenen Quellen und Hilfsmittel benutzt habe.

Heidelberg, den 15.11.2022

.....